

LAMPOST SOURCE HEIGHT MEASUREMENTS

In unobscured Active Galactic Nuclei



Masterarbeit aus der Physik
vorgelegt von

Marco Fink

30. September 2016

Dr.-Karl-Remeis-Sternwarte Bamberg & ECAP
Friedrich-Alexander-Universität Erlangen-Nürnberg



Betreuer: Prof. Dr. Jörn Wilms

Cover Image: Author's impression of relativistic light bending around a supermassive black hole and an accretion disk. Inspired by the corresponding scenes of the 2014 movie *Interstellar* by Christopher Nolan. The visual effects were developed under supervision of theoretical physicist Kip Thorne. Acrylic on cardboard.

Zusammenfassung

In der vorliegenden Masterarbeit wird ein Sample sogenannter *bare* Active Galactic Nuclei analysiert. Das Sample basiert auf einer Studie durchgeführt von Walton et al. (2013) anhand von *Suzaku*-Beobachtungen. Nach dem Paradigma des vereinheitlichten Modells für Galaxienkerne können wir in *bare* AGN direkt in den innersten Teil der Akkretionsscheibe um ein supermassives schwarzes Loch (SMBH) sehen. Dort wird eine Röntgenstrahlungsquelle angenommen, die in den beobachteten Spektren direkt und in reflektierter Strahlung beobachtet wird, reprozediert von der opaquen Akkretionsscheibe. Das offensichtlichste Merkmal dieses Reflektionsspektrums ist die $K\alpha$ -Linie der fluoreszenten Emission von Eisen. In der Region nahe des Ereignishorizonts wird diese Linie verzerrt durch Gravitationsrotverschiebung, relativistischen Dopplereffekt und Gravitationslinseneffekte in einer stark gekrümmten Raumzeit. Durch diese Effekte sind dem Reflektionsspektrum, insbesondere der Fe- $K\alpha$ -Linie die physikalischen Eigenschaften des SMBH-Akkretionsscheiben-Systems aufgeprägt. Aus der Form des Spektrums können daher z. B. die Inklination und der Ionisationsgrad der Akkretionsscheibe, sowie der Spin-Parameter des SMBH bestimmt werden.

Diese Sample-Studie befasst sich mit der Geometrie der primären Strahlungsquelle. Aufbauend auf der oben erwähnten Studie erweitern wir sowohl Energiebreite als auch Auflösung der untersuchten Spektren indem wir Datensätze der Röntgenteleskope *XMM-Newton* und *NuSTAR* für einen Teil der Quellen des Samples kombinieren. Zur Analyse dieser Daten nutzen wir ein physikalisch konsistentes Modell einer Punktquelle auf der Rotationsachse der Akkretionsscheibe, die sogenannte *lamppost*-Geometrie. Zu Vergleichszwecken betrachten wir auch das etabliertere Modell einer Akkretionsscheibe deren Abstrahlung durch ein radiales Emissivitätsprofil gegeben ist. Beide Modelle liegen in Form der RELXILLP, bzw. RELXILL-Codes vor. Die *lamppost*-Variante des Modells eröffnet die Möglichkeit, direkt die Position der Strahlungsquelle zu vermessen. Wir unterscheiden außerdem zwischen einer Variante, bei der die Intensität der Quelle als freier Parameter betrachtet wird, und einer bei der diese *reflection fraction* intern konsistent aus der Quelhöhe über der Akkretionsscheibe ermittelt wird. Für die Bestimmung der physikalischen Parameter des Modells aus den Feinheiten des Breitbandspektrums, bereiten wir die Daten durch eine Lichtkurvenanalyse vor, um die Einflüsse von spektraler Variabilität auszuschließen. Wir betrachten für jede Quelle individuell das komplexe Verhalten des Spektrums im niederenenergetischen Bereich und diskutieren den Einfluss von Kalibrationseffekten zwischen den beiden verwendeten Detektoren.

Ein direkter Vergleich unserer Ergebnisse mit der Studie von Walton et al. zeigt, dass die Berücksichtigung des hochenergetischen Spektralbereichs beobachtet mittels *NuSTAR* einen systematischen Einfluss auf die gemessenen Parameter hat. Wir finden eine allgemeine Tendenz zu einem härteren primär-Kontinuum und einer erhöhten Akkretionsscheibenionisation gegenüber der *Suzaku*-Studie. Wir finden durchweg Spin-Parameter nahe dem physikalischen Maximum von $a = 0.998$. Unsere Datensätze lassen sich allgemein gut erklären anhand des *lamppost*-Modells. Der Vergleich zwischen freier *reflection fraction* und dem vollständig selbst-konsistenten Modell zeigt, dass beide Modelle die Daten vergleichbar gut reproduzieren können. Darüber hinaus können wir anhand des selbst-konsistenten Modells unphysikalische Lösungen ausschließen und Entartungen im Parameterraum vermeiden. Mit diesem Modell finden wir schließlich Werte für die Höhe der primär-Quelle bei im Mittel $4 r_g$.

Abstract

In this master thesis, I analyze a sample of unobscured Active Galactic Nuclei based on a sample of AGN that has been observed with *Suzaku* by Walton et al. (2013). According to the paradigm of 'bare' AGN we can observe the innermost part of an accretion flow surrounding a supermassive black hole, where an X-ray continuum source can be seen directly and reprocessed by the optically thick accretion disk. The most apparent line feature of this reflection is the line of fluorescent Fe $K\alpha$ -emission. In the region close to the event horizon, this feature is distorted by gravitational redshift, Doppler shift and light bending in a strongly curved spacetime. From the shape of the reflected spectrum and especially the broadened iron line, information on the accretion disk, the black hole and the X-ray source can be recovered. The reflection spectrum is most notably determined by the ionization and inclination of the accretion disk and the spin of the supermassive black hole.

This sample study focuses on the geometry of the primary radiation source. Compared to the mentioned study, we vastly improve on spectral range and data quality by using combined *XMM-Newton* and *NuSTAR* observations of a subset of 12 unobscured AGN. On these data we use an internally consistent model of a point-like X-ray continuum source along the rotation axis of the accretion disk, this setup is called lamppost geometry. In comparison we apply the commonly used empirical model of an accretion disk with a radial emissivity profile. We use the existing implementations RELXILLP respectively RELXILL of these models. The use of the lamppost model opens the possibility to directly measure the height of the radiation source above the accretion disk. Moreover, we distinguish between a lamppost model, where the intensity of the reflected continuum is fitted freely, and a variant where this 'reflection fraction' is derived from the height of the source. To measure the physical model parameters from the subtle features of reflection, we first perform a light-curve analysis to handle spectral variability. We individually account for phenomena in the soft X-ray spectral range of each source and discuss the issues brought up by cross-calibrating data from the two detectors.

A direct comparison between our results and the Walton et al. study shows that the inclusion of the high energy *NuSTAR* data leads to a systematic deviation in the measured physical parameters. We generally measure a harder primary X-ray continuum, as well as stronger accretion disk ionization and find black hole spins close to the physically allowed maximum of $a = 0.998$. Our datasets are generally well-explained by a lamppost geometry model. The comparison between the free reflection fraction model and the completely self-consistent model shows, that both models reproduce the data at comparable statistics. However, with the self-consistent model we can rule out unphysical solutions and avoid degeneracies in the already complex parameter space. Finally, we present source height values for 9 sources, which we find generally close to the event horizon at an average of $4 r_g$.

Contents

1	Motivation	8
2	Active Galactic Nuclei	9
2.1	The Unified Model	10
2.2	Black Holes	12
2.3	Accretion	14
2.4	Radiation Processes	16
2.4.1	Broadband X-ray Spectrum	16
2.4.2	Continuum Emission	17
2.4.3	Broadband Reflection Spectra	19
2.4.4	$K\alpha$ emission lines	20
2.4.5	Relativistic Reflection	21
2.5	Source Geometry	22
3	Instruments	24
3.1	Wolter telescopes	24
3.2	XMM-Newton	25
3.3	NuSTAR	26
4	X-ray Data Analysis	28
4.1	CCD event patterns	29
4.2	χ^2 -Statistics	30
4.3	Parameter Estimation	31
5	Extraction and model details	32
5.1	Sample Selection	32
5.2	Extraction	33
5.3	Light Curves	34
5.3.1	Simultaneous Observations	34
5.3.2	Hardness ratio	35
5.3.3	Non-simultaneous Observations	35
5.4	Spectrum Cross Calibration	37
5.5	Modelling	39
5.6	Comparing reflection models: Ark 120	41
6	Sample Analysis	43
6.1	Model I: Relxill - Parameters	43
6.2	Model I: Relxill - Residuals	44
6.3	Model I: Individual source details	45
6.4	Model II: Relxillp - Parameters	46
6.5	Model III: Relxillp (self-consistent) - Parameters	47
6.6	Model II: Relxillp - Residuals	48
6.7	Model III: Relxillp (self-consistent) - Residuals	49
6.8	Spectral component decomposition	50
6.9	Individual source results	52
6.10	χ^2 -Landscapes	53
6.11	Cross Validation of Simultaneous Observations	56
7	Sample discussion	58
7.1	Parameter correlations	58
7.2	Comparison to the Walton (2013) sample	59
8	Conclusions and Outlook	61
9	Bibliography	64
	Appendices	68

1 Motivation

Active Galactic Nuclei (AGN) are one of the large and promising frontiers of modern astrophysics. As one of the most extreme environments in astrophysics, they feature connections to many fields of astro- and particle physics. Firstly, evidence is overwhelming that AGN are actual, observable astrophysical black holes. Thus they are a perfect place to observe and study general relativistic effects and to test increasingly sophisticated models for the behaviour of matter and radiation in regions of extreme gravity (Rees, 1984). As launching points of galaxy scale astrophysical jets, AGN serve as natural particle accelerators and present an opportunity to study high energetic processes of the standard model in a natural source. Detections of high energy neutrinos lie well within the realm of possibility, as demonstrated by (Kadler et al., 2016). AGN jets are also one candidate source for the high energy part of the cosmic particle radiation (Pierre Auger Collaboration et al., 2007), a phenomenon that has a direct impact on earth's atmosphere and biosphere.

Moreover, AGN are multi-wavelength emitters from radio to γ -rays. From the synchrotron radio emission of jets, across the infrared, optical and UV emission of accretion disks up to inverse Compton produced X-rays and γ -rays. They offer a unique possibility to test and cross-validate matter-radiation interaction models and observational methods across the whole electromagnetic spectrum (Richards et al., 2006).

These efforts also pay off in the field of cosmology. Amongst AGN are the farthest, oldest and most luminous while constantly radiating objects in the sky. Cosmological redshifts are measured at up to $z \sim 7$, corresponding to a universe age of 0.8 Gyrs (Mortlock et al., 2011). As cosmic lighthouses abundant throughout the history of the universe, they can be used to trace matter and structures back to the emergence of the first galaxies. Once properly calibrated, AGN might even give a new standard candle (Bentz et al., 2013) to complement Supernova measurements of cosmological distances.

The evolution of an AGN seems to be deeply connected to its host galaxy and even larger scale structures (compare Fig. 1). Recent studies on AGN feedback like those of Fabian (2012); Harrison et al. (2014) have shown that jets, winds and radiation of AGN have a significant impact on their host galaxy's interstellar medium and star formation. Even when investigating structure formation on cosmological scales, Sijacki et al. (2007) have concluded that AGN feedback has to be taken into account.

Lastly, our own Galaxy houses a supermassive black hole at its center (Ghez et al., 2008), which turns out to be difficult to observe due to dust extinction in the Galactic plane. However, the recently Fermi-bubbles of the Milky Way discovered recently by Su et al. (2010) hint at a past phase of activity in the Galactic core.

We conclude that AGN are an important building block of the universe as well as a promising tool for the future of astrophysics. However, the central mechanisms driving the AGN leave many open questions. What is the dissipation mechanism allowing accretion of matter? How do the gas and dust structures surrounding the AGN form? What is driving the acceleration of jets? What is the primary source of high energy radiation?

We will study the last of these questions and take a look at the central accretion region of unobscured AGN. Here we see spectral features of X-ray radiation produced by an unknown source and reflected of the structures of surrounding material (Pounds et al., 1990). Investigating these features of reflected radiation, we hope to gain insight on the nature of the primary source.

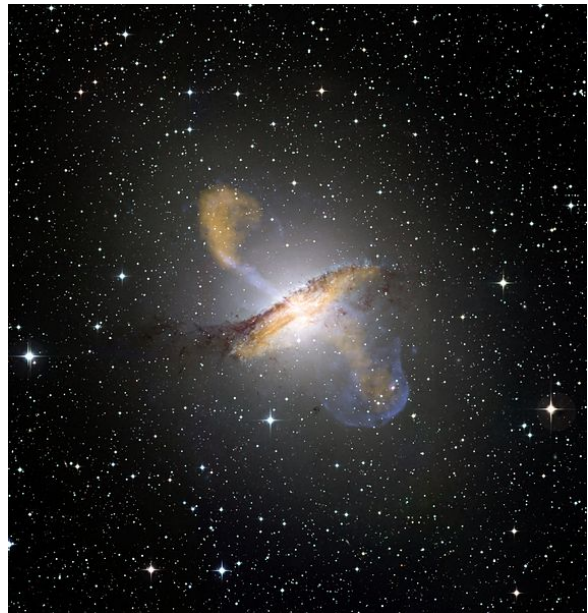


Figure 1: Composite image of the AGN host galaxy Centaurus A. Via galaxy sized jets the AGN feeds back into the cosmic matter cycle. Image Credit: ESO/WFI (Optical); MPIfR/ESO/APEX/A.Weiss et al. (Sub-millimetre); NASA/CXC/CfA/R.Kraft et al. (X-ray)

2 Active Galactic Nuclei

The most striking feature of Active Galactic Nuclei as astrophysical radiation sources is the ability to emit a large luminosity from a very small space volume and across a wide range of the electromagnetic spectrum. While all AGN are thought to sit at the center of a galaxy, many AGN are observed at distances where the host galaxy can no longer be resolved from its luminous nucleus. At luminosities from 1% to a factor of 10^4 above the typical field galaxy luminosity of 10^{44} erg s $^{-1}$ AGN contribute a significant fraction to the energy output of a galaxy (Krolik, 1999). This luminosity is strikingly illustrated in Fig. 2.

However, AGN are by far no homogeneous object class. Single objects may or may not show phenomena like broad or narrow optical emission lines, variability across the whole spectrum, extended radio emitting jets and strong or weak radio emission and polarization. This confusing multitude of features is attempted to be sorted by the unified model of Galactic Nuclei (Antonucci, 1993), which explains most of these features by assuming a complex, non-spherical source object observed from different angles.

To conduct a meaningful Analysis of AGN observational data, we need to get a handle on all processes of energy and radiation transfer that are part of the AGN unification model. Beginning at the central compact object, the supermassive black hole (SMBH), we will take a look at the process of accretion as a mechanism to produce extreme amounts of energy. From there, we will discuss effective mechanisms to turn a significant part of this energy into radiation to be sent to the observer.



Figure 2: Near infrared image of NGC 1566, a typical AGN hosting galaxy of type Seyfert I. The remarkably bright nucleus is clearly visible. Image Credit: ESA/Hubble & NASA

The shape of the spectrum in X-rays will be of special interest, and further the reprocessing of this radiation via reflection off dense clouds, Fluorescent line emission and light bending in the strongly curved spacetime close to the black hole. These are the features that will be central to the following data analysis as they will allow us to gain insight on the geometry of the primary X-ray source. The descriptions of this introduction section will generally follow the works of Krolik (1999), Frank et al. (2002) and Rybicki & Lightman (1986).

While there have been models and simulations for different geometries of the primary source (see, e.g., Wilkins & Fabian, 2012; Dauser et al., 2013; Dovčiak & Done, 2016), only for a few specific sources the actual location and extent of the primary source has been analysed. Direct measurements of the accretion disk emissivity profile for the sources 1H0707–495 (Fabian, 2012) and Mrk 335 (Parker et al., 2014) show a radially extended emission region, but generally measurements reveal a low height and compact source along the rotation axis of the system (Keck et al., 2015; Svoboda et al., 2012) (Lamppost geometry). It has been shown that such a compact emitting region is required in order to produce an observable relativistic smearing of the reflection spectrum (Dauser, 2014; Fabian et al., 2015).

In the analysis part of this work we will test this lamppost paradigm using a sample of high quality data and elaborate physical models of relativistic reflection. First we present the sample of 12 sources and treat the extraction and reduction of its spectral data acquired with *XMM-Newton* and *NuSTAR*. To get workable spectra we will take a look at the sample's light-curves and perform a cross-calibration via a simple analytical model. Only then we can examine the broadband spectra using physical models. All of these sources are well-known to show strongly distorted iron lines from the work of Walton et al. (2013), from now on referred to as Walton (2013). Most of our sources are individually well-studied in the X-ray range, so our goal is not a detailed treatment of complex absorption features or the multiple possibilities to explain soft X-ray excess emissions. Our intention is to fit a physical model of lamppost reflection consistently to a varied sample of high quality data. Exemplary, we perform a deeper analysis of the source Ark 120 comparing several models of relativistic reflection. Then we extend this analysis to the complete sample. We figure out individual complexities of the sources and perform fits of three variant models of relativistic reflection. The fit results are investigated via decomposition into model components, mapping of the χ^2 -landscape and a final sample spanning comparison of the physical parameters.

2.1 The Unified Model

The first general distinction of AGN classes can be made into radio-loud and radio-quiet ones. Radio-loud AGN produce jets observable on a large scale via their interactions with the intergalactic medium. Accordingly radio-quiet are characterised by the lack of these features and are found to be constituting $\sim 90\%$ of the AGN population (Wilson & Colbert, 1995). Recent studies concluded that this dichotomy is unrelated to the host galaxy morphology and the behaviour of the optical AGN counterpart (Dunlop et al., 2003; Best et al., 2005), but might be connected to galaxy merging events (Chiaberge et al., 2015). As this work focuses on the high energy part of AGN emission, we will not discuss the radio-loud case but rather point to the work of e.g. Urry & Padovani (1995); Best & Heckman (2012).

The optical to X-ray part of radio-quiet AGN phenomenology can be distinguished into the following classes. They are named after Carl Seyfert (1943), who was the first to find galaxies that exhibit strong optical emission lines:

Seyfert I: The first class is characterised by a strong, variable continuum featuring narrow emission lines of widths corresponding to a redshift of $\sim 10^3 \text{ km s}^{-1}$. Line positions correspond to the transitions of Hydrogen, Helium, Oxygen and Nitrogen (Osterbrock & Pogge, 1985). These narrow lines are surrounded by broad wings of $\sim 10^4 \text{ km s}^{-1}$ (compare Fig. 3). The advent of X-ray astronomy revealed also a strong X-ray component (Antonucci, 1993).

Seyfert II: Seyfert II galaxies are differentiated by their weaker continuum and the lack of broad lines. They also exhibit strong source intrinsic obscuration with hydrogen equivalent column densities of $N_H > 10^{23} \text{ cm}^{-2}$ as determined by e.g. Risaliti et al. (1999) from X-ray data.

Quasi-Stellar Objects (QSO): Is used synonymously to radio-quiet quasar. The term originated historically for objects that appear point-like in the optical and shine at magnitudes similar to that of a Galactic field star. The classification criteria of a QSO are the same as those of a Seyfert I, with the only difference being that for a QSO the host galaxy is not visible. As this distinction relies mainly on the contrast and resolution abilities of the observing telescope, it is not considered practical anymore (Krolik, 1999).

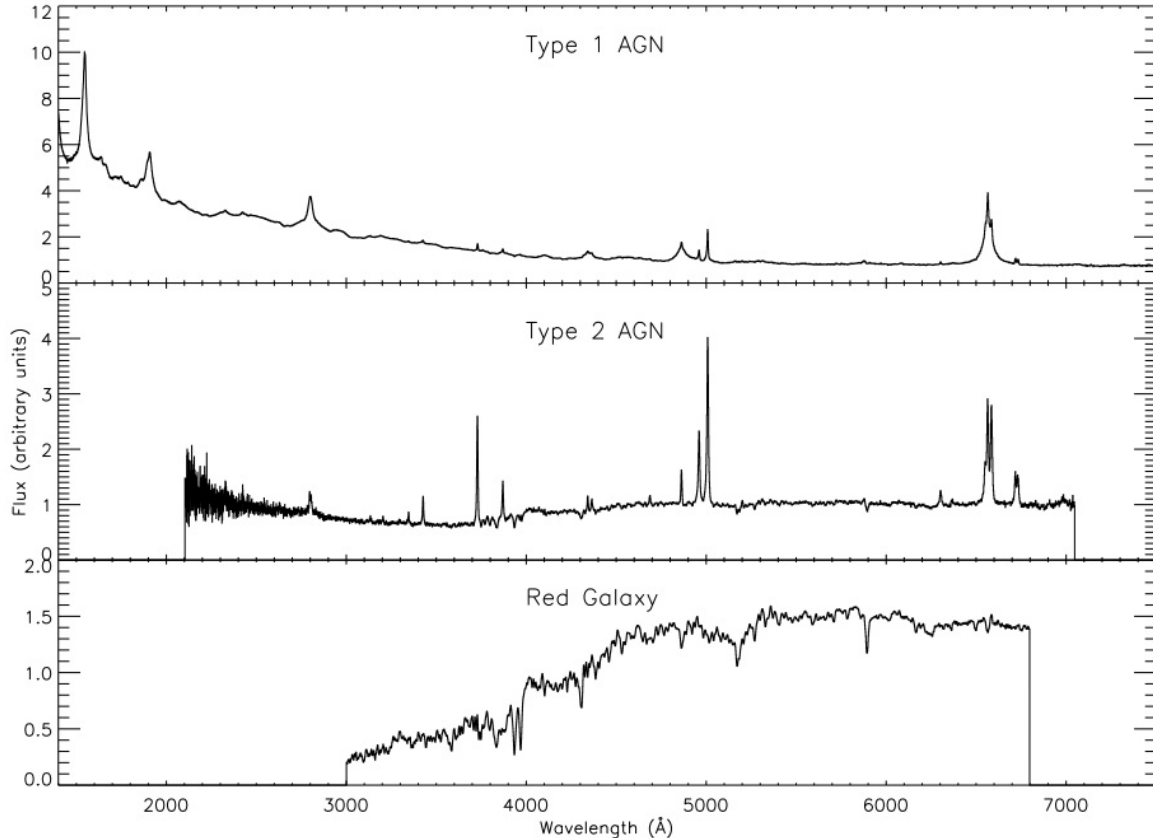


Figure 3: Typical optical spectra of the two different Seyfert classes and a non-AGN galaxy. Image: Trump et al. (2007)

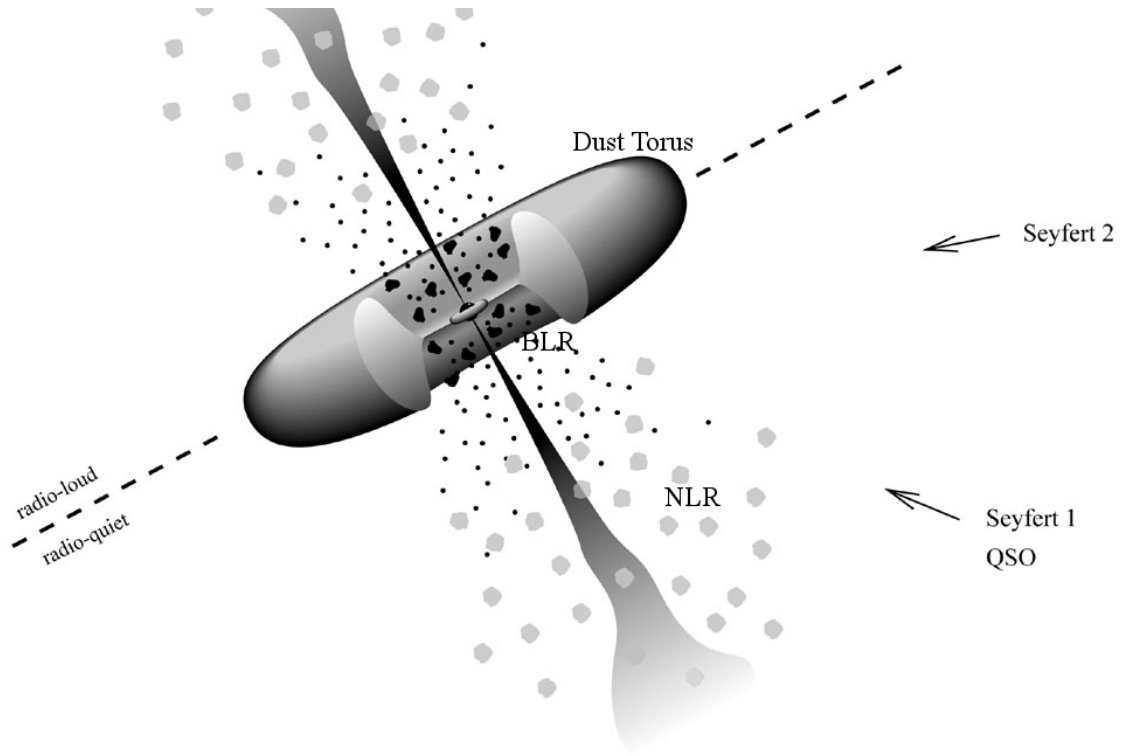


Figure 4: Schematic of the unified AGN model, viewing the accretion disk, dust torus, close and distant clouds and jets. Image: Urry & Padovani (1995), modified

After Krolik (1999), the paradigm unifying these observations can be summarized as follows: A supermassive black hole is accreting gaseous matter in an opaque disk. As it is moving towards the center the material is heated via dynamical friction. The thermal energy gained in the accretion process is radiated as blackbody radiation in the optical. Part of the energy is processed into a power law continuum across the whole electromagnetic spectrum. Perpendicular to the disk jets of relativistic charged particles leave the system. The conversion processes in this central radiation source will be detailed in section 2.4.

Close to this region, in the broad line region (BLR), clouds are orbiting at high speeds and get ionized by the central radiation source. The moving ionized material emits UV-optical lines at different redshifts. In sum these appear accordingly as broadened emission lines (Rees et al., 1989).

Parsecs from the center, the system is embedded into an opaque torus-like structure of dust and gas. Depending on the viewing angle, the cloud torus may occlude the view on the primary spectrum and the broad line region. Also on these scales the narrow line region is assumed (NLR) where slow moving low density clouds produce narrow emission lines (Peterson & Wilkes, 2000). In some cases, this gas might be flowing away from the accretion disk, driven by radiation pressure (Konigl & Kartje, 1994).

In the Seyfert I case, we view the object under a high angle to the accretion disk, and the central radiation source, NLR and BLR all contribute to the spectrum. In the Seyfert II case, the central engine and BLR are obstructed by the torus. The continuum is only seen strongly extinguished and in reflections, while the line emission from the NLR can still be observed. A schematic is shown in Fig. 4.

We have to keep in mind that this is a very simplified model, and that recent studies support the picture of a more filamented torus, clumpy disk winds and an accretion inflow starting at Galactic scales. An up-to-date review can be found in Netzer (2015).

2.2 Black Holes

One of the most exciting prospects of AGN research is the possibility to not only find evidence for black holes, but even measure their inherent properties. We will introduce some of the basic results of General Relativity applied on the Schwarzschild and Kerr black hole. In theoretical considerations regarding General Relativity the gravitational constant and velocity of light are typically set $G = c = 1$. The typical measure of length is the gravitational radius $r_g = GM/c^2$. Applying these conventions the units of length and mass are the same.

The Schwarzschild black hole

The considerations of this section follow Krolik (1999). The solution of the Einstein (1916) field equations for the spherically symmetric, time-steady, non-rotating point-mass was found by Karl Schwarzschild (1916). He showed that particle trajectories can still be calculated using the classical formulation of the two-body problem and a correction term to the Newtonian effective potential V_N :

$$V_N(r) = -M/r + L^2/(2r^2) \quad (1)$$

Where L is the angular momentum and M the central mass. For a test particle, it yields the Keplerian conic orbits. The General relativistic correction adds the two terms:

$$V_{GR}(r) = V_N(r) + 1/2 - ML^2/r^3 \quad (2)$$

The last correction term implies the precession of a bound orbit's perihelion, if the orbit approaches the central mass closely.

It is also instructive to look at the lapse function $\alpha = \sqrt{g_{tt}}$, which derives from the time component of the metric g . The lapse function gives the ratio between the coordinate time dt measured far from the source in flat space and proper time ds for an observer stationary at r .

$$ds = \sqrt{1 - \frac{2M}{r}} dt \quad (3)$$

Assume a particle oscillating close to the event horizon at $r \rightarrow 2M$, the duration of one oscillation is ds . According to the lapse function, a distant observer sees the oscillation taking a much larger time dt , so an emitted photon appears at lower frequency. This effect is called gravitational redshift.

For the AGN case, we are mainly interested in photon trajectories originating close to the black hole. As the photon velocity is fixed and the metric is spherically symmetric, the trajectories are predetermined by the starting radius and the angle ψ to the radially outward direction. The main turning point is at $r = 3M$. At larger radii, outward directed photons are always escaping, at smaller radii inward directed photons are certainly captured. The other cases are decided at the boundary

$$\sin \psi = \frac{3\sqrt{3}M}{r} \sqrt{1 - \frac{2M}{r}} \quad (4)$$

From this expression, we also see that at $r_{EH} = 2M$ no escaping trajectories are possible which is the definition of the event horizon or Schwarzschild-radius. Note that this is also the location where the lapse function approaches infinity.

Another interesting property of the Schwarzschild black hole is the radius of marginal stability r_{ms} . From the potential viewpoint, a stable orbit requires the effective potential to have a local minimum outside the central object's surface. In the Schwarzschild effective potential, the smallest radius where such a minimum exists is $r_{ms} = 6M$ (depending on L). It is implied that at smaller radii no stable orbits are possible and particles inevitably plunge into the event horizon.

The Kerr black hole

The solution of the Einstein Field equations for the case of an uncharged rotating mass was found by Roy Kerr (1963). The angular momentum of the black hole is expressed via the spin parameter a , fulfilling the relation $J = aM$. The limits of a are 0, meaning the Schwarzschild case, and 1 where any increase in angular momentum will increase Energy and therefore mass by the same amount. In fact, a significant fraction of the black hole population is expected to have angular momentum close to the upper limit (Krolik, 1999). As black hole growth is assumed to happen via disk accretion (see sect. 2.3), mass growth automatically corresponds to growth in angular momentum. The angular momentum of matter at r_{ms} is directly transferred to the black hole. With an initial mass m_i , a black hole can be assumed to rotate maximally after disk-accretion of a rest mass of $\Delta M = 1.85 M_i$ (Bardeen, 1970).

However, the extreme case of $a = 1$ can not be physically realized as was shown by Thorne (1974) using a model that includes a radiating disk. In this model, the capture cross-section of the black hole for photons carrying positive angular momentum is smaller than for negative angular momentum photons. The result is a net braking effect that starts to dominate at $a = 0.998$, preventing any further angular momentum build-up.

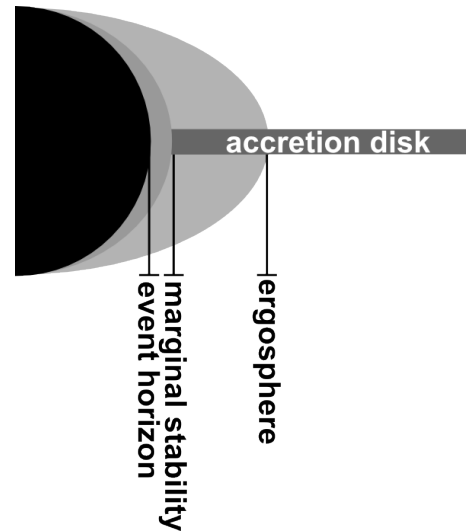


Figure 5: Schematic of a Kerr black hole for $a = 0.998$.

A characteristic feature of rotating black holes is the ergosphere, an ellipsoidal region slightly larger than the event horizon limited by the surface

$$r_{\text{ergo}} = M + \sqrt{M^2 - a^2 \cos^2 \theta} \quad (5)$$

Inside this surface rest frames stationary with respect to the far field are forbidden. The phenomenon of rest frames moving along with the rotation of the black hole is also called frame-dragging. The event horizon is shrinking with increasing black hole spin:

$$r_{\text{EH}} = M + \sqrt{M^2 - a^2} \quad (6)$$

and touches the ergosphere at the poles. The radius of marginal stability strongly depends on a . Where in the Schwarzschild case $r_{\text{ms}}(a = 0) = 6M$, for the rotating black hole we must distinguish the prograde and retrograde orbit. For prograde orbits r_{ms} moves inward with increasing a . The dependency is shown in Fig. 6, for the full analytical expression see Krolik (1999).

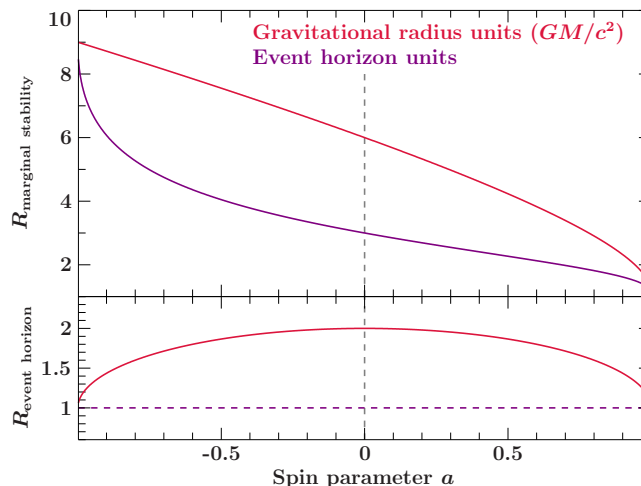


Figure 6: Spin dependency of the radius of marginal stability and the equatorial event horizon radius for a Kerr black hole.

2.3 Accretion

To power the immense luminosity comparable to that of a galaxy from a region smaller than parsecs, an AGN needs a very efficient energy conversion process. The energetics alone allow to rule out all chemical and nuclear processes (Frank et al., 2002). The only feasible energy source left is accretion of matter into a deep gravity well. Some important characteristics of accretion processes can already be examined using just a spherically symmetric matter distribution (consisting only of hydrogen) without any angular momentum, flowing steadily onto a central object of radius R and mass M . This case is named spherical or Bondi (1952) accretion.

Spherical Accretion

Following Frank et al. (2002), we assume that given enough time all kinetic energy of the infalling material will be converted to heat and radiated away. The luminosity can be calculated directly from the gravitational potential at the accreting objects surface and the accretion rate of matter \dot{m} :

$$L = G \frac{\dot{m}M}{R} \quad (7)$$

Now we consider the interaction of the central radiation source with the infalling material. Each hydrogen atom feels a gravitational force of $F_G = GM(m_p + m_e)/r^2$, but also an outward radiative force caused by the radiation flux S of $F_{\text{Rad}} = S(r)\sigma_T/c$. The photons mainly interact with electrons, but as long as they are bound to the proton the force acts on the whole atom. Due to these counteracting forces, we reach an equilibrium state where the radiation slows down the infalling material, effectively limiting the accretion rate \dot{m} . The resulting maximum luminosity is reached when $F_G = F_{\text{Rad}}$. It is determined only by the central mass and is called Eddington luminosity:

$$L_{\text{Edd}} = \frac{4\pi GMm_p c}{\sigma_T} \quad (8)$$

At a typical SMBH mass of $10^7 M_\odot$, this relationship yields a maximum luminosity of $1.5 \times 10^{45} \text{ erg s}^{-1}$ ($4 \times 10^{11} L_\odot$). However, it is assumed that the matter drops onto a surface, allowing enough time to convert all gravitational energy into radiation. Specifying the central object as black hole, we have to consider the existence of an event horizon. All kinetic energy contained in the mass flow in the moment it passes the event horizon can not be radiated away. The accretion luminosity is limited to the fraction η of the produced energy that can be radiated away before reaching the event horizon.

$$L = \eta G \frac{\dot{m}M}{R} \quad (9)$$

This accretion efficiency η strongly depends on details of the accretion process and space-time close to the black hole. It can also be seen as fraction of accreted material rest mass that is converted to radiation, or $L = \eta \dot{m}c^2$.

Accretion disks

In practice, incoming material will not be directly dropping into the central object, but will be carrying some angular momentum, for example from the rotation of the host galaxy. When the infalling gas clouds are dense enough, friction and gravitational interaction will force them into a common plane of rotation. An accretion disk in steady flow will have its gas masses moving on circularized Keplerian orbits. In the following considerations of accretion disks we will follow the derivations found in Frank et al. (2002); Paczynsky & Wiita (1980); Pringle (1981). The structure perpendicular to the disk will be governed by hydrostatic equilibrium and can be considered independent to the movement of the disk plane. The circular velocity of a ring of gas is given by the Kepler velocity:

$$v_\phi = R\Omega = R\sqrt{\frac{GM}{R^3}} \quad (10)$$

Matter is moving inwards radially at a drift velocity v_r small compared to the orbital velocity. The matter content of the ring is described by the surface density $\Sigma(R)$ of mass per area, so that a ring extending from R to $R + \Delta R$ contains a mass of $\Delta m = 2\pi R \Delta R \Sigma(R)$ (neglecting quadratic terms).

Through this ring, material is drifting from respectively into the neighboring rings at an accretion rate of $\dot{m} = 2\pi v_r(R)R\Sigma(R)$ constant throughout the disk. In and outflow sum up to the change of mass of the ring:

$$\frac{\partial}{\partial t} \Delta m = 2\pi v_r(R)R\Sigma(R) - 2\pi v_r(R + \Delta R)(R + \Delta R)\Sigma(R + \Delta R) = 0 \quad (11)$$

Requiring a steady accretion disk we set the change of mass to zero and simplify the remaining expressions to:

$$0 = \frac{\partial}{\partial R} R \Sigma v_R \quad (12)$$

This condition expresses conservation of mass and mass flow. As angular momentum is conserved on a Keplerian orbit, we need to consider a mechanism of angular momentum transport to actually allow mass to flow inward. In this simple model, the mechanism is viscous friction between layers of accreting material. We can define the angular momentum of a ring as $\Delta L = \Delta m R^2 \Omega = 2\pi R \Delta R \Sigma(R) R^2 \Omega$. Analogous to the mass flow, we can calculate the transport of angular momentum carried with the mass. We add an additional term of $G(R)$ for the torque that is exerted by a ring onto its neighboring rings due to viscous friction:

$$\frac{\partial}{\partial t} \Delta L = 2\pi v_R(R) R^3 \Sigma(R) \Omega - 2\pi v_R(R + \Delta R) (R + \Delta R)^3 \Sigma(R + \Delta R) \Omega (R + \Delta R) - G(R) + G(R + \Delta R) \quad (13)$$

which similarly to Eq. 11 reduces to:

$$0 = \frac{\partial}{\partial R} R^3 \Sigma v_R \Omega - \frac{1}{2\pi} \frac{\partial G}{\partial R} \quad (14)$$

Combining the mass and angular momentum transport equations, we relate the torque, density and velocity profiles.

$$R \Sigma v_R \frac{\partial}{\partial R} (R^2 \Omega) = \frac{1}{2\pi} \frac{\partial G}{\partial R} \quad (15)$$

We now need a more explicit expression for the torque. Therefore we assume a force of friction F_v acting along the whole ring boundary, so $G(R) = R F_v \cdot 2\pi R$. This friction is in a most simple assumption proportional to density and boundary velocity, so $F_v = \nu \Sigma \Delta v_\phi = \nu \Sigma R \frac{\partial \Omega}{\partial R}$. The proportionality constant ν is called viscosity.

$$G(R) = 2\pi R^3 \nu \Sigma \frac{\partial \Omega}{\partial R} \quad (16)$$

The exact source of this viscosity is still debated. A realistic assumption is that the viscosity is caused by turbulence and magnetic fields. These are justified by the expectation of at least partially ionized disk material and supersonic motion. The exact working of this mechanism as well as a usable parametrization are still subject of debate. In the way of Shakura & Sunyaev (1973) we treat the viscosity simplistically as a constant. Inserting the torque equation 16 into equation 15 we get the following diffusion equation for the surface density:

$$\frac{3}{R} \frac{\partial}{\partial R} \left[\sqrt{R} \frac{\partial}{\partial R} \nu \Sigma \sqrt{R} \right] = 0 \quad (17)$$

This differential equation can be solved assuming an inner boundary R_{in} after Frank et al. (2002) to obtain the following surface density profile:

$$\nu \Sigma = \frac{\dot{m}}{3\pi} \left[1 - \sqrt{\frac{R_{\text{in}}}{R}} \right] \quad (18)$$

The transfer of kinetic energy into heat due to viscous friction is given by the dissipation $D(R) = \frac{1}{2} \nu \Sigma \left(R \frac{\partial \Omega}{\partial R} \right)^2$ (Pringle, 1981). Using the above equation it is:

$$D(R) = \frac{3}{4\pi} \frac{GM\dot{m}}{R^3} \left[1 - \sqrt{\frac{R_{\text{in}}}{R}} \right] \quad (19)$$

Assuming that all of this heat will be radiated away, we can integrate the dissipation across the surface of the disk to get the luminosity

$$L = \int_{R_{\text{in}}}^{\infty} D(R) 2\pi R dR = \frac{1}{2} \frac{GM\dot{m}}{R_{\text{in}}} \quad (20)$$

Comparing this result to equation 9, we see that the prefactor corresponds to an accretion efficiency $\eta = 0.5$ when accreting matter to the radius R_{in} . Realistically, accretion efficiencies of black holes are lower than this value as the disk becomes unstable once it reaches the radius of marginal stability and the material quickly falls into the event horizon (Abramowicz et al., 1978). Without much time to radiate, energy contained in the plunging matter is trapped beyond the event horizon. More detailed calculations yield the efficiency of a Schwarzschild black hole at 0.057. For Kerr black holes, the efficiency rises with black hole spin. This is due to the shrinking of the radius of marginal stability (compare Fig. 6) and the event horizon, leaving infalling matter more time to radiate. At maximum spin, the efficiency rises up to 0.42 (Thorne, 1974).

2.4 Radiation Processes

Having discussed the accretion process powering an AGN, we are left with the primary energy in the form of kinetic and thermal energy of a flow of ionized gas. It is now of interest how this energy is converted into electromagnetic radiation and distributed across the spectrum.

2.4.1 Broadband X-ray Spectrum

We list a short overview for the components that are generally observed in the X-ray spectra of AGN. The physical models for the individual spectral components will be explained in later sections, being our main tool to extract information about the source objects from the spectrum. For an extensive discussion on the topic see also Mushotzky et al. (1993).

The basic model is that of a primary source of X-ray radiation that sits close to the center of a unified model disk-torus structure. The light reaches the observer directly and in reflection as illustrated in Fig. 7.

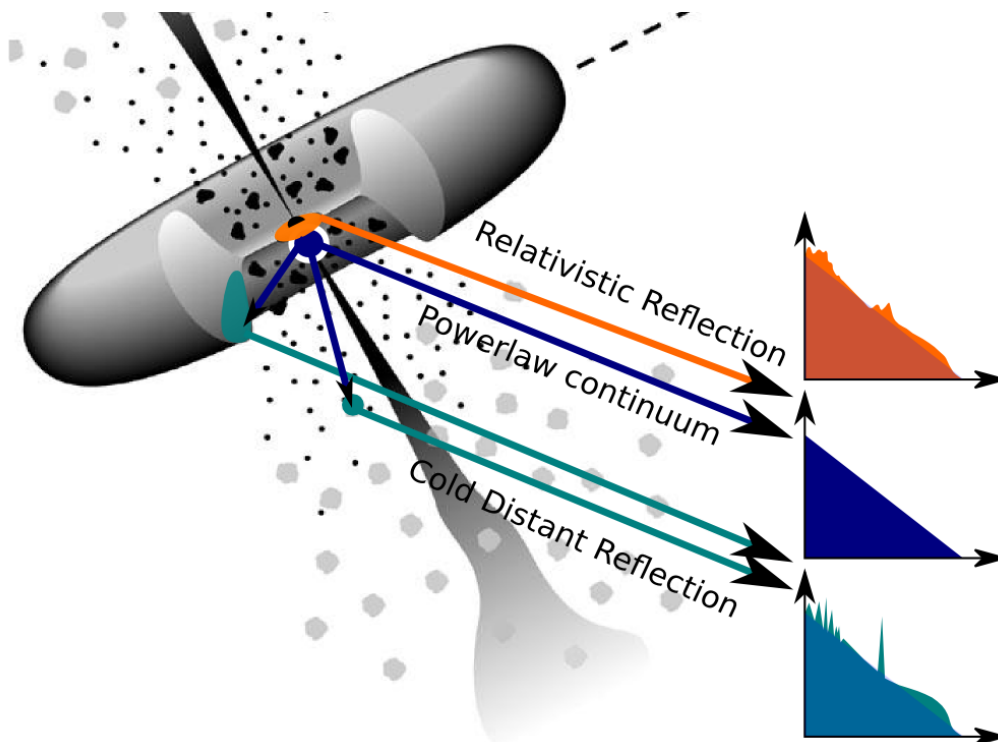


Figure 7: Schematic drawing of spectral components as observed and their physical origin in an unabsorbed case. The cold distant reflection (CDR) is composed of soft narrow line emission and a hard Compton scattering hump. The relativistic component shows the same but distorted features. Image: Urry & Padovani (1995), modified

Power law continuum: A hot electron population produces a broad range power law spectrum. Possible mechanisms are Comptonization of UV-seed photons or synchrotron emission from movement in magnetic fields. This primary radiation source is assumed to be in parts absorbed and in parts reflected from the surrounding clouds. The primary continuum has been observed to vary on timescales of days (McHardy et al., 1990). For such variability to happen, all parts of the source must be causally connected on this timescale, so it can be inferred that the primary spectrum must come from a very confined region much smaller than light-days (Mushotzky et al., 1993).

Fluorescent line emission: Fluorescent line emission of a large column density of X-ray illuminated matter is mainly seen in the Fe-K α (6.40 keV), Fe-K β (7.06 keV) and Ni-K α (7.48 keV) line with the Fe-K α line being the dominant line. The illuminated material is generally assumed to be that of the accretion disk and torus (George & Fabian, 1991).

Relativistic broad lines: The same process responsible for narrow fluorescent emission lines also happens deep into the potential well of the SMBH, where gravity redshift, relativistic Doppler effect and gravity lensing distort individual line profiles across an energy range of several keV (Nandra et al., 1997).

Compton hump: At energies above 10 keV, the reflectivity caused by Compton scattering in gaseous material reaches its maximum. This causes the spectrum to seemingly steepen at high energies. (George & Fabian, 1991)

Soft excess: At soft X-ray energies, many AGN spectra show a steepening of the power law. Several mechanisms producing or redistributing radiation into this range are debated, and in some cases more than one might contribute to this part of the spectrum. One possibility is the upper tail of the accretion disks black-body UV spectrum reaching into the soft X-ray range, called the "big blue bump". Also a large part of the fluorescent line emission of reflection spectra lies in this energy range. Another contribution might come from Comptonized emission of Compton thick gas in the accretion disk (Done et al., 2012).

Absorption: Most AGN show signs of absorption which mainly suppresses the spectral flux below 2 keV, but also at the Fe-K-shell energy a significant absorption edge is found. Generally the column densities of absorbing material observed in Seyfert IIs are much larger than for Seyfert Is (Turner & Pounds, 1989). Often-observed variability in the obscuring hydrogen equivalent column is another cause of variability in AGN X-ray spectra (Mushotzky et al., 1993).

Warm Absorption: Many AGN show strongly Doppler shifted photoelectric absorption lines around 1 keV typical for hot, ionized gas like OVII and OVIII, but also in the iron line complex. Commonly these are attributed to high velocity radiation driven winds intervening the line of sight (George et al., 1998).

2.4.2 Continuum Emission

One very important interaction process between matter and radiation in the X-ray spectral range is the scattering of photons off electrons - the Compton effect. Here we follow the description found in Rybicki & Lightman (1986).

First we consider an electron that is practically at rest and impacted by a photon at energy $h\nu$. The photon energy is assumed to be much lower than the electron rest mass $m_e c^2$ so that it is scattered as a wave at unchanged wavelengths. This process is called Thomson scattering. The differential cross sections is given by the following equations:

$$\frac{d\sigma_T}{d\Omega} = \frac{1}{2} r_0^2 (1 + \cos^2 \theta) \quad (21)$$

Integration over the full solid angle yields the total cross section of $\sigma_T = \frac{8\pi}{3} r_0^2$, where r_0 is the classical electron radius (Rybicki & Lightman, 1986).

In the X-ray regime however, photon energies are large enough that recoil on the electron becomes a concern, so in a quantized view of elastic scattering the photon undergoes an energy change from an initial Energy E_{in} to a final E_{fi} . From energy and momentum conservation, one can derive the energy transfer:

$$E_{fi} = \frac{E_{in}}{1 + \frac{E_{in}}{m_e c^2} (1 - \cos \theta)} \quad (22)$$

In a classical view, this energy transfer always happens from the photon to the electron. The differential cross-section can only be found from a full Quantum electrodynamic treatment and is described by the Klein-Nishina-formula (Heitler, 1954):

$$\frac{d\sigma}{d\Omega} = \frac{r_0^2}{2} \frac{E_{fi}^2}{E_{in}^2} \left(\frac{E_{in}}{E_{fi}} + \frac{E_{fi}}{E_{in}} - \sin^2 \theta \right) \quad (23)$$

In the case of $E_{in} \simeq E_{fi}$ this equation reproduces the cross section of Eq. 21. For larger energy changes the cross section gets smaller, implying that Compton scattering gets inefficient for higher photon energies.

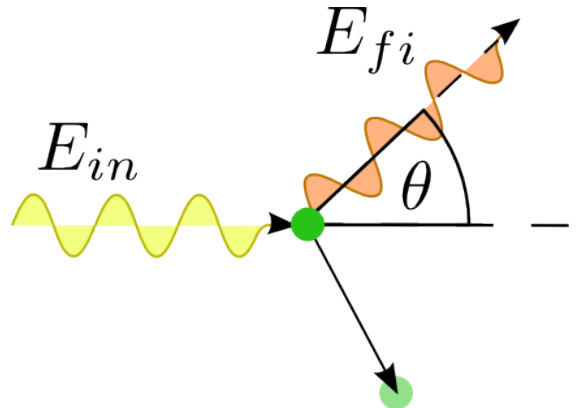


Figure 8: Schematic of the Compton scattering process.

Now we generalize to the case of an electron moving at relativistic velocity β in the lab frame before the scattering. To get the complete energy transfer, we can first transfer to the electron rest frame (marked by ') apply the energy transfer according to equation 22 and then to transfer the back to the lab frame. During each frame of reference transfer, we apply the relativistic Doppler shift formula on the photon. We transfer the photon energy to the electron rest frame:

$$E'_{\text{in}} = E_{\text{in}}\gamma(1 - \beta \cos \theta) \quad (24)$$

Apply the energy transfer ΔE :

$$E'_{\text{fin}} = E'_{\text{in}} - \Delta E \quad (25)$$

And transfer back into the lab frame:

$$E_{\text{fin}} = E'_{\text{fin}}\gamma(1 + \beta \cos \theta) \quad (26)$$

Consider the case of a low energy photon and a relativistic electron. From Eq. 21 we see that if $E_{\text{in}} \ll m_e c^2$ the energy transfer gets small, so $\Delta E \simeq 0$ while for the relativistic electron $\gamma > 1$. Assuming large angle scattering $\cos \theta \simeq 0$ for equations 24 - 26 we immediately find that the photon energy roughly gains a factor of γ during each frame shift, so in total the photon energy grows by γ^2 (Blumenthal & Gould, 1970). We see that we can not only lose photon energy, but also transfer energy of moving matter to photons. This process is therefore called inverse Compton effect or 'upscattering'.

It is applied in astrophysical situations where there is a 'hot' population of high energy electrons that is illuminated by a lower energy photons. The most prominent cases where this condition is fulfilled are:

- In the hot electron plasma surrounding Galaxy clusters, illuminated by the cosmic microwave background. (Sunyaev-Zel'dovich-effect)
- In the particle shock front of a supernova.
- In an atmosphere of hot electrons above an accretion disk, illuminated by the thermal emission of the disk itself - the so called corona.

Now we take a look at the continuum spectrum that is produced by an electron population via this process. We first consider the case of a single electron illuminated by an isotropic photon distribution of energy density u_{ph} . This model is characterised by a transfer rate of energy from the electron to the photon field:

$$P_{\text{Compt}} = \frac{dE_{\text{rad}}}{dt} = \frac{4}{3}\sigma_{\text{T}}c\gamma^2\beta^2u_{\text{ph}} \quad (27)$$

To get the macroscopic energy transfer rate, we integrate this rate over the thermal Maxwell velocity distribution $N(\gamma)d\gamma = C\gamma^{-p}d\gamma$ of a gas of electron density n_e . Using the approximation $\gamma \simeq 1$, this yields:

$$P_{\text{Compt}} = \left(\frac{4kT}{mc^2}\right)c\sigma_{\text{T}}n_eu_{\text{ph}} \quad (28)$$

Illustrating that the inverse Compton effect is a process that effectively cools a hot electron plasma The cooling gets more efficient at higher electron temperature.

The energy spectrum of an isotropic photon distribution of arbitrary spectrum scattered off an isotropic thermal electron distribution was shown by Jones (1968) to be given by a power law distribution:

$$I(\epsilon)d\epsilon = I_0\epsilon^{-\frac{p-1}{2}}d\epsilon \quad (29)$$

This relation also holds if the electron distribution is no longer a power law. The electron gas has, however, to be optically thick for Compton scattering, which would be the case in a Shakura-Sunyaev accretion-disk. The fact that the spectrum of a thermal electron distribution is independent of the primary spectrum leaves the possibility for another radiation process. In the presence of a magnetic field, the primary spectrum could as well be produced by synchrotron emission, for an explanation on a similar level see Krauss (2013).

2.4.3 Broadband Reflection Spectra

Following George & Fabian (1991) and Krolik (1999), we now take a look at the spectrum that is produced in reflection of interstellar material.

We assume that AGN are surrounded by masses of cool, optically thick and intermediately ionized gas gathering in the accretion disk and torus structure (Pounds et al., 1990). The power law spectrum from Eq. 29 irradiates the surface of the structure and interacts mainly with free and bound electrons in a thin surface layer of several free path lengths. At energies below 10 keV, the photoelectric cross sections of different elements are large enough to absorb a significant part of the radiation. The opacity has a strong peak at the Fe $K\alpha$ -edge, the energy absorbed here gets re-emitted in the $K\alpha$ -line. Other elements abundant in interstellar matter are carbon, nitrogen, oxygen and neon causing absorption edges and fluorescent lines below 5 keV (Matt et al., 1993).

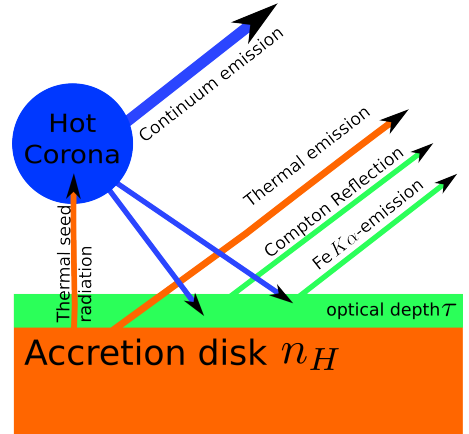


Figure 9: Flowchart of the different spectral components involved in X-ray reflection spectra.

With increasing energy, X-ray photons experience smaller Compton cross sections (compare section 2.4.2), leading to these photons penetrating deeper into the gas structure and scattering more frequently than low energy photons. The paths of incident photons > 30 keV are increasingly randomized and absorbed. The combination of low energy photoelectric absorption and high energy Compton scattering lead to an energy-dependent albedo with its maximum between 10 and 30 keV (Magdziarz & Zdziarski, 1995).

From the strength of the Fe $K\alpha$ -edge, the according fluorescent line and the Compton hump we can extract crucial information about the gas of the accretion disk. The equivalent width of the line in relation to the illuminating continuum strongly depends on the Iron abundance of the region. The energy position of the Iron line as well as the strength of photoelectric absorption depend on the ionization of the material (George & Fabian, 1991). The ionization state is quantified using the ionization parameter $\xi = 4\pi F/n_H$. Here n_H is the hydrogen equivalent number density of the material illuminated by the photon flux F . For the dependency of the reflection spectrum on ionization state, see Fig. 10. Here we see that reflectivity in the soft raises with ionization strength, as less atoms are available for photoelectric absorption. When observing a spectrum directly and in reflection, this effect leads to a flattening of the total spectrum.

We can expect that the ionization of the inner accretion disk mainly depends on the energy dissipation and therefore on the accretion rate (see Eq. 20). Assuming that the intensity of X-ray radiation is directly proportional to the disk thermal emission, Nandra et al. (1997) expect a proportionality of $\xi \sim M^3$.

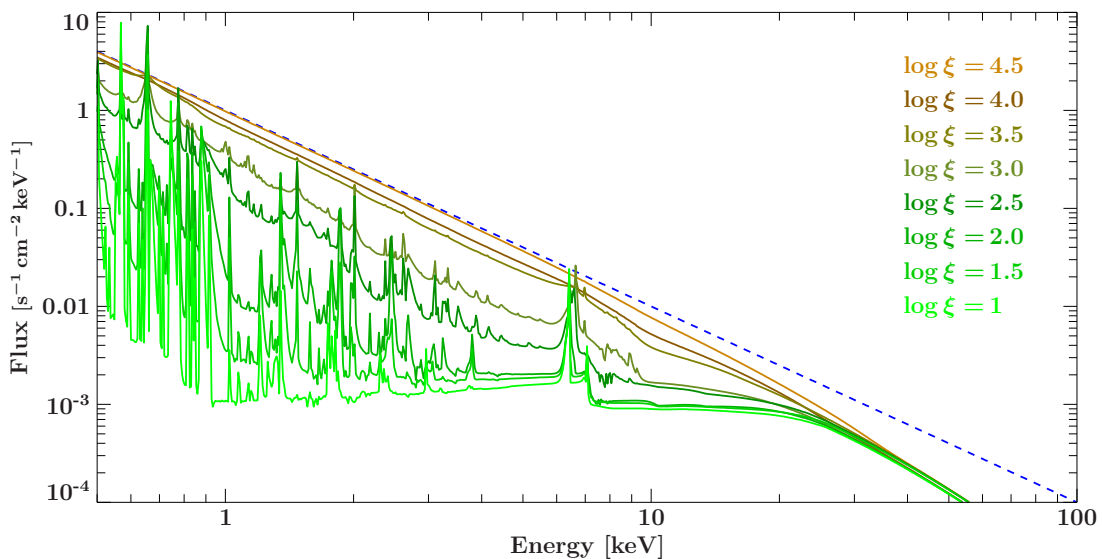


Figure 10: Power law spectrum (blue) reflected off differently ionized material. Calculated using the reflection table-model XILLVER(Garcia et al., 2013). The reflecting material goes from an unionized $\log \xi = 1$ (green) to completely ionized $\log \xi = 4.5$ (orange).

2.4.4 $K\alpha$ emission lines

The most prominent line feature in the X-ray spectral range is that of fluorescent iron $K\alpha$ -emission, due to the comparably high abundance of Iron in the interstellar medium and the large fluorescent yield of the respective line (George & Fabian, 1991). The emission process is initiated by photoelectric ejection of an Iron K-shell electron. In the central parts of accretion disks we expect Iron to be more abundant in the XXIII to XXV ionization states where the K-shell binding energies are shifted to between 8.47 and 8.76 keV (Krolik & Kallman, 1987). In this energy range we can expect the corresponding absorption edges against the illuminating continuum spectrum. The Fe-atom is left in an unstable state and de-excites via one of two processes:

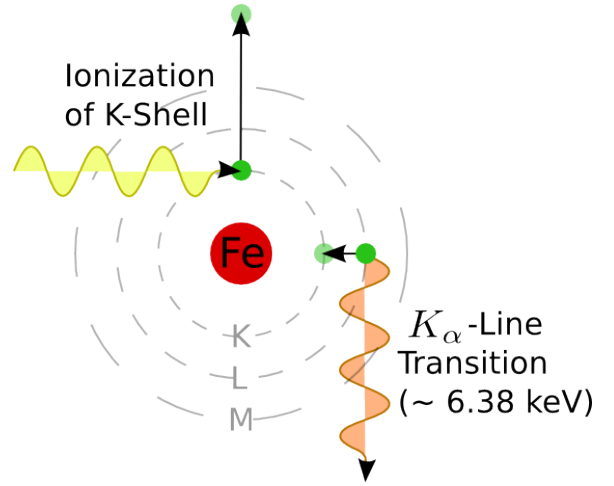


Figure 11: Schematic of an Fe ionization process followed by $K\alpha$ -emission.

Auger effect (auto-ionization): In intermediate shell electron drops into the K-state, and the binding energy is transferred to ionization of an outer shell electron. This transition is invisible in the spectrum as no photons are involved, and the branching ratio gets lower with increasing ionization state up to Fe XIV where the process gets impossible due to lack of electrons.

Line emission: An electron from a higher shell transitions to the K-shell emitting excess energy as X-ray photon as illustrated in Fig. 11. Depending on the origin of the electron, transitions are called $K\alpha$ (L-shell), $K\beta$ (M-shell) or $K\gamma$ (N-shell). The $K\alpha$ -transition is preferred by branching ratio in every ionization state and in the highest ionization states with unoccupied M and N-shells it is the only possible transition.

In a simplified model we can calculate the line energy from the binding energies of electrons in the Fe-core potential at the quantum energy levels n_x , utilizing an effective core charge $Z_{eff} = Z_{Fe} - s$ that takes account of repulsive forces from other shell electrons in the correction factor s .

$$E_{Kx} = Z_{eff} \left(\frac{1}{n_1^2} - \frac{1}{n_{2/3/4}^2} \right) \cdot 13.6 \text{ keV} \quad (30)$$

For a highly ionized atom, the correction term is negligible and we thus find line energies of $E_{K\alpha} = 6.9 \text{ keV}$ and $E_{K\beta} = 8.2 \text{ keV}$ while for a neutral atom, it is close to unity and we find $E_{K\alpha} = 6.4 \text{ keV}$ and $E_{K\beta} = 7.5 \text{ keV}$. Note however that this approximation is a very rough one, and that to get close to the measured values we would need to consider a full quantum mechanical treatment of asymmetric electron wave functions and spin-orbit-interaction (Mayer-Kuckuck, 1985).

According to Reynolds & Nowak (2003), the behaviour of the iron features depending on the ionization of the illuminated material $\log \xi$ can be classified into the following regimes (compare also Fig. 10):

Near-neutral - $\log \xi < 2$: There is a cold Iron line at 6.4 keV, a weak K-shell edge and a very weak continuum.

Intermediately ionized - $\log \xi < 2.7$: We find iron predominantly in the states from Fe XVII to Fe XXIII where fluorescent emission as well as Auger-deexcitation is possible. Here resonant scattering of the $K\alpha$ -photons happens frequently, leading to a slightly suppressed Iron line.

Highly ionized - $\log \xi < 3.7$: Iron atoms are too strongly ionized to permit Auger-deexcitation, so the iron line gets stronger again. The scattered continuum gets stronger and therefore the iron K-edge becomes visible in the reflection spectrum.

Fully ionized - $\log \xi > 3.7$: In this regime, no more atomic line or edge features are visible, but the continuum reflection is strongest.

2.4.5 Relativistic Reflection

In Eq. 19 for the energy dissipation in an accretion disk we have seen, that the energy conversion scales with R^{-3} . The largest part of the radiated emission of an accretion disk must therefore come from the central parts of the disk where a lot of gravitational energy has gone into the infalling material, and where gravitational fields and relative velocities are large.

Close to the event horizon this radiation is subject to strong relativistic effects in a curved space-time. Namely these are light bending and time dilation causing strong redshifts (Dauser, 2010). These effects modify the shape of the whole spectrum emitted from the innermost gravitational radii. They were first observed by Fabian et al. (1989) in their imprint on the broadened, asymmetric Fe $K\alpha$ line of the stellar mass black hole Cygnus X-1. For AGN relativistic effects were first observed in MCG-6-30-15 by Tanaka et al. (1995), who constrained the fluorescent emission to originate from material moving at $\sim 0.3c$ at only several Schwarzschild radii.

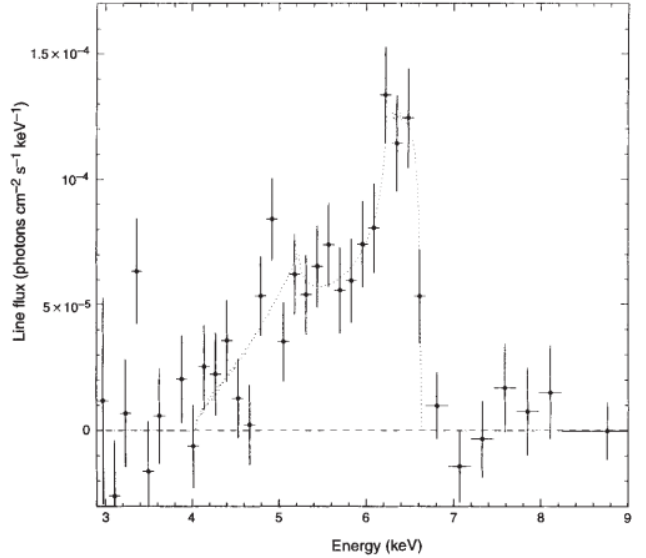


Figure 12: Broadened Iron line in the spectrum of MCG-6-30-15.

Image Credit: Tanaka et al. (1995)

Multiple sample studies (Nandra et al., 1997; Brenneman, 2013; Walton et al., 2013; Reynolds, 2014) established that broadened iron lines are a feature that can be found in many AGN spectra. Laor (1991) found that the line profiles that would be produced by a Schwarzschild and a Kerr black hole can be significantly distinguished as the reflection profile breaks off at the inner edge of the accretion disk. Bromley et al. (1997); Wilms et al. (2001) argued that MCG-6-30-15 must be home to a rotating black hole. For an in-depth discussion of the influence of the black hole spin parameter on the line profile, see the works of Dauser et al. (2010). We just point out that the radius of marginal stability and therefore the inner edge of the accretion disk strongly depends on the black hole spin after Fig. 6. The position of this cutoff significantly influences the reflection image and spectrum. Using elaborate numerical models of reflection off a cut-off disk in a relativistic space-time, we can study the influence of disk inclination, ionisation or the radial emissivity profile. In ray-tracing models of the disk we see the black hole to function as gravitational lens focusing the radiation of the disk behind itself (see Fig. 13).

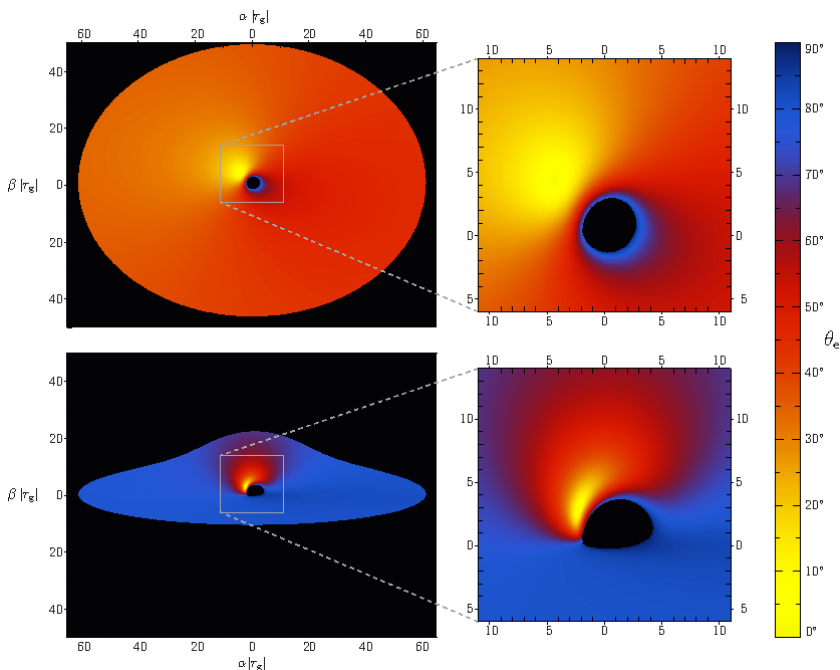


Figure 13: Reflection emission of two different accretion disks at 80° (top) and 30° (bottom) from the GR ray tracing model RELXILL. Colour coded is the emission angle at which radiation left the disk.

In non-relativistic regions, the emission angle is identical to the disk inclination, while close to the black hole we see that rays are emitted nearly vertical and bent towards the observer.

Image from García et al. (2014).

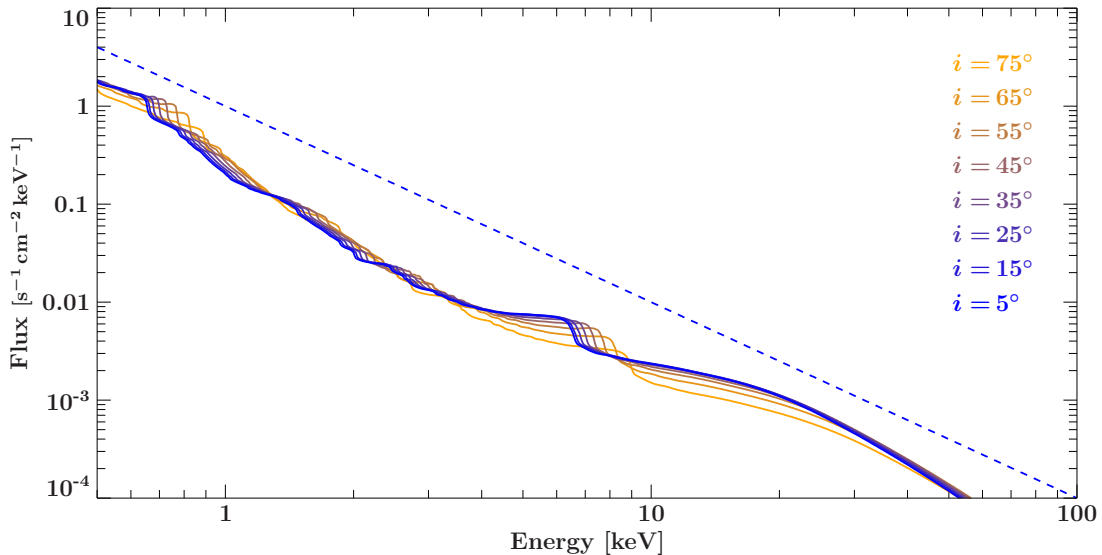


Figure 14: Relativistic reflection spectra at fixed $\log \xi = 2.7$ and $\Gamma = 2$. Disk inclinations range from 5° (blue) to 75° (orange). Calculated using RELXILLP.

Where for a top on view the image and spectrum remain largely unchanged, in a near edge view a large part of the reflection radiation closely passes by the black hole undergoing a significant change in direction, the angle of deflection being approximately (Refsdal, 1964):

$$\Delta\theta = \frac{4GM}{rc^2} \quad (31)$$

This deflection itself is independent of photon energy. But it leads to different viewing angles on the disk surface when following different sight lines. Close to the black hole we thus see different reflection spectra at each observed point on the disk. The combined effect of this gravitational lensing on the overall spectrum results in another dependency of the Fe-line and edge position on the viewing angle of the disk and is illustrated in Fig. 14.

Comparing with non-relativistic reflection spectra of Fig. 10 at similar ionization, we see that the relativistic reflection spectrum largely resembles the non-relativistic one, but with all sharp line features blurred into a distorted continuum.

2.5 Source Geometry

One largely unresolved question in AGN research is the exact origin and nature of the primary X-ray source. From the power law spectral shape, it is generally inferred that the driving process is one of the following: Either a hot, optically thin electron gas is illuminated by i.e. the thermal accretion disk spectrum. After Sec. 2.4.2 this spectrum is upscattered to resemble the observed power law spectrum. In the other case, a population of relativistic electrons is moving in a strong magnetic field emitting synchrotron radiation. In both cases we need a mechanism to accelerate electrons to relativistic speeds. Regions where this is feasible are around the inner part of the accretion flow or at the base of the commonly observed radio jets (Miller et al., 2015), see Fig. 15. Latest studies of reflection profiles have shown that these source regions must be compact and close to the center of the accretion disk (Keck et al., 2015; Svoboda et al., 2012), mostly resembling the lamppost case. Also from the strength of reflection features, a compact source can be inferred (Dauser, 2014; Fabian et al., 2015). Generally the following two mechanisms are discussed concerning the production of high energetic electrons.

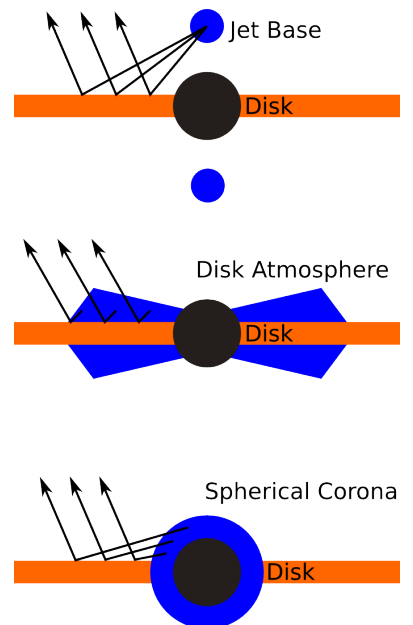


Figure 15: Different scenarios for X-ray emitting regions in the AGN.

Magnetic Fields: We expect the inner accretion flow to be differential and highly ionized, thus electrically conductive and able to produce magnetic fields. A turbulent and differential flow could create magnetic field loops that are rapidly changing size or even crossing other loops, violently reconnecting. After all, from Maxwell's equations we know that for negligible $\frac{\partial \vec{E}}{\partial t}$:

$$\vec{j} = \frac{c}{4\pi} \nabla \times \vec{B} \quad (32)$$

So that when we have rapidly changing magnetic fields, large currents are induced in the plasma that will result in higher velocities for the lighter electrons. There are different theoretical models handling this, see for example the review of Ulmschneider et al. (1991)

Shock acceleration: A process that is mainly studied in the context of supernovae, however in the central accretion disk in gas masses moving extremely supersonic or even at significant fractions of c we have perfect conditions for creating shockwaves between flows of high relative velocity.

According to the Fermi mechanism, Particles crossing such a shockwave will see material moving towards them, experiencing acceleration upon reflection. A particle reflected backwards across the shock front will again be moving against the stream and will end in a cycle of accelerating reflections across the shock front. This mechanism works for any particle type and scattering processes that do not cost too much energy. For an in depth explanation see Blandford & Eichler (1987).

The question for the process driving this heating is deeply connected to the location in the AGN. Where in accretion disks magnetohydrodynamical processes are expected for a variety of reasons, the observed relativistic jets allow perfect conditions for collisionless shocks.

The reflection spectrum shines light on this question as it allows us to infer information on the shape of the primary source irradiating the accretion disk. The emissivity profile $\epsilon(r)$ of light reflected off the accretion disk can be calculated for a given source geometry. For a treatment of a layer above and below the accretion disk see Haardt & Maraschi (1991), while the case of a spherical corona surrounding the event horizon has been discussed for the stellar mass BH Cygnus X-1 by Dove et al. (1998). In this work, we will focus on the setup of a compact source above the accretion disk as illustrated at the top of Fig. 15 and test whether it is compatible with observations. This setup was first considered theoretically by George et al. (1989) and by Matt et al. (1992). The radial emissivity profile can be approximated by $\epsilon \propto r^{-3}$ in Newtonian spacetime. However, due to light bending and spacetime curvature, the profile deviates in the innermost $10 r_g$ (Wilkins & Fabian, 2012). This is commonly approximated via a broken power law profile, compare Fig. 16. For smaller source heights, the breaking radius gets smaller as the inner index increases. For a detailed discussion of emissivity profiles, see Dauser et al. (2013).

The combined effect of a given point source emissivity profile on the total spectrum is given in Fig. 16. Most notably, the strength of the reflected continuum versus the incident continuum rises with the source closer to the disk. Also, the feature of the broad iron line gets more distinct for low sources.

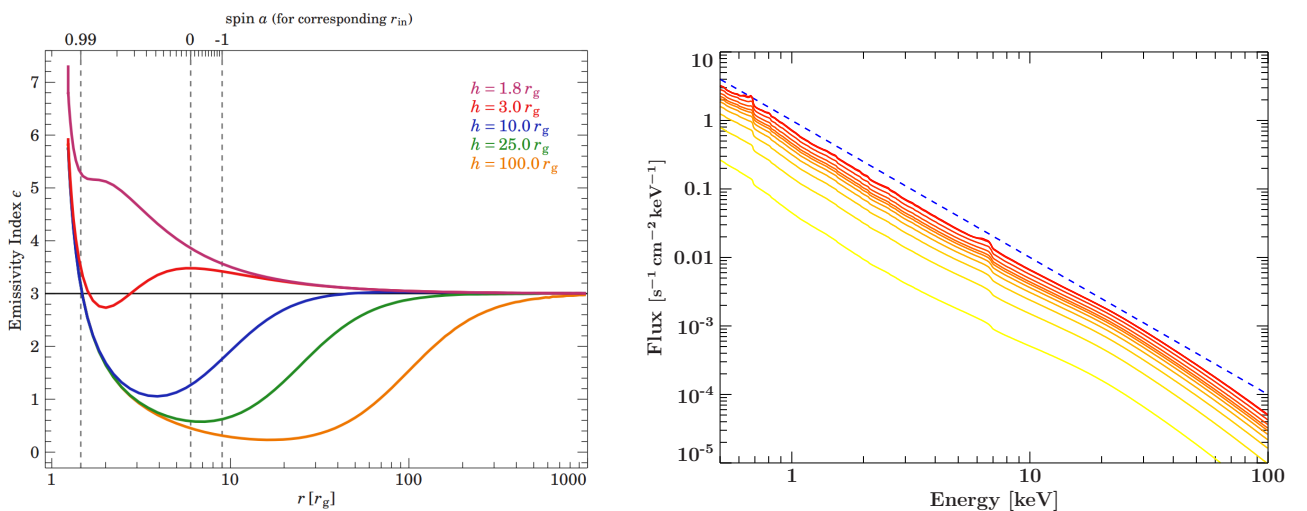


Figure 16: Left: Emissivity profiles of point source reflection from an accretion disk, calculated for different source heights. Image: Dauser (2014)

Right: Relativistic reflection spectra at fixed $\log \xi = 2.7$ and $\Gamma = 2$. Lamppost heights range from $2 r_g$ (yellow) to $60 r_g$ (red). Calculated using the self-consistent lamppost reflection spectrum model RELXILLP.

3 Instruments

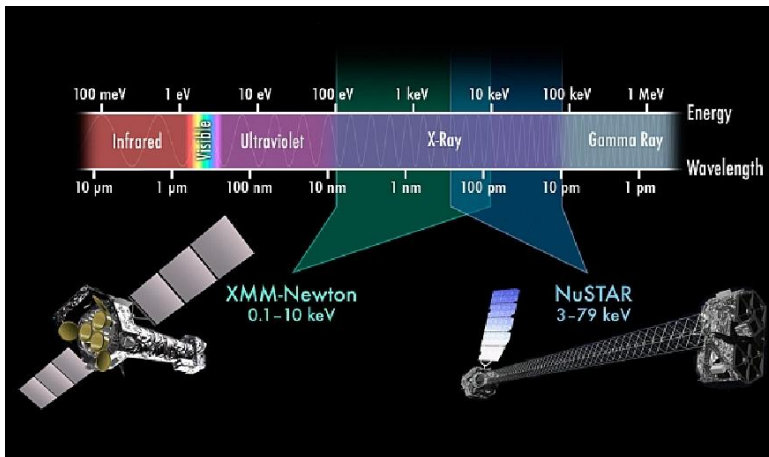


Figure 17: Artist’s depiction of the *XMM-Newton* and *NuSTAR* observatories and their spectral ranges in the electromagnetic spectrum. Image credit: NASA/JPL, Caltech

In the preceding sections we have seen that the characterising spectral features of accretion disk reflection span a spectral range of over 2 decades. While there is no single instrument with this capability, the 0.1 to 10 keV range is well observable by a multitude of X-ray observatories like *XMM-Newton*, *Chandra* or *Suzaku*. Using the more recently started *NuSTAR* satellite, this range can be expanded up to 79 keV. For this work, we use data of *XMM-Newton*, the X-ray Multi-Mirror Mission which over a operating time of over 16 years collected a huge archive of well calibrated and high resolution AGN spectra. Complementary we use latest data taken by the *NuSTAR* (*Nuclear Spectroscopic Telescope Array*) mission unprecedented in resolution in its hard X-ray spectral range.

3.1 Wolter telescopes

The interaction of X-rays with matter differ vastly from the behaviour of visible photons in classical optics. In an optical mirror telescope, photons hit a parabolic mirror at high angles of incidence. X-rays would penetrate or get absorbed in all known materials under such a geometry. Significant total reflection of X-rays only occurs below a critical angle of incidence θ_C (Parratt, 1954). The critical angle is given by:

$$\theta_C = 5.6' \sqrt{\frac{\rho}{1 \text{ g cm}^{-3}}} \cdot \frac{\lambda}{1 \text{ nm}} \quad (33)$$

Even for high density materials and soft X-ray wavelengths, this critical angle only reaches up to 1° (Kraus, 2016). This reflection behaviour motivated the invention of grazing incidence optics by Wolter (1952). Instead of reflecting at high angles from the cusp of a parabola, the Wolter telescope uses the high slope section of a parabolic mirror to direct rays toward the focal point, which in this case lies behind the mirror optics. In the frequently implemented Wolter type I case, the focal length is further reduced by adding a second hyperboloid mirror after the parabolic section as shown in Fig. 18.

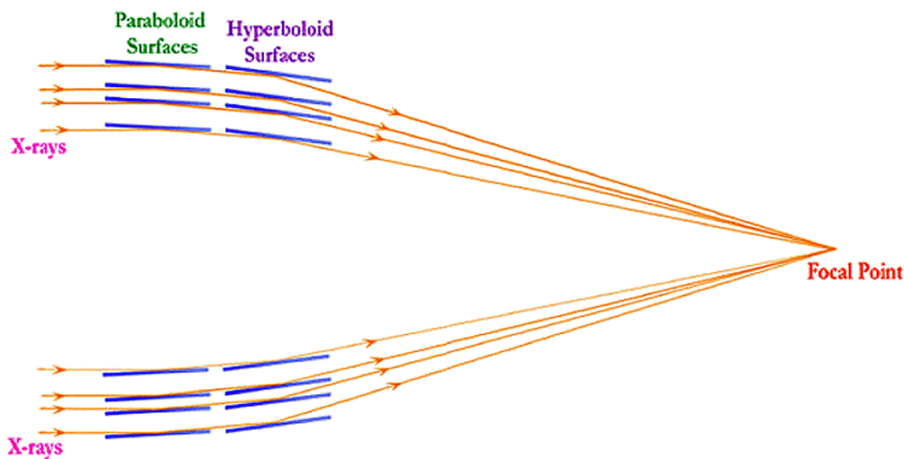


Figure 18: Principle of the Wolter telescope with paraboloid and hyperboloid sections. Image: Gorenstein (2012)

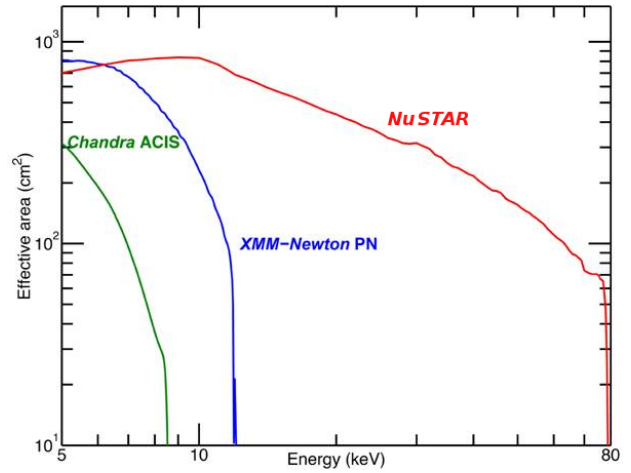


Figure 19: Left: *NuSTAR* Wolter I optics with detail view of the nested mirrors. Image: Nasa/JPL, Caltech
 Right: Effective mirror areas of *XMM-Newton*, *Chandra* and *NuSTAR*. (An et al., 2014)

A single grazing incidence mirror only provides a very small surface in the direction of the optical axis. It is common practice to nest multiple layers of mirrors for a much larger effective mirror area. For manufacturing reasons these mirrors are approximated to conical shape. In most Wolter optics the dependencies between reflection angle and reflectivity lead to a measurable drop in sensitivity away from the optical axis. This effect is called vignetting. In the case of *NuSTAR* effective area drops by a factor of 10 from the optical axis to the edge of the field of view (Harrison et al., 2013).

The wavelength dependence of the critical angle in Eq. 33 is the limiting factor in the energy range of X-ray observatories towards high energies. However, using multilayered mirror materials of like the Pt/SiC and W/Si mirrors of *NuSTAR* reflectivity in hard X-rays can be increased vastly, compare in Fig. 19.

3.2 XMM-Newton

The ESA X-ray observatory *XMM-Newton* was launched into a 40° inclination elliptical orbit on an Ariane 5 from the European spaceport of Korou in French Guiana. The high orbit inclination and eccentricity allow continuous unblocked observation of targets on the whole sky, but at the expense of radiation shielding from earth's magnetic field making careful screening of the detector background necessary. The spacecraft is built around three Wolter Type I grazing-incidence telescopes of 70 cm aperture and 58 mirrors each as illustrated in Fig. 23. These telescopes feed into a range of instruments:

Launch	12/1999	
Peri-/Apogee	5660 km	113000 km
Mass/Focal length	3800 kg	7.5 m
Orbital period	48 hrs	
Energy Range	0.15-12 keV	
Spectral Resolution (pn)	150 eV	
Spatial Resolution (pn)	5'' (FWHM)	
Time resolution (burst mode)	7 μ s	

Figure 20: Specifications of the *XMM-Newton* observatory (Jansen et al., 2001).

European Photon Imaging Camera (EPIC): *XMM-Newton* carries three cameras, one at each mirror module focus. Two are of the the MOS-CCD type, one is a higher resolution pn-CCD which can be operated in several windowed modes and a high time resolution readout mode. For an example readout of the central high resolution window of the EPICpnused for spectroscopy see Fig. 21. The rays surrounding the point source are the imprint of the mirror holding structures on the point spread function. A detailed description of the detector can be found in Strüder et al. (2001).

Reflection Grating Spectrometer (RGS): Two of the mirrors carry integrated grating structures reflecting the scattering image of first order onto a secondary CCD for high resolution spectroscopy in the 0.3 to 2.1 keV range at an energy resolution of up to 500 (den Herder et al., 2001).

Optical Monitor (OM): A 30 cm UV and optical telescope to provide simultaneous optical imaging data to X-ray observations. Its resolution of 1'' is comparable to that of a 4 m ground-based telescope (Mason et al., 2001).

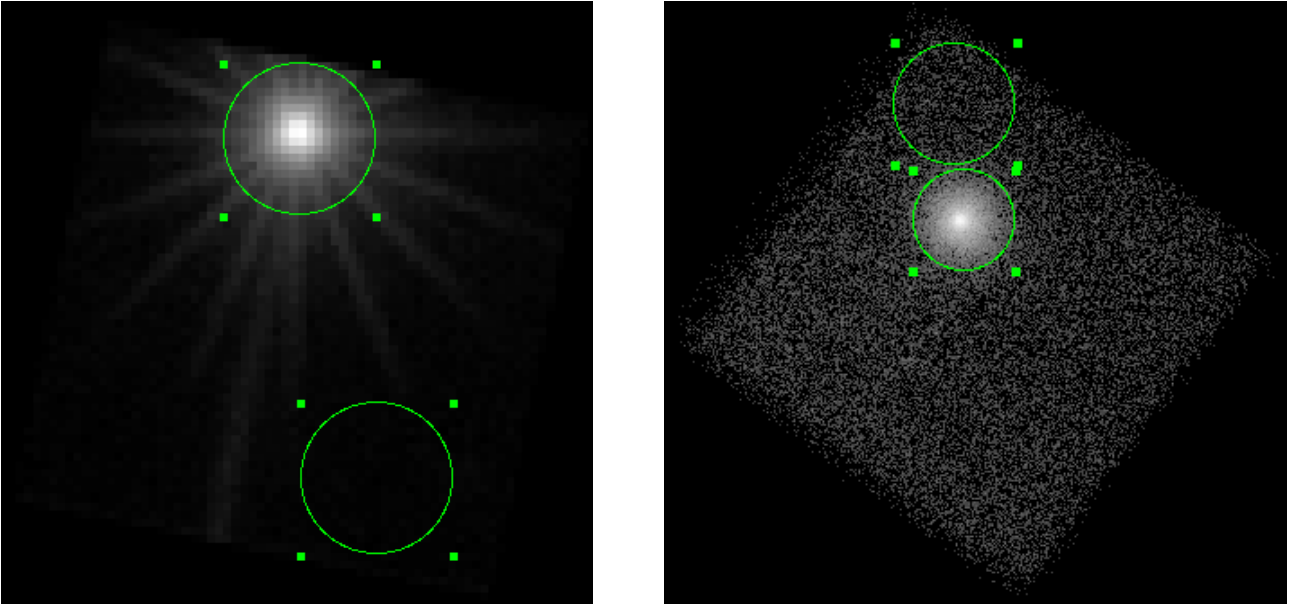


Figure 21: Left: EPICpn medium filter image of Ark 120. Rays around the point source are caused by the mirror holding structures. Right: *NuSTAR* FPMA image of Ark 120 with extraction regions for source and background, compare Sec. 5.2.

3.3 NuSTAR

NuSTAR was built by NASA and launched to a near equatorial orbit on a plane-launched Pegasus XL rocket. Its optics module consists of two Wolter-I telescopes of 138 mirror shells each. The detector modules sit at the end of a 10 m unfolding mast and were extended into the focal plane once the satellite was in orbit (compare schematic in Fig. 24). A metrology system of IR lasers is used to determine the position of the two modules with respect to each other in order to correct for flexing of the mast that would otherwise become visible in the data. The low earth orbit implies frequent earth occultations of most targets, thus a given observing window yields 55% to 90% of actual target exposure time, depending on the target latitude.

Launch	06/2012	
Peri-/Apogee	610 km	650 km
Mass/Focal Length	350 kg	11 m
Orbital period	1.6 hrs	
Energy Range	3-79 keV	
Spectral Resolution (pn)	400-900 eV	
Spatial Resolution (pn)	18'' (FWHM)	
Time resolution (burst mode)	100 μ s	

Figure 22: Specifications of the *NuSTAR* observatory (Harrison et al., 2013).

Focal Plane Module A/B (FPM): The focal plane instrumentation consists of a set of CdZnTe CCD detectors at each optical axis. Each detector consists of four CCD chips of 32*32 pixels each. The detector arrays are slightly offset from the optical axis, so that the axis where resolution is highest and least image distortion occurs, does not run through the detector gaps, but can be observed effectively. Compare Fig. 21 where the optical axis is aligned with the point source.

The CCDs are embedded into an anti-coincidence shield CsI detector. When an event enters the CCD from a direction different from the optical axis, it is also detected in the coincidence shield and can be discarded as background event. Upon an event, an on-board processor identifies the pixel location and reads out a 3×3 -pixel array of pulse height information that is used to reconstruct the energy of the event (Kitaguchi et al., 2014). Concerning these event patterns see also Sec. 4.1.

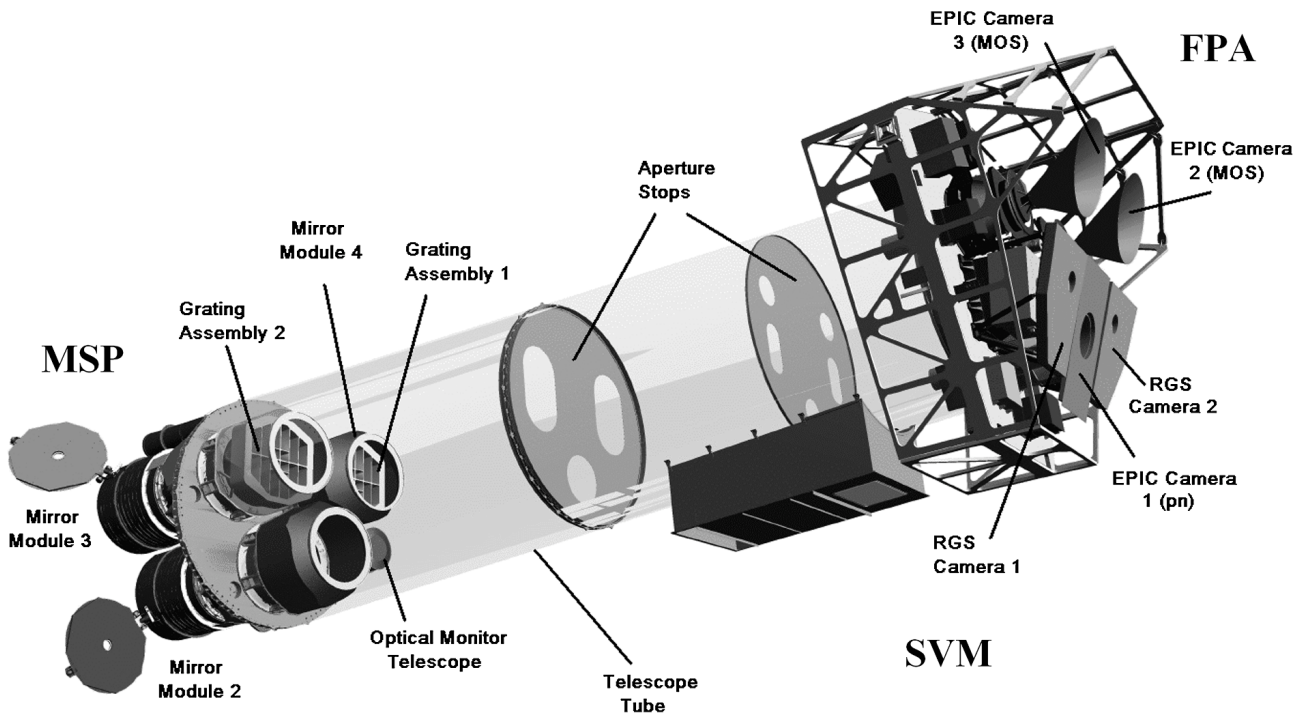


Figure 23: Schematic of the *XMM-Newton* X-ray observatory. Image: Lumb et al. (2012)

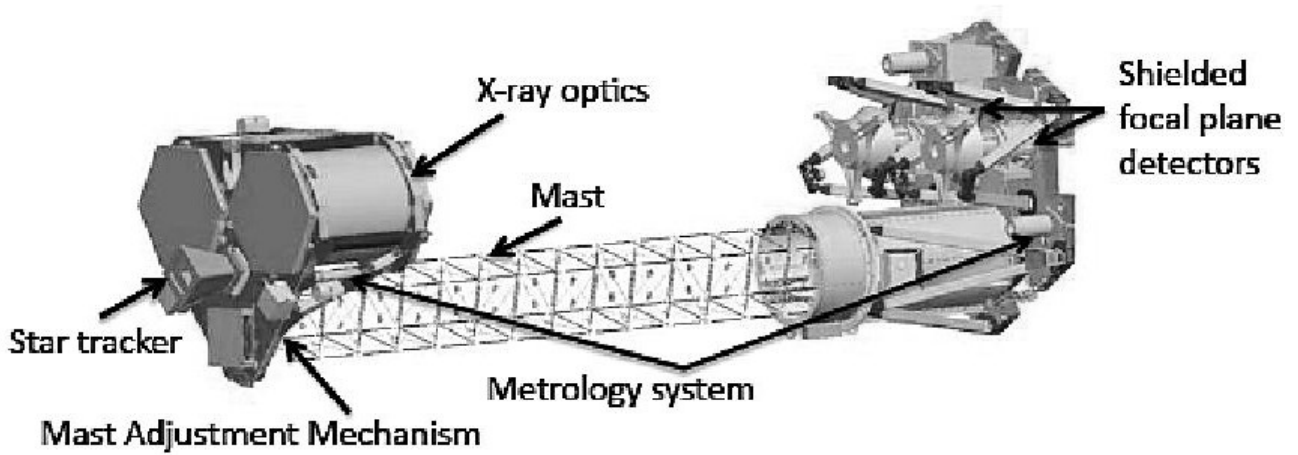


Figure 24: Schematic of the *NuSTAR* spacecraft. Image: *NuSTAR* Collaboration

4 X-ray Data Analysis

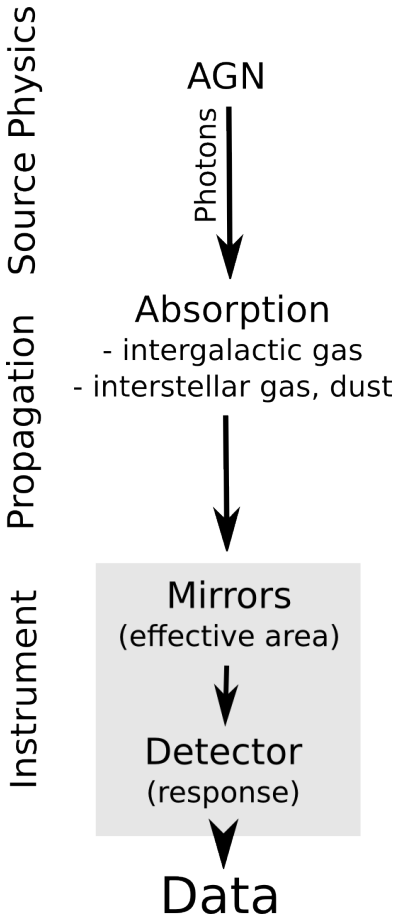


Figure 25: Schematic of data acquisition in X-ray astronomy.

For empirical data analysis, it is important to understand the whole process of taking data from the astrophysical source object to the detector producing the numerical experimental data. In X-ray astronomical observations, we begin at the source that is described by a complex physical model, in our case the AGN model outlined in the preceding chapters. This source produces a flux of X-ray photons travelling through the intergalactic and interstellar medium and interacting with intervening material. When observing Seyfert galaxies, this absorption only has a significant impact in the interstellar dust and hydrogen medium of our galaxy. After Wilms et al. (2000), interstellar absorption can be written as:

$$F_{\text{abs}}(E) = F_{\text{src}}(E) \cdot e^{-\sigma_{\text{ISM}}(E)N_{\text{H}}} \quad (34)$$

Here $\sigma_{\text{ISM}} = \sigma_{\text{gas}} + \sigma_{\text{molecules}} + \sigma_{\text{grains}}$ collects the cross sections of the different phases of the interstellar medium and is normalized to the number density of hydrogen N_{H} . Everything up to now goes into the astrophysical model predicting the energy-dependent Flux $F(E)$ entering the telescope.

Here we need to take into account two more components, the mirror and the detector. As the reflectivity of X-ray optics depends on the incident photon energy, this is taken into account by scaling the photon flux by an energy dependent effective area $A(E)$, see Fig. 19. This function is generally provided in a discrete matrix form via the *ancillary response file* (ARF).

When hitting the detector the photon is assigned to a discretely numbered energy channel of width ΔE . However, this assignment is not unambiguous. Photons may trigger signals in channels of different energy. This is handled through the detector response function $R(c, E)$ which gives the probability that a photon at energy E triggers a given channel c . This response function is published in form of a *redistribution matrix file* (RMF). Folding the predicted incoming Flux with these two response functions for each channel, we get the final measured source spectrum discretized into channels c (Lampton et al., 1976):

$$S_{\text{ph}}(c) = \sum_{i=0}^{n_{\text{channels}}} R(c, i)A(E_i)F(E_i)\Delta E \quad (35)$$

The measured output spectrum $N_{\text{ph}}(c)$ of the detector contains a component of background flux, so that $N_{\text{ph}}(c) = S_{\text{ph}}(c) + B_{\text{ph}}(c)$. This background has two main causes:

- Astrophysical sources along the line of sight that can not be distinguished as individual sources. In the X-ray spectral band this background might be dominated by the early population of individually not detectable AGN in the high redshift universe (Comastri et al., 1995).
- Erratic detections of photon events that did not originate in the source direction, but rather from unfiltered cosmic rays passing the detector, undetected hot pixels or artifacts produced by the CCD readout electronics (Lumb et al., 2002).

Both backgrounds can be estimated together by measuring the flux of a source-less area in the exposure next to the target source. We get the estimated source flux by subtracting this background from the measured total Flux:

$$\hat{S}_{\text{ph}}(c) = N_{\text{ph}}(c) - \hat{B}_{\text{ph}}(c) \quad (36)$$

4.1 CCD event patterns

Simplistically we can assume to get as analysable data the time, location and energy of a photon hitting a CCD within some margin of error. But we have to keep in mind the grid nature of a CCD and its interaction with an impacting photon. Typically, a photon hitting the CCD material produces a cloud of separated charges in the semiconductor material that is detected if it surpasses a given threshold. From the size of the charge, the original Photon energy can be inferred. There is also the possibility of a photon hitting near the edge of a pixel and the charge cloud spreading across several pixels, surpassing the threshold in each one. These event patterns are illustrated in Fig. 26. This effect can be diminished by recognizing the according patterns and reconstructing the original Photon energy.

However, if the time between events in an area of the CCD gets close to the read-out time, there is a probability that these pattern events will be created by different photons arriving at the same time. Nevertheless, these patterns will be recognised as single photon events. For the *XMM-Newton* EPICpnused in the small window mode, which is the case in most of the observations analysed later on, the critical count rate is 25 cts s^{-1} (XMM, 2016).

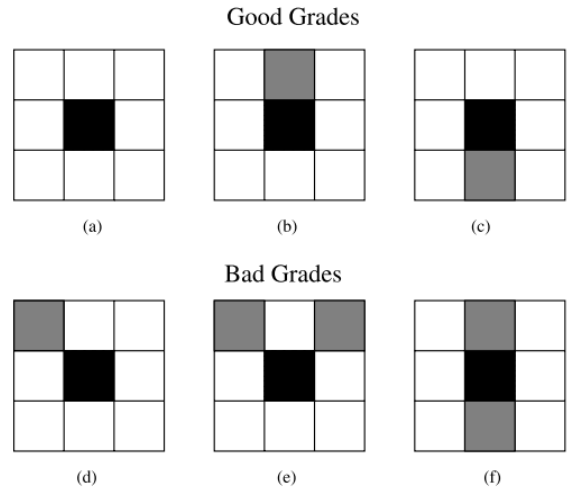


Figure 26: Some possible event patterns in a 3×3 CCD grid. The top patterns are possible to be produced by a photon impacting a pixel edge, while the lower ones are more likely to be the results of a Pileup effect. Image: (Davis, 2001)

This effect, called pattern pileup, skews spectra towards higher energies by assigning several low energy photons to a single high energy bin. The unwanted detector effect can be identified via the procedure explained in Davis (2001). For a given spectrum, a prediction of pattern frequencies can be calculated under the assumption that no pileup happened. By comparing this model to the actual distribution, we can see if the spectrum is affected by pileup. An example of the effects of pileup on the pattern distribution is viewed in Fig. 27. Note that the model overpredicts in the low energy range, and underpredicts in the high energy range, so spectral flux effectively gets shifted to higher energies.

A simple countermeasure to pileup is to only extract regions of the CCD hit by lower flux. In the case of a point source we extract a ring around the maximum, thus only keeping the low flux of the outer wings of the point spread function.

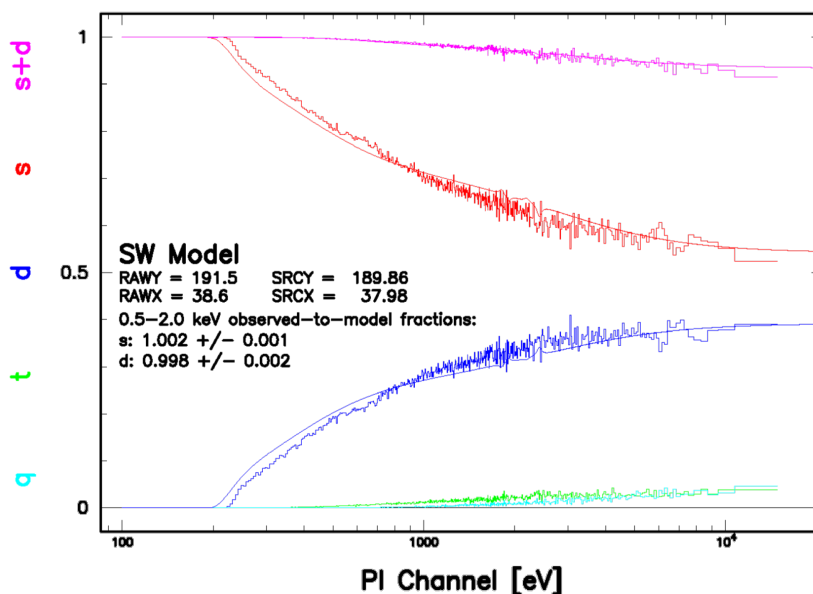


Figure 27: Energy-dependent pattern distribution of an *XMM-Newton* observation of Ark 564. The plot shows distributions derived from spectrum extraction (histogram) and modelled. Plotted using EPATPLOT.

4.2 χ^2 -Statistics

We see that in acquiring data from an astronomic source, a whole chain of physical models from source to detection is required. As these models are often very complex, inverting the detector and mirror matrices is generally not easily possible. Instead it is more straightforward to state a theoretical model of the source, apply all absorption, propagation and detector effects to this model and compare this prediction to the real data.

To quantify whether the prediction correctly describes the data we try to explain, the most commonly used measure is the χ^2 -Statistic introduced by Pearson (1900). We follow the description given by Lampton et al. (1976). Suppose we have a model predicting spectral flux M_{ph}^i for each spectral bin i , while \hat{S}_{ph}^i are the accordingly binned spectral data from Eq. 36. The photon counts per bin are subject to a Poissonian error distribution such that $\sigma^i = \sqrt{\hat{S}_{\text{ph}}^i}$. The deviation between spectral model and data is quantified using the test statistic

$$\chi^2 = \sum_0^{N_{\text{bins}}} \frac{(\hat{S}_{\text{ph}}^i - M_{\text{ph}}^i)^2}{\sigma^i} \quad (37)$$

The size of this value primarily depends on the deviation between model and data as illustrated in Fig. 28, but also receives a contribution from measurement errors. Assuming a model perfectly reproducing the data, these errors will still produce a non-zero test statistic.

Building on this argument, let the observation be repeatable and k be the number of statistical degrees of freedom. Then the probability of taking an observation and gaining a statistic of χ^2 will under the assumption of Gaussian errors follow a probability density $f(\chi^2, k)$ described by the χ^2 -distribution (see also Fig. 29):

$$f(\chi^2, k) = \frac{(\chi^2)^{(k/2-1)} e^{-\chi^2/2}}{2^{k/2} \Gamma(k/2)} \quad (38)$$

where $\Gamma(k/2) = \int_0^\infty t^{(k/2-1)} e^{-t} dt$ is the gamma function.

We accept a model, if its χ^2 is close enough to the expected χ^2 and otherwise reject it. Due to the measured χ^2 being subject to a random process, there is always a chance of having a perfectly working model, but rejecting it due to drawing a value from the high end of the χ^2 -distribution. We can handle this risk by choosing the according χ^2 threshold at which we reject our hypothesis. This risk α is found integrating the χ^2 probability distribution:

$$\alpha = \int_{\chi_{\text{thresh}}^2}^{\infty} f(\chi^2, k) d\chi^2 = F(\chi^2, k) \quad (39)$$

The value $1 - \alpha$ is called the confidence level and is typically set to values 68.3% (or 1- σ), 90% or 99%. The integrated probability distribution, or cumulative distribution function is shown in Fig. 29. It is given by:

$$F(\chi^2, k) = \frac{\gamma(k/2, \chi^2/2)}{\Gamma(k/2)} \quad (40)$$

where $\gamma(k/2, \chi^2/2)$ is the lower incomplete gamma function $\gamma(k/2, \chi^2/2) = \int_0^{\chi^2/2} t^{(k/2-1)} e^{-t} dt$.

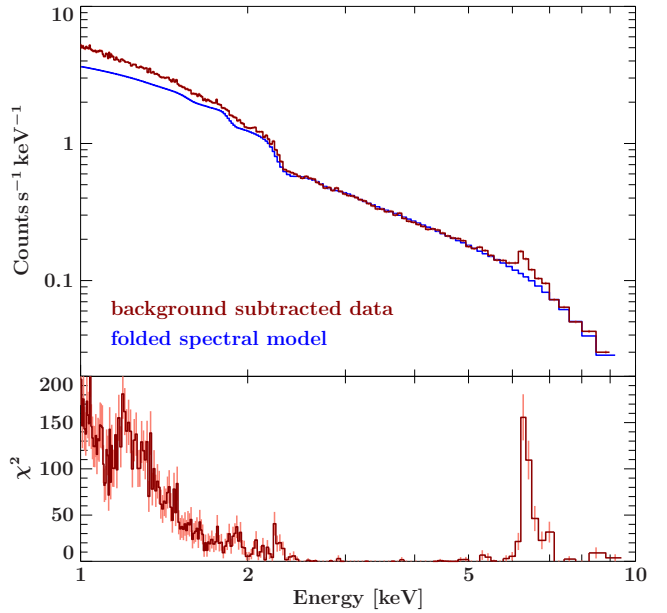


Figure 28: Binned and background subtracted spectral XMM-Newton data of Ark 120 together with a simple power law model folded through ARF, RMF and a galactic absorption model. χ^2 per bin on the lower panel.

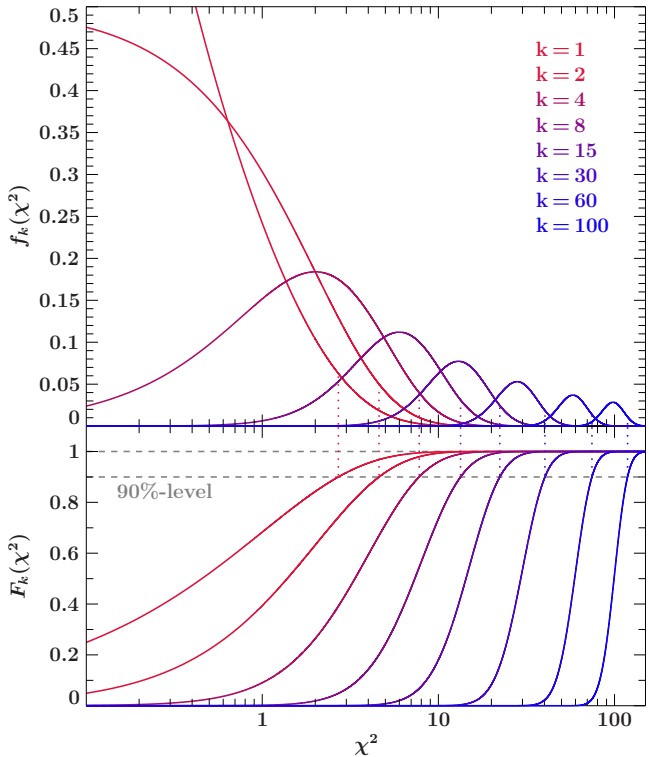


Figure 29: Probability density distribution (top) of χ^2 and its cumulative distribution function (bottom) at k degrees of freedom.

4.3 Parameter Estimation

If we have a model $S_{ph}(\bar{\mathbf{x}})$ that describes our spectrum depending on a set of physical parameters $\bar{\mathbf{x}}$, we can find a set of parameters most accurately describing reality by minimizing the function $\chi^2(\bar{\mathbf{x}})$. Throughout this work, this will be done using the damped least squares method by Levenberg (1944) and Marquardt (1963) as it is implemented in the ISIS spectral analysis site.

However, due to the data being subject to the error distributions discussed above, we have no chance of recovering the exact values of these parameters. The value x_{est} regained through χ^2 minimization will be fluctuating around the true value. Thus we can only constrain the interval containing the true value at a probability given by the confidence level:

$$x_{est} - \sigma < x_{true} < x_{est} + \sigma$$

The value minimizing the χ^2 -statistic will lie inside this interval, but bears no further physical meaning. In the case of a model with a single free parameter, determining this interval is straightforward. We calculate the statistic as a function of the model parameter $\chi^2(x)$. The limits of the confidence interval are reached where the difference in χ^2 surpasses the threshold determined by the cumulative distribution function for 1 degree of freedom.

Simultaneously estimating several parameters will increase these intervals for every single parameter as the model gains the freedom to compensate the worsening of χ^2 by moving other parameters. A prescription on how to calculate these multi-parameter confidence intervals can be found in Lampton et al. (1976) and Andrae (2010).

To get a quick grasp of how well a model represents the data, one can take a look at the reduced χ^2 .

$$\chi_{red}^2 = \frac{\chi^2}{N_{dof}} = \frac{1}{N_{dof}} \sum_0^{N_{bins}} \frac{(D_i - S_{ph}^i)^2}{\sigma^i} \quad (41)$$

In case of a perfect fit and well known error, for each bin the elements of the sum should lie around 1. The number of statistical degrees of freedom is $N_{dof} = N_{bins} - N_{parameters}$, so for a number of bins much larger than the number of model parameters, χ_{red}^2 should also lie close to 1.

If $\chi_{red}^2 \gg 1$, the deviations are receiving a contribution from the ill-fitting model. If a model has too many free parameters, it is capable of fitting noise fluctuations reducing χ_{red}^2 below 1. But we need to keep in mind that the reduced χ^2 depends on the bin size of the data and thus is no definitive measure for the acceptability of a model.

We also have to be aware that this formulation of the reduced χ^2 is only a rough approximation for complex non-linear models as pointed out by Andrae et al. (2010). Therefore it should never be the only criterion on which to reject or approve a hypothesis. More conclusive is an in-depth analysis of the multidimensional χ^2 -landscape and the behaviour of model-to-data residuals.

5 Extraction and model details

5.1 Sample Selection

The sample for this analysis are a subset of the sample of 25 bare AGN from Walton et al. (2013), selecting the visually most distinct iron lines. Additionally, we analyse NGC 1365 and MCG 6-30-15. All of these have been shown to feature significant relativistic reflection (Risaliti et al., 2013; Wilms et al., 2001). The Analysis of Walton used *Suzaku*/XIS data at a range of 0.5 to 10 keV. For some of the sources also PIN data above 20 keV are available, but at very low signal-to-noise. To constrain the relativistic reflection models, three energy ranges are of interest: 10-50 keV where the Compton reflection hump can be found, 5-8 keV for the sharp iron reflection line and the relativistically blurred iron line and the 0.5-2 keV range where especially cold distant reflection produces line emission and where absorption is imprinted on the spectrum. To disentangle distant and relativistic reflection reliably, all of these features need to be analysed.

There is no single instrument that spans this energy range, however joint *NuSTAR* and *XMM-Newton* observations cover the desired spectral range at high resolution. We limit our sample to those sources, for which we can acquire very high signal-to-noise spectra across a broad spectral range. We use archival data of *NuSTAR* and ESA *XMM-Newton* X-ray space observatories. Table 1 shows the sources in our sample. The first six sources of our sample were targets of a campaign of simultaneous long exposure *XMM-Newton* and *NuSTAR* observations. In the following tables, they are highlighted in bold face. For the remaining six sources, although no strictly simultaneous data are available, we still expect to be able acquire better constraints than from a single instrument observation.

We exclusively use spectroscopic data taken with the *XMM-Newton* EPICpn detector and *NuSTAR*'s focal plane modules. Compared to *Suzaku*'s PIN, the FPM detectors yield a much higher effective area, better photon statistics and wider energy range to gauge the Compton hump. Most importantly, the energy range overlap with EPICpn allows effective cross calibration of the detectors. Therefore, we expect to be able to significantly improve on the work done by Walton (2013).

Table 1: The sources and observational data chosen for this analysis. The last column references mostly work on *XMM-Newton*, *NuSTAR* or *Suzaku* data and on relativistic iron lines in the according sources.

Source	Instrument	Revolution/ Obsid	Start (Y-M-D h:m)	Exposure (ks)	References
Ark 120	FPM	60001044002	13-02-18 10:46	55.3	Matt et al. (2014); Garcia et al. (2014)
	EPICpn	2417/0693781501	13-02-18 11:39	130	Nardini et al. (2011); Vaughan et al. (2004)
Fairall 9	FPM	60001130003	14-05-09 23:01	93.8	Emmanoulopoulos et al. (2011)
	EPICpn	2640/0741330101	14-05-09 02:20	141	Schmoll et al. (2009); Lohfink et al. (2012)
NGC 1365	FPM	60002046005	12-12-24 14:31	66.3	Risaliti et al. (2005, 2013)
	EPICpn	2389/0692840301	12-12-24 15:34	126	Walton et al. (2014)
PDS 456	FPM	60002032010	14-02-26 08:16	101	Reeves et al. (2003, 2009, 2014)
	EPICpn	2640/0721010601	14-02-26 07:45	141	Gofford et al. (2014)
MCG-6-30-15	FPM	60001047003	13-01-30 00:11	127	Fabian et al. (2002); Wilms et al. (2001); Morales et al. (2000)
	EPICpn	2407/0693781201	13-01-29 12:08	134	Miller et al. (2008); Marinucci et al. (2014b); Vaughan et al. (2004)
Mrk 841	FPM	60101023002	15-07-14 17:36	23.4	Longinotti et al. (2010); Petrucci et al. (2007)
	EPICpn	2856/0763790501	15-07-14 18:01	29.5	
Mrk 335	FPM	60001041005	13-06-25 08:06	93.0	Parker et al. (2014); Gallo et al. (2013)
	EPICpn	1741/600540601	09-11-06 07:16	132	Wilkins et al. (2015)
3C 382	FPM	60001084002	13-12-18 01:51	82.5	Ballantyne et al. (2014)
	EPICpn	1536/0506120101	08-04-28 11:23	39.4	Torresi et al. (2010); Reeves et al. (2009)
3C 390.3	FPM	60001082003	14-05-24 19:51	47.5	Sambruna et al. (2009)
	EPICpn	0885/0203720201	04-08-10 19:43	70.4	
1H 0419-577	FPM	60101039002	15-06-07 03:18	169	Di Gesu et al. (2014); Fabian et al. (2005)
	EPICpn	1917/0604720301	10-05-30 07:01	107	Page et al. (2002); Pounds et al. (2001, 2004)
Mrk 509	FPM	60101043002	15-04-29 14:26	166	Mehdipour et al. (2011); Pal & Dewangan (2013)
	EPICpn	1806/0601390301	09-10-19 15:37	63.8	
Mrk 1018	FPM	60160087002	16-02-10 22:11	21.6	
	EPICpn	1586/0554920301	08-08-07 02:28	17.6	

5.2 Extraction

Data were acquired from the public archives via the *xmmaster* and *numaster* catalogues. Data Extractions were performed using the utilities of the HEADAS package 6.19, especially XMM-SAS version 14.0 for EPICpn and NuSTARDAS 1.6.0 for FPM extractions. Source spectra and light-curves are extracted using the extraction scripts *xmmextract* respectively *nuextract* of the Reemis-Observatory, utilizing the HEADAS-programs EVSELECT, ARFGEN and RMFGEN for spectrum, ancillary response and redistribution matrix production. General FITS-file operations were performed using FTOOLS and the fits viewer FV version 5.4. After extracting full images, spectrum extraction regions were selected in the image viewer DS9 version 7.2 (compare Fig 21 in Sec. 3.2). Extraction regions are circular, including as much of the source point spread function as possible without overlapping background sources or CCD gaps. Background regions are also chosen as large as possible without intersecting point sources or the diffraction patterns of the main source. All extraction regions are given in table 2. We extract single pixel events only, and extract light curves in bins of 100 s.

In the highest flux sources MCG–6-30-15 and Mrk 841 we find strong pileup effects in energy patterns (analyzed via EPATPLOT), which we diminish by extracting only an annulus around the bright source.

Table 2: Spectrum and light curve extraction parameters. Per default, circular regions are extracted across the full time range of an observation. Where two radii are given, these denote an annular extraction region. For some observations time windows are given relative to the start of the observation. They are substantiated in the following section.

Source	Detector	Source Dec, Ra, Radius (°, °, ")	Background Dec, Ra, Radius (°, °, ")	Time window (ks)
Ark 120	FPMA	79.04579, -0.151431, 100	79.05034, -0.087702, 120	-
	FPMB	79.04498, -0.151747, 100	79.04261, -0.087260, 120	-
	EPICpn	79.04792, -0.151274, 40	79.03598, -0.200453, 40	-
Fairall 9	FPMA	20.93758, -58.80509, 100	21.04056, -58.85831, 120	-
	FPMB	20.94008, -58.80425, 100	21.04786, -58.84461, 120	-
	EPICpn	20.93956, -58.80545, 40	20.86915, -58.76572, 40	-
NGC 1365	FPMA	53.40068, -36.14017, 100	53.36237, -36.08842, 120	57.5 - 87.0
	FPMB	53.40125, -36.14159, 100	53.35487, -36.09337, 120	57.5 - 87.0
	EPICpn	53.40266, -36.14169, 40	53.44165, -36.19649, 60	57.5 - 87.0
PDS 456	FPMA	262.0821, -14.26597, 50	262.0533, -14.31386, 120	62.4 - 89.3
	FPMB	262.0835, -14.26746, 50	262.0476, -14.30417, 120	62.4 - 89.3
	EPICpn	262.0817, -14.26490, 40	262.1008, -14.21101, 60	62.4 - 89.3
MCG–6-30-15	FPMA	203.9731, -34.29598, 80	203.9152, -34.33978, 120	43.2 - 69.0
	FPMB	203.9738, -34.29863, 80	203.9250, -34.34556, 120	43.2 - 69.0
	EPICpn	203.9747, -34.29556, 7.5-40	204.0232, -34.26861, 50	85.0 - 111
Mrk 841	FPMA	226.0027, 10.43933, 70	226.0450, 10.48098, 120	-
	FPMB	226.0013, 10.44001, 70	226.0418, 10.48553, 120	-
	EPICpn	226.0051, 10.43608, 15-40	225.9603, 10.39821, 50	-
Mrk 335	FPMA	1.581930, 20.20178, 80	1.588976, 20.14248, 120	-
	FPMB	1.583092, 20.20340, 80	1.596708, 20.14622, 120	-
	EPICpn	1.580558, 20.20310, 40	1.584643, 20.25605, 60	0 - 82
3C 382	FPMA	278.7653, 32.69595, 80	278.7072, 32.74146, 120	-
	FPMB	278.7642, 32.69416, 80	278.6993, 32.72771, 120	-
	EPICpn	278.7610, 32.69965, 40	278.7581, 32.74634, 60	-
3C 390.3	FPMA	280.5279, 79.77179, 80	280.7248, 79.72241, 120	-
	FPMB	280.5351, 79.77211, 80	280.7872, 79.72820, 120	-
	EPICpn	280.5364, 79.77021, 40	280.4276, 79.72675, 60	-
1H 0419–577	FPMA	66.50185, -57.19956, 80	66.61656, -57.23093, 120	-
	FPMB	66.50264, -57.19822, 80	66.61529, -57.21411, 120	-
	EPICpn	66.50187, -57.20075, 40	66.42806, -57.18011, 60	50.0 - 82.0
Mrk 509	FPMA	311.0406, -10.72494, 80	311.0411, -10.77960, 120	-
	FPMB	311.0421, -10.72395, 80	311.0485, -10.78996, 120	-
	EPICpn	311.0408, -10.72399, 40	311.0708, -10.75743, 50	-
Mrk 1018	FPMA	31.56694, -0.292536, 40	31.56808, -0.364230, 120	-
	FPMB	31.56571, -0.291903, 40	31.55006, -0.352123, 120	-
	EPICpn	31.56581, -0.290514, 40	31.57564, -0.243444, 50	-

5.3 Light Curves

To measure the subtle features of relativistic spectral distortion, we need to make sure that the source is in a stable state, to prevent averaging over spectral variability from outbursts or absorption coverage. Light-curves are presented in Fig. 30 for the simultaneous observations and in Fig. 32 for non-simultaneous ones. *NuSTAR* lightcurves are not continuous due to frequent earth occultations and the gaps follow the orbital period of 96.8 minutes. FPM light-curves generally show less counts due to observing the harder, low-flux part of the power law spectrum. *XMM-Newton*'s highly eccentric orbit allows continuous exposures but sacrifices radiation shielding of the earth magnetic field. During increased radiation CCD-readout is interrupted, also leading to data loss.

5.3.1 Simultaneous Observations

The simultaneous *XMM-Newton* and *NuSTAR* exposures of Ark 120, Fairall 9 and Mrk 841 show very steady light-curves with variability below 10%. Although the *XMM-Newton* and *NuSTAR* time ranges do not completely coincide, the light-curves suggest that the source is in a long term stable state, so we extract the complete time ranges of these observations for spectral analysis to improve statistics.

For PDS 456 we find stronger variability and also EPICpn background flaring. Therefore we exclude intervals of strong background and apply the bayesian block implementation of the Remeis-ISISSCRIPTS on the light-curve to select a 27 ks-interval of near constant flux and low background. A description of the algorithm is found in Scargle et al. (2013). NGC 1365 shows even stronger variability. As was established by Risaliti et al. (2005), this variability can be attributed to strong absorption close to the source at varying coverage. The ratio of EPICpn to FPM count rate is very low compared to other sources. This is also a consequence of absorption which suppresses the spectrum in the low energy range only seen by *XMM-Newton*. For spectral analysis, we identify a block of 29.5 ks duration.

The same procedure is applied to the dataset of MCG-6-30-15. In the PDS 456, NGC 1365 and MCG-6-30-15 lightcurves EPICpn and FPM count rates can be seen to correlate, indicating that also the *NuSTAR* energy range is slightly impacted by source flaring.

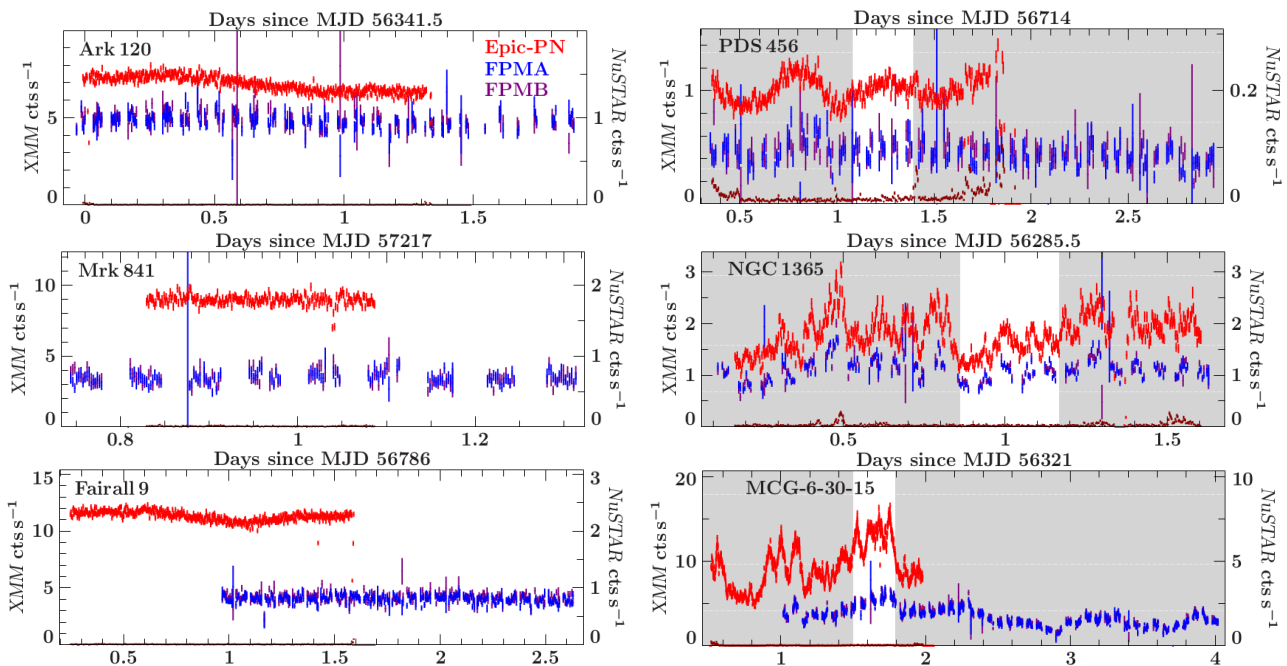


Figure 30: X-ray light-curves taken with the *XMM-Newton* EPICpn (red), PN background (dark red) and *NuSTAR* FPMA (blue) and FPMB (purple). *NuSTAR* light-curves are scaled up with respect to *XMM-Newton* light-curves. Right panels: grayed out regions are excluded from spectrum extractions.

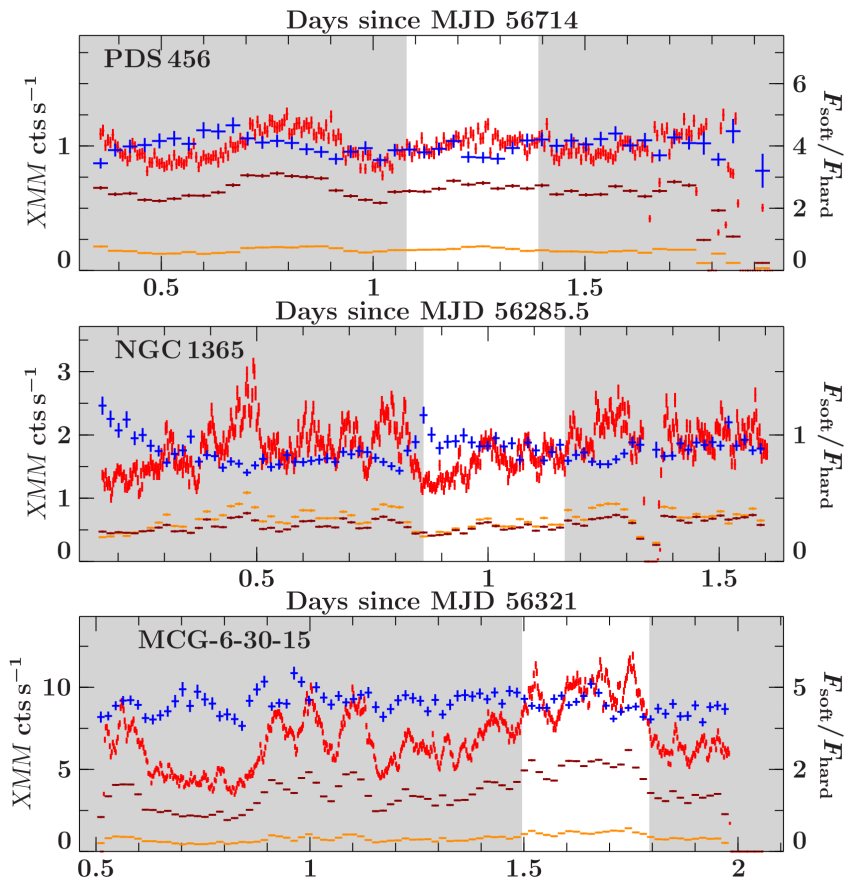


Figure 31: Hardness ratios of light-curves showing strong variability. Total EPICpn count rate in red. Hardness ratios (blue) are calculated from 0.5-2 keV (dark-red) and 2-5 keV (orange) light-curves.

5.3.2 Hardness ratio

In the light-curves of PDS 456, NGC 1365 and MCG-6-30-15 we found significant short term variability. To estimate the impact on the spectral features we want to analyze, we calculate the ratio of flux in a low energy spectral band to that in a higher energy band. This way, we can quantify the change of spectral slope due to flaring and variable coverage. Requiring high resolution in the soft and intermediate ranges, we use the *XMM-Newton* datasets for this consideration. For the soft band we choose the 0.5-2 keV range, the hard band ranges from 2-5 keV. Hardness ratios are displayed in Fig. 31. Generally we see a slight correlation between dips in the total count rate being accompanied by peaks in hardness ratio.

The hardness ratios of all sources are fluctuating within 20% around the average with no visible long term trend. We observe no strong peaks in our observation windows. To estimate the impact of this fluctuation on the observed continuum slopes, we calculate the hardness ratio of a simple power law as given in Eq 29, integrating over the two flux bands.

$$\frac{F_{\text{Soft}}}{F_{\text{Hard}}} = \frac{\int_{0.5 \text{ keV}}^{2 \text{ keV}} I_0 \epsilon^{-\Gamma} d\epsilon}{\int_{2 \text{ keV}}^{5 \text{ keV}} I_0 \epsilon^{-\Gamma} d\epsilon} = \frac{[\epsilon^{-\Gamma+1}]_{0.5 \text{ keV}}^{2 \text{ keV}}}{[\epsilon^{-\Gamma+1}]_{2 \text{ keV}}^{5 \text{ keV}}} \quad (42)$$

Assuming a typical photon index of $\Gamma = 2$, this equation yields a hardness ratio of 5, well agreeing with the observed values. With a standard deviation of 10% as observed in these hardness ratio curves, we can infer from the inverted relation that the spectral slope would fluctuate around $\Gamma = 2.0 \pm 0.1$.

5.3.3 Non-simultaneous Observations

The non-simultaneous exposures of 3C382, 3C390.3, Mrk 1018 and Mrk 509 again give very steady light curves. The observation of 1H 0419-577 shows steady source flux, but was impacted by high radiation levels. This lead to several readout interruptions, leaving 32 ks of continuous observation. The second half of the EPICpn observation of Mrk 335 shows a flare of double steady state flux, and later on a raise in background. Again, we select an 82 ks bayesian block of nearly constant count rate to exclude this flare. For light-curves, see Fig. 32.

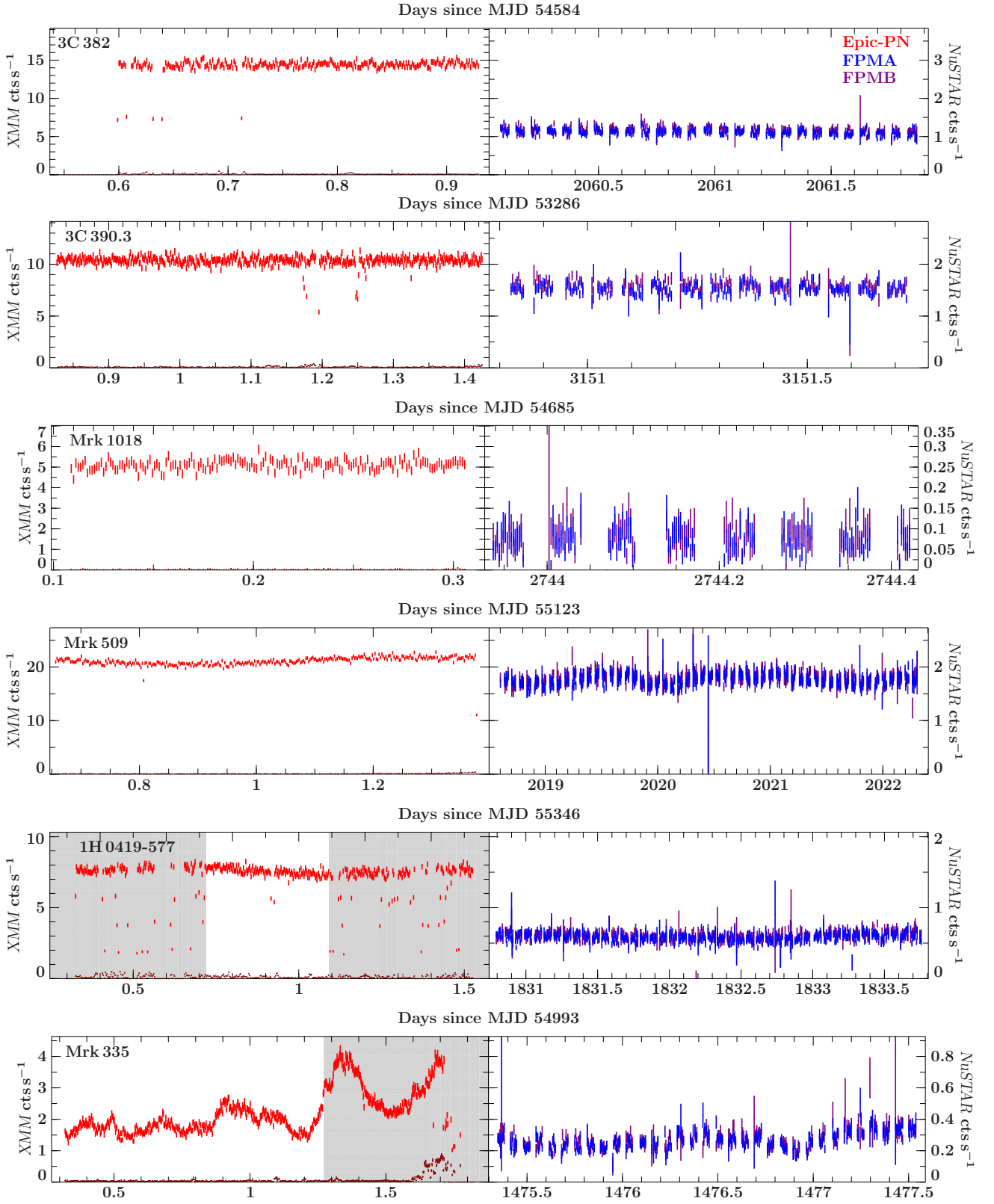


Figure 32: Light-curves taken with the *XMM-Newton* EPICpn (red), PN background (dark red) and *NuSTAR* FPMA (blue) and FPMB (purple). *NuSTAR* light-curves are scaled up with respect to *XMM-Newton* light-curves. Grayed out regions are excluded from spectrum extractions.

5.4 Spectrum Cross Calibration

To compare the behaviour of the both detectors, we perform a simple fit of an analytic power law for each single spectrum. For FPMA and FPMB photon indices are tied, with normalization free to vary. The power law is fitted to the region between 3 keV and 10 keV where both detector's energy ranges overlap. Below 3 keV absorption close to the source and in some cases the thermal component would distort the spectrum, above 10 keV the Compton hump influences the continuum. We also exclude the region between 5 and 7 keV where the most significant Iron reflection features are found.

The Galactic hydrogen absorption is also accounted for, assuming values from the HEASARC N_{H} -Tool (Dickey & Lockman, 1990; Kalberla et al., 2005) and using the TBNEW-model by Wilms et al. (2000). Fit results are listed in Table 3 and residual plots are shown in Fig. 33.

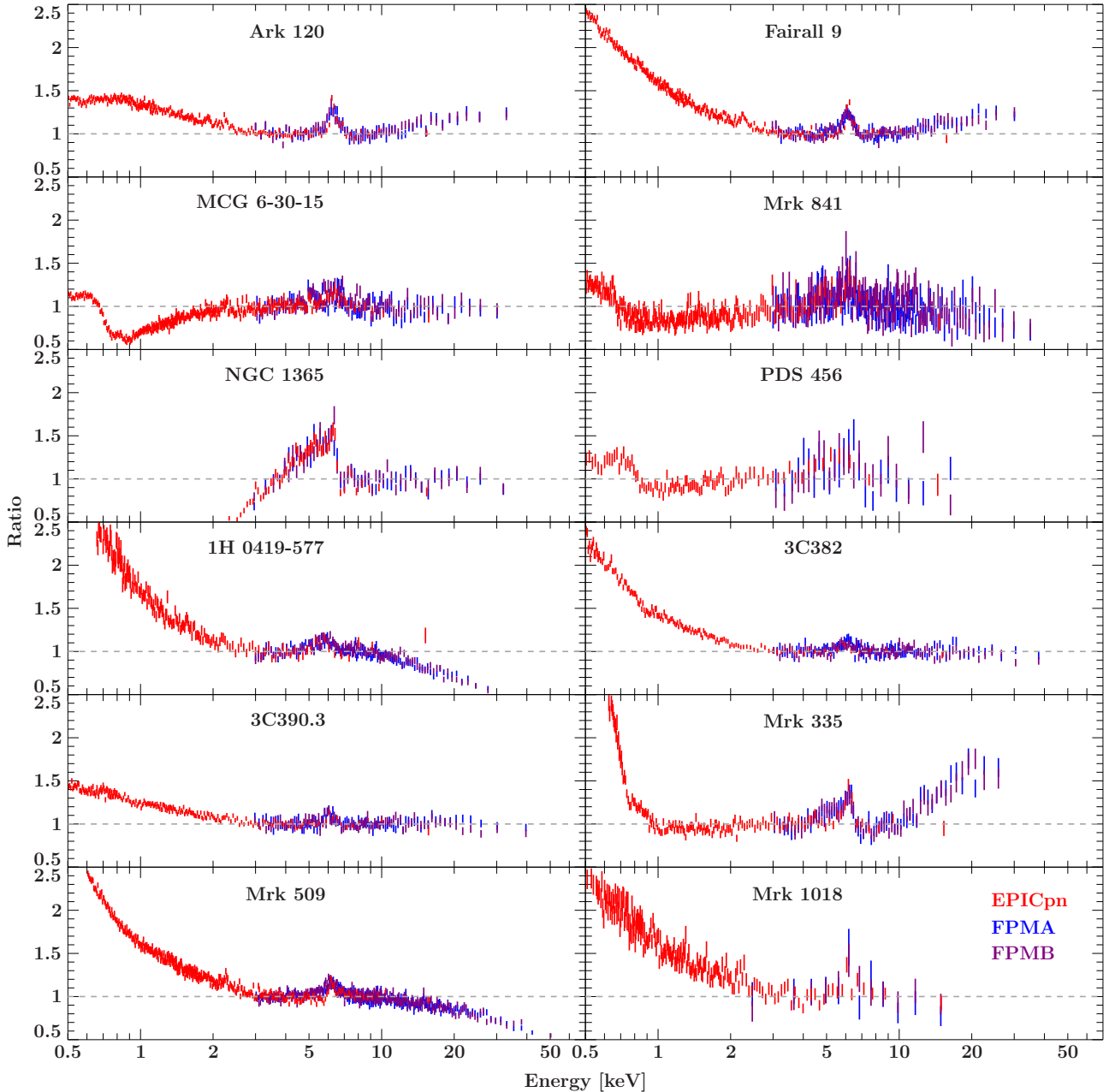


Figure 33: Calibration fits for all EPICpn and FPM spectra. All panels show residuals versus power laws corrected for galactic absorption. Each dataset was fitted to separate power laws for EPICpn and FPM.

Table 3: Galactic hydrogen equivalent column and parameters of the calibration power laws. Although not needed for these fits, we also list source redshifts for further reference.

Source	$n_{\text{H}}^{\text{Gal}}$ (10^{20} cm^{-2})	z	Γ_{EPN}	Γ_{FPM}	$N_{\text{EPN}}/N_{\text{FPMA}}$	$N_{\text{EPN}}/N_{\text{FPMB}}$
Ark 120	9.78	0.0327	1.70 ± 0.02	1.80 ± 0.02	0.80 ± 0.04	0.79 ± 0.04
Fairall 9	3.16	0.0470	1.81 ± 0.02	1.88 ± 0.02	0.91 ± 0.04	0.89 ± 0.04
NGC 1365	1.34	0.00548	1.06 ± 0.03	1.18 ± 0.04	0.83 ± 0.08	0.81 ± 0.07
PDS 456	19.6	0.1840	2.12 ± 0.02	2.12 ± 0.06	1.4 ± 0.2	1.3 ± 0.2
MCG 6–30–15	4.1	0.00758	1.99 ± 0.04	1.76 ± 0.03	1.7 ± 0.2	1.7 ± 0.2
Mrk 841	2.3	0.03642	2.04 ± 0.11	1.48 ± 0.05	2.9 ± 0.6	3.0 ± 0.6
Mrk 335	4.26	0.0258	1.54 ± 0.05	1.86 ± 0.04	0.42 ± 0.04	0.4 ± 0.04
3C 382	6.98	0.05787	1.75 ± 0.03	1.71 ± 0.02	1.39 ± 0.08	1.33 ± 0.07
3C 390.3	3.47	0.0561	1.72 ± 0.02	1.63 ± 0.02	0.83 ± 0.04	0.78 ± 0.04
1H 0419–577	2.03	0.104	1.62 ± 0.05	1.28 ± 0.02	2.0 ± 0.2	2.0 ± 0.2
Mrk 509	4.1	0.03501	1.67 ± 0.022	1.48 ± 0.01	1.64 ± 0.06	1.64 ± 0.06
Mrk 1018	2.6	0.04296	1.64 ± 0.08	1.5 ± 0.2	12 ± 4	11 ± 5

The simultaneous observations of Ark 120, Fairall 9 and NGC 1365 show cross calibration constants in the expected range for *NuSTAR* and *XMM-Newton* joint observations with slightly flatter power laws and lower fluxes for *XMM-Newton* data (compare table 3). While the FPM calibration constant $\frac{N_{\text{FPMA}}}{N_{\text{FPMB}}} = 0.97 \pm 0.03$ agrees for all observations, the flux and photon index deviations between *NuSTAR* and *XMM-Newton* are consistent with those observed by Madsen et al. (2015). The remaining simultaneous observations deviate from the known calibration, but we remind that due to variability (see Sec. 5.3.2), we expect an additional error of 5% on the photon index. Also, later on when using physical models in Sec. 6 we find that all of these spectra can be modelled with a common power law index. Leaving normalization constants between FPM and EPICpnto vary freely, they find values in the range of the first three sources.

For the non-simultaneous observations, especially those of variable sources, the power law parameters cannot be expected to agree, so for any further fitting these parameters will be kept separate. Also, the highest energy bin of *XMM-Newton* data is visibly poorly cross calibrated, so from now on we only consider *XMM-Newton* data up to 10 keV. 3C 382 and 3C 390.3 nevertheless find agreeing power law indices, we will use this result in the physical models to prevent parameter degeneracies. Residuals of the power law fits (Fig. 33) highlight the features of reflection in all sources. All spectra feature distinctly broad iron lines and compatible shapes in the 5-7 keV Fe-band. This motivates the assumption that we can also fit non-simultaneous spectra with tied reflection parameters, but untied power law parameters.

All *XMM-Newton* observations except that of NGC 1365 feature a notable soft excess above the absorbed power law continuum. The low energy dip in the spectrum of NGC 1365 is commonly attributed to strong absorption close to the source by a hydrogen equivalent column on the order of 10^{23} atoms per cm^{-2} (Risaliti et al., 2013; Walton et al., 2014). The flatter excesses of the remaining sources are typical of low energetic cold and blurred reflection lines. The dips, edges and steepenings in the soft excesses of some sources can mostly be explained by multi-layered, ionized or partially covering absorption or the tail of the accretion disk black-body radiation. These details will be covered for each source individually. The model components we found to be required to fit each single source are given in Table 4.

5.5 Modelling

We now apply models including cold distant reflection (CDR) and relativistic reflection (RR) to the data. For data visualization, model calculation and spectral fitting purposes we use the Interactive Spectral Interpretation System (ISIS) version 1.6.2-36. All model components are redshifted according to the values from Table 3. For the power law, black-body and partial covering components we use the according XSPEC-implementation included in ISIS. The different model components used through the course of this analysis are:

- **detconst**: A multiplicative cross calibration constant for each spectrum. Detector constants are allowed to float, but checked to be consistent with the results of Sec 5.4.
- **galabs**: For galactic foreground absorption we use the TBNEW-model by Wilms et al. (2000), fixed at the hydrogen equivalent columns given in Table 3 and solar abundances.
- **power law**: Analytical power law as explained in detail in Sec. 2.4.2.
- **warmabs**: Fast outflowing material intervening the line of sight. We use a table based on the photoionization-code XSTAR that was originally calculated for an analysis of NGC 1365 by D. Walton (priv. comm.).
- **pcabs**: A layer of absorbing material covering a fraction of the source. The XSTAR-based model ZXIPCF was introduced by Reeves et al. (2008). A general discussion of warm and partial covering absorption can be found in Beuchert (2013).
- **CDR**: Cold distant reflection is modelled using the XSTAR-derived XILLVER tables from Garcia et al. (2013) fixed at a neutral value of $\log \xi = 1$.
- **RR**: Relativistic reflection is modelled using the different RELXILL-implementations, see later in this section. Being the main focus of this work, we use three different variants, to be introduced in the following section.
- **tbody**: In some of the soft excesses a thermal component remains, that can be fitted empirically by a black body. For a short explanation see also Ballhausen (2015). The spectral shape is given by:

$$F \sim \frac{E^2 dE}{kT^4 (e^{E/kT} - 1)} \quad (43)$$

Table 4: Models for each single source and total number of parameters. For the three different reflection models.

Source	Model	free parameters (Model I/II/III)
Ark 120	detconst*galabs*(powerlaw+CDR+RR)	12/11/10
Fairall 9	detconst*galabs*(powerlaw+CDR+RR)	12/11/10
PDS 456	detconst*galabs*warmabs*(powerlaw+RR)	13/12/11
NGC 1365	detconst*galabs*pcabs*(powerlaw+CDR+RR-gauss)	18/17/16
MCG 6-30-15	detconst*galabs*warmabs*warmabs*(powerlaw+CDR+RR)	16/15/14
Mrk 841	detconst*galabs*(powerlaw+CDR+RR)	12/11/10
3C 382	detconst*galabs*(powerlaw+CDR+RR)	12/11/10
3C 390.3	detconst*galabs*(powerlaw+CDR+RR)	12/11/10
Mrk 335	detconst*galabs*pcabs*(tbody+powerlaw+CDR+RR)	15/14/14
1H 0419+577	detconst*galabs*(powerlaw+CDR+RR)	13/12/12
Mrk 509	detconst*galabs*(tbody+powerlaw+CDR+RR)	15/14/14
Mrk 1018	detconst*galabs*(powerlaw+CDR+RR)	13/12/12

For each source we begin with fitting a generic model of power law, CDR and RR components. While in most cases the iron complex and high energy region can be well fitted, we find that for some sources additional absorption and excess components are necessary (Table 4). The motivation for including specific components will be discussed in the treatment of individual sources. According to literature, most of these sources show some signs of warm absorption, but often these features are subtle to detect at CCD resolutions. We only include additional components where they have a significant impact on the broadband spectral shape and influence the fit of the reflection components.

Relativistic Reflection

For CDR and RR, the illuminating power law index, disk inclination and iron abundance are tied to reduce parameter degeneracies. These assumptions are also physically justified as we assume the illumination to come from the same source and to be reflected by different parts of the same disk. For the full list of physical parameters relevant to this analysis, see Table 5. To examine the relativistic reflection, we use the following three different models in direct comparison. The primary motivation for this comparison is to gain insight whether the purely empirical emissivity profile can be replaced by the physically consistent lamppost model.

MODEL I: The RELXILL model calculates the reflection spectrum based on a radius-dependent emissivity (see Sec. 2.5). The emissivity profile is given by a broken power law with indices ϵ_1 , ϵ_2 and breaking radius r_{br} . For non-relativistic reflection of a point source illuminated disk we expect the reflected flux to be $F \propto r^{-3}$, only deviating in the strong field region close to the SMBH Dauser (2014). So we generally fix the outer emissivity index at $\epsilon_2 = 3$ and fit breaking radius and inner index. Note that the broken profile is still a simplification and that the inner power law is averaging over a more complicated profile. The model is based on the XSTAR derived X-ray reflection code XILLVER by García & Kallman (2010); García et al. (2013). The reflection spectrum is convolved with the relativistic line blurring model RELLINE by Dauser et al. (2010). For each point on the disk relativistic deviations of emission angles are taken into account. A full description of the RELXILL model can be found in García et al. (2014) and Dauser (2014). Including this emissivity profile model, we are also able to compare our results directly to Walton (2013) who used the closely related RELCONV on his sample.

MODEL II: The RELXILLP model is variant of the RELXILL model, where the shape of the emissivity profile is derived from an isotropically radiating source on the rotation axis of the system. The three parameters of the emissivity profile are reduced to one parameter, the height of the lamppost source. The normalization of the reflected spectrum is allowed to vary. As primary reference see Dauser et al. (2013).

MODEL III: The RELXILLP model optionally allows not only the shape of the reflected spectrum, but also the intensity of the reflected radiation to be calculated self-consistently from the height of the primary power law source. This removes the reflection normalization from the free parameters.

Table 5: Physical parameters of the relativistic reflection models with the typical parameter ranges found in this sample study.

Parameter	Description	Typical values
Γ	Photon index of the primary power law	1.5 - 2.5
a	Spin parameter of the SMBH	0.7 - 0.998
i	Inclination angle between disk normal and line of sight	10° - 80°
$\log \xi$	Ionization parameter of the inner accretion disk edge	2 - 3
A_{Fe}	Iron abundance of accreted material in solar units	0.1 - $10 A_{\text{Fe}}^\odot$
ϵ_1	Inner index of disk emissivity profile	3 - 10
ϵ_2	Outer index of disk emissivity profile	3 (fixed)
r_{br}	Emissivity profile breaking radius	2 - $5 r_g$
h	Lamppost source height above the accretion disk	1 - $10 r_g$
f_{refl}	Fraction between radiation hitting the disk and escaping directly	0.5 - 10

A parameter of special interest is the reflection fraction f_{refl} , which is defined as the ratio of coronal intensity illuminating the disk to the primary emission’s intensity reaching the observer. In a classical case of a disk illuminated by a point source above the disk, the reflection fraction is 1. In the case of a lamppost source situated above the black hole, light paths are bent downward and thus a larger intensity hits the disk, so we expect f_{refl} to increase above 1 (Dauser et al., 2016). Due to this definition, the reflection fraction only depends on the lamppost height or respectively the emissivity profile parameters.

5.6 Comparing reflection models: Ark 120

Being the spectrum with the most obvious reflection features and showing no signs of absorption, we choose Ark 120 for a more detailed comparison of different reflection models. We use the basic model shape given in table 4. For comparison, we include the angle averaged convolution model RELCONV by Dauser et al. (2010) that was used in the Walton et al. (2013) analysis of the same source, but with a different data set acquired with *Suzaku*.

In the RELXILLP models, the disk emissivity profile is determined by the height of the lamppost source. We distinguish between a self-consistent version, where also the flux of the reflection component is inferred from the strength of the primary power law and a free reflection model, where the normalization of the reflection component is free to vary. We also include a model of two lamppost components at different lamppost heights (see Table 6).

Table 6: The different models applied to the simultaneous Ark 120 spectrum.

Name	RR Component	Annotation	free parameters
Relconv	relconv(reflionx)		12
Relkill	relkill		12
fixed LP	relxillp	fixrefl_frac=True	10
free LP	relxillp	fixrefl_frac=False	11
double LP	relxillp(1)+relxillp(2)	fixrefl_frac=True	12

For all different RELXILL-models, we find consistent power law indices, Fe abundances, Ionization parameters and spin parameters where generally spins are constrained close to the upper limit (See table 7). The inclinations all lie in the intermediate range of 40 - 60°, but do not generally agree within confidence intervals. This range is consistent with Walton (2013) as well as Nardini et al. (2011). Compared to the Walton (2013) measurements, we find a large increase and closer constraints of the spin. As even our RELCONV-model shows the increased spin value, we attribute this behaviour to the increase in data quality and especially spectral range as opposed to a model intrinsic increase.

Compared to Walton (2013), we measure a significantly harder power law, a significantly stronger disk ionisation and steeper emissivity profile. The spectral hardening and increased ionisation could be explained by a rise in accretion rate and coronal temperature between the 2007 *Suzaku* and the 2013 join *XMM-Newton* and *NuSTAR* observation.

Table 7: Best fit parameters with 90%-confidence intervals for different reflection models applied to Ark 120 data. χ^2/N_{dof} is calculated at a binning of minimum S/N = 5. The reflection fractions in brackets are inferred not fitted, but from the lamppost height. Also included are the results of Walton et al. (2013)

Model	Γ_1	A_{Fe} (A_{Fe}^{\odot})	$\log \xi$	ϵ_1/h ($-/r_{EH}$)	r_{br} (r_g)	a	i ($^{\circ}$)	f_{refl}	χ^2/N_{Bins}
Relconv (Walton)	2.14 ± 0.01	$1.8^{+0.2}_{-0.3}$	0.8 ± 0.025	$5.1^{+2.8}_{-1.1}$?	$0.64^{+0.19}_{-0.11}$	47^{+7}_{-2}	-	1274/1176
Relconv	1.889 ± 0.008	$1.28^{+0.13}_{-0.14}$	2.56 ± 0.05	> 9.3	$3.5^{+16.5}_{-0.4}$	$0.949^{+0.025}_{-0.037}$	65 ± 5	-	2953/2605
Relkill	1.938 ± 0.009	4.1 ± 0.4	$2.80^{+0.05}_{-0.04}$	> 9.8	2.78 ± 0.09	> 0.991	$38.1^{+2.6}_{-3.2}$	$3.0^{+0.8}_{-0.4}$	2858/2605
fixed LP	$1.904^{+0.008}_{-0.006}$	$2.95^{+0.11}_{-0.18}$	2.751 ± 0.016	$3.36^{+0.09}_{-0.16}$		$0.994^{+0.003}_{-0.004}$	$40.1^{+1.9}_{-1.6}$	(2.525)	3098/2605
free LP	$1.943^{+0.011}_{-0.010}$	3.9 ± 0.4	$2.733^{+0.016}_{-0.027}$	$1.124^{+0.003}_{-0.004}$		> 0.9979	$53.4^{+1.5}_{-1.8}$	$0.52^{+0.03}_{-0.13}$	2956/2605
double LP	$1.932^{+0.010}_{-0.009}$	$3.60^{+0.33}_{-0.26}$	$2.750^{+0.04}_{-0.03}$	< 1.1 260^{+120}_{-80}		> 0.9977	$53.5^{+1.9}_{-3.6}$	(20.9) (0.383)	2865/2605

While we find acceptable fits with all models, the angle-averaged model gives a significantly worse fit than the angle resolved RELXILL. The self-consistent model produces the worst, yet still acceptable fit. Freeing the reflection fraction from the lamppost height significantly improves the fit. When adding a second lamppost component, the first lamppost height as well as all other reflection parameters stay consistent to those of the free reflection fraction model, and the fit reaches the same goodness of fit as the broken emissivity profile. The second lamppost component is found at a factor 10 lower normalization and very weakly constrained to several hundred r_{EH} suggesting a weak vertically extended component.

In Fig. 34 we show a decomposition of the models into the primary and reflected components. We see striking differences between the best fitting convolution model, the angle-resolved model and the lamppost model, where the latter two produce a more distinct Fe-edge and a steeper Compton hump. The reflection components of the three different lamppost models are very similar in spite of the differences in lamppost height and reflection fraction between the free and self-consistent lamppost.

The second relativistic component of the best-fit double lamppost is comparable in flux to the cold distant reflection. While a weaker, extended part of the lamppost source remains a possibility, this part of the spectrum might also be a result of the simplified assumption of one distant reflector at fixed ionisation. A non-relativistic reflection component scattered of a disk with an ionization gradient might produce the same result.

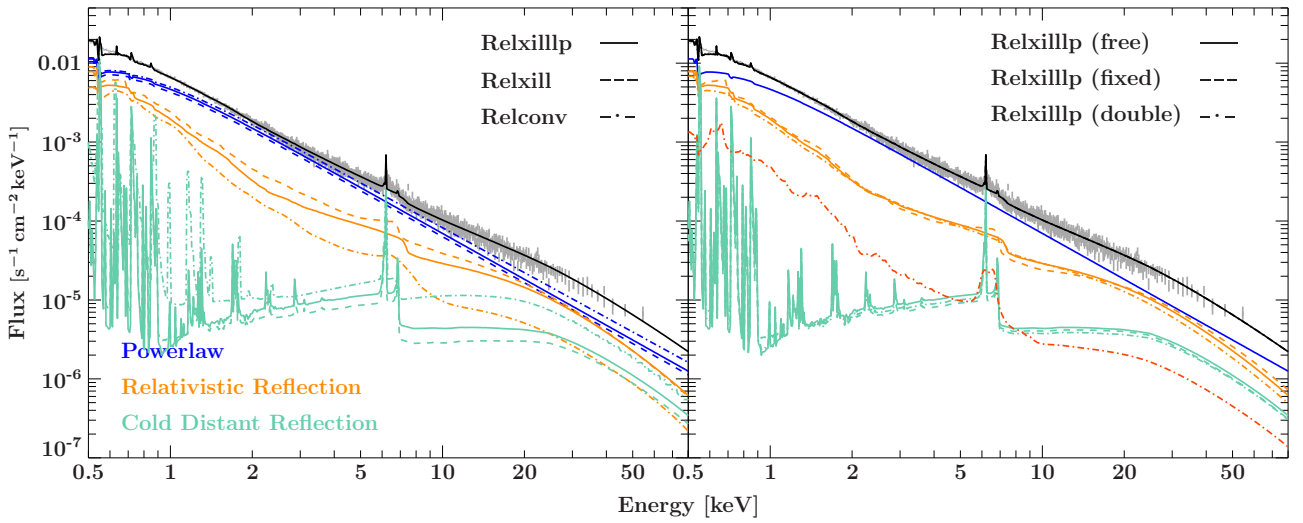


Figure 34: Comparison of different reflection model fits with respective components. Summed model in black with data in the background. Note that CDR is generally tied to the respective RR component via inclination and iron abundance parameters. Right panel: The second component of the double lamppost model is displayed in red.

6 Sample Analysis

We now fit the whole sample using three different reflection models and the additional continuum components given in Table 4. The models differ only by the component used for the relativistic reflection as listed in sec. 5.5. Considering the calibration fits, we assume the simultaneous observations and the observations with consistent power law parameters of 3C 382 and 3C 390.3 to be modellable by assuming one common spectral model.

To the remaining sources Mrk 335, 1h0419–577, Mrk 509 and Mrk 1018, separate power laws are fitted separately for individual observations, while all physical parameters are kept tied. The best fit parameters are given in tables 8 - 10 with 90%-confidence intervals. χ^2/N_{dof} is calculated at a binning according to a minimum signal-to-noise of 5. *XMM-Newton* data above 10 keV and *NuSTAR* data below 4 keV are omitted due to uncertain calibration in these regions.

6.1 Model I: Relxill - Parameters

The following fitting strategy generally works well to quickly find the global minimum: All physical parameters are set to intermediate values (with regard to Table 5) or, where available, to the values of the Walton et al. (2013) study. Then parameters are untied groupwise from broad to subtle spectral features and refitted. A good working order is as follows:

1. normalization parameters, detector constants, hydrogen equivalent columns
2. photon index, black body temperature
3. ionization, iron abundance
4. inclination
5. emissivity profile breaking radius and inner index
6. spin parameter

The measured photon indices (Table 8) generally do not match those measured during cross calibration, as for all components reflection and absorption influence the spectral slope even in the seemingly flat 3-5 and 7-10 keV ranges. We find high spins throughout and relatively large reflection fractions. Emissivity profile breaking radii lie in the typical range of 3-5 r_g (Dauser et al., 2013). The found inner emissivity indices are generally higher than those given by Walton (2013), but this is likely a result of our freely fitted breaking radius, where Walton (2013) only fitted the emissivity index of a single power law profile.

Table 8: Best fit parameters with 90%-confidence intervals for Model I applied to the whole sample. χ^2/N_{dof} is calculated at a binning of minimum S/N = 5.

Source	Γ_1 Γ_2	A_{Fe} (A_{Fe}^{\odot})	$\log \xi$	ϵ_1	r_{br} (r_g)	a	i ($^{\circ}$)	$f_{\text{relxill}}^{\text{refl}}$	χ^2/N_{dof}
Ark 120	1.938 ± 0.009	4.1 ± 0.4	$2.80^{+0.05}_{-0.04}$	> 9.8	2.78 ± 0.09	$0.9934^{+0.0046}_{-0.0024}$	$38.1^{+2.6}_{-3.2}$	$3.0^{+0.8}_{-0.4}$	2858/2605
Fairall 9	$2.006^{+0.007}_{-0.019}$	$4.65^{+0.30}_{-0.33}$	3.051 ± 0.006	> 9.8	$3.21^{+0.10}_{-0.06}$	$0.9960^{+0.0014}_{-0.0013}$	$28.4^{+1.7}_{-1.9}$	> 12	2770/2638
PDS 456	$2.00^{+0.05}_{-0.04}$	> 6	$3.31^{+0.06}_{-0.08}$	> 7.5	$2.28^{+0.41}_{-0.19}$	> 0.991	57^{+6}_{-5}	$2.8^{+2.2}_{-1.4}$	707/603
NGC 1365	1.84 ± 0.05	$7.1^{+1.9}_{-1.3}$	$2.69^{+0.04}_{-0.20}$	$5.9^{+0.6}_{-0.4}$	$4.0^{+0.9}_{-0.7}$	$0.990^{+0.009}_{-0.027}$	$51.3^{+1.9}_{-1.7}$	$4.5^{+1.9}_{-0.4}$	1723/1638
MCG–6–30–1	2.028 ± 0.021	$1.1^{+4.5}_{-0.5}$	$3.16^{+0.10}_{-0.06}$	> 9.2	2.99 ± 0.26	$0.989^{+0.005}_{-0.009}$	34 ± 7	> 5.1	2114/1989
Mrk 841	$1.917^{+0.028}_{-0.031}$	$0.27^{+0.17}_{-0.16}$	$3.00^{+0.04}_{-0.10}$	> 6.2	$2.8^{+0.9}_{-0.5}$	> 0.941	21^{+7}_{-10}	> 4.1	1156/1083
3C 382	$2.007^{+0.010}_{-0.031}$	$0.91^{+0.33}_{-0.15}$	$2.71^{+0.18}_{-0.10}$	> 7.9	$2.93^{+0.46}_{-0.30}$	> 0.993	47 ± 6	$2.9^{+2.8}_{-0.5}$	2484/2404
3C 390.3	$1.765^{+0.010}_{-0.009}$	> 6.8	$2.74^{+0.06}_{-0.04}$	> 9.7	$2.95^{+0.23}_{-0.17}$	> 0.994	27^{+6}_{-8}	$1.6^{+0.6}_{-0.5}$	2762/2626
Mrk 335	2.08 ± 0.05	$2.8^{+0.9}_{-0.7}$	$2.00^{+0.05}_{-0.25}$	-	-	$0.82^{+0.15}_{-0.50}$	< 25	$2.9^{+1.4}_{-0.8}$	1699/1599
1H 0419–577	$1.91^{+0.08}_{-0.05}$ $1.87^{+0.04}_{-0.05}$ $2.117^{+0.017}_{-0.034}$	< 0.6	$2.70^{+0.10}_{-0.19}$	$7.8^{+2.2}_{-1.2}$	$5.6^{+2.0}_{-2.1}$	$0.961^{+0.027}_{-0.017}$	15^{+20}_{-10}	$8.8^{+9.6}_{-2.0}$	1956/1949
Mrk 509	$1.730^{+0.012}_{-0.011}$ $1.990^{+0.018}_{-0.012}$	$1.33^{+0.29}_{-0.28}$	$3.014^{+0.009}_{-0.011}$	> 9.8	$3.24^{+0.10}_{-0.11}$	> 0.995	$29.1^{+2.2}_{-2.8}$	> 12	3443/3069
Mrk 1018	$1.84^{+0.11}_{-0.12}$ $2.02^{+0.05}_{-0.08}$	$5.0^{+3.8}_{-1.5}$	$2.88^{+0.14}_{-0.12}$	9.3 ± 0.6	$4.05^{+0.22}_{-0.50}$	$0.992^{+0.006}_{-0.004}$	< 22	> 10	709/707

6.2 Model I: Relxill - Residuals

Throughout the sample we achieve reasonably flat residuals. The only remaining residuals appear as line-like features at 1.8 and 2.2 keV in several spectra. These correspond to the energies of the silicon K-edge and the gold M-edges and the according fluorescent lines (Bearden & Burr, 1967). This leads to the assumption that we are seeing calibration inaccuracies surrounding these edges in the mirror effective area (gold) and detector response (silicon). Another possibility would be cosmic background induced fluorescent emission of the detector and mirror material (Kuntz & Snowden, 2008), but the features are too insignificant to discern these scenarios.

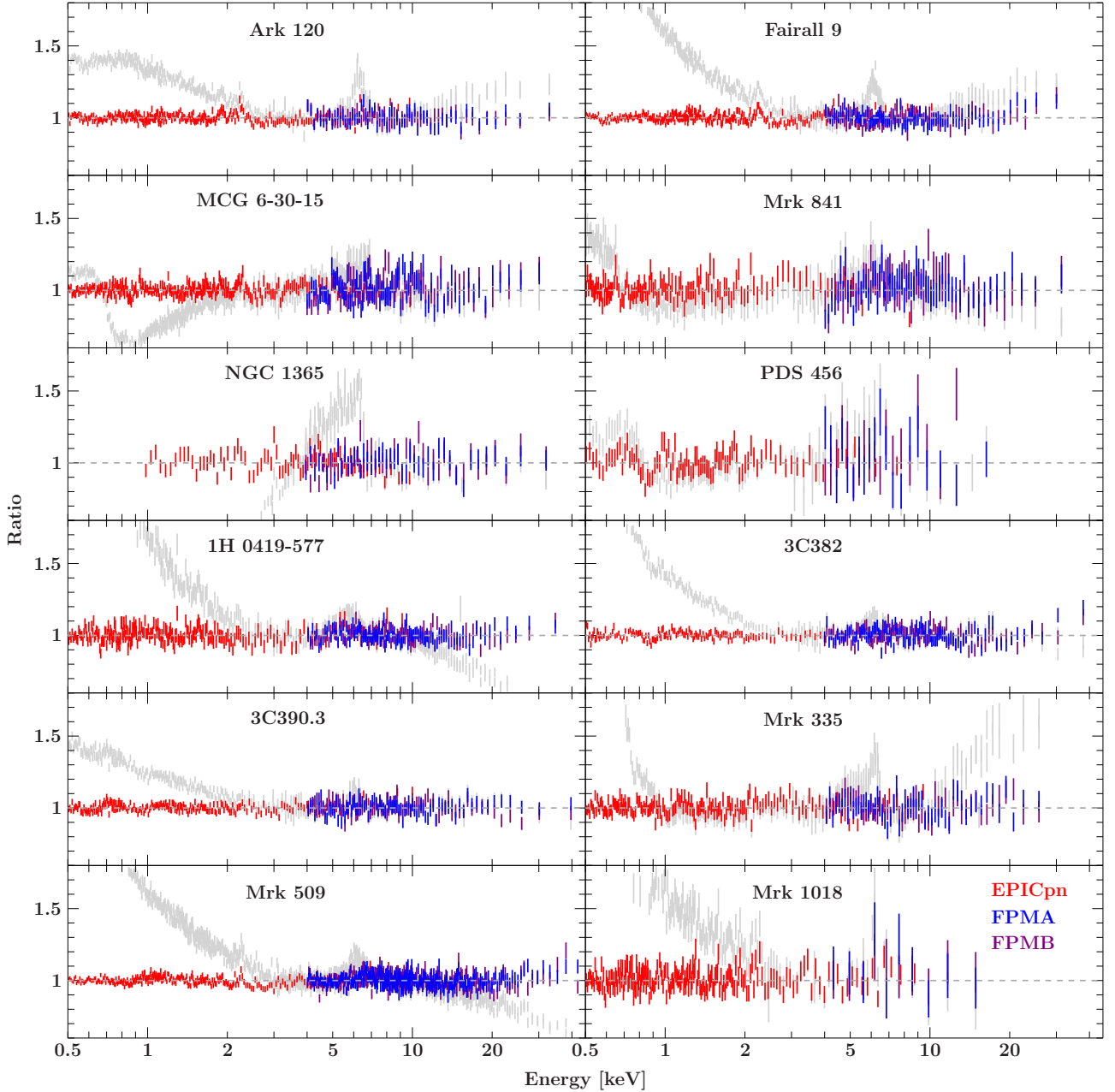


Figure 35: Residuals of the RELXILL model fits according to Table 8. In the background the power law residuals from Fig. 33 are shown to highlight soft excesses and $K\alpha$ -region. Binning is increased for readability.

6.3 Model I: Individual source details

Ark 120: Analyzing *Suzaku* data, Nardini et al. (2011) already concluded that the soft excess of Ark 120 can be completely modelled via soft reflection, these results were confirmed by (García et al., 2014). Thus we keep the basic power law plus reflection model. We find physically reasonable parameters throughout and gain very flat residuals. Around 1.9 keV and 2.2 keV calibration features remain.

Fairall 9: While Schmoll et al. (2009) are able to explain the existing *XMM-Newton* and *Suzaku* data with the same simple power law plus reflection model, Lohfink et al. (2012) find that for some epochs an additional soft component is required. As we immediately acquire flat residuals without adding further complexity, we stay with the basic model. Again we find the lines at 1.9 keV and 2.2 keV already observed for Ark 120. We find a very large reflection fraction.

PDS 456: In an analysis of RGS and EPICpn data Reeves et al. (2003) established that this source features fast outflowing material moving at $\sim 50,000 \text{ km s}^{-1}$. One obvious spectral feature is an absorption trough around 1 keV and produced by a warm absorption column around $5 \times 10^{22} \text{ cm}^{-2}$. We can perfectly reproduce this feature with a column density of $(4.3_{-0.8}^{+1.0}) \times 10^{22} \text{ cm}^{-2}$ and $\log \xi = 2.8$. While Reeves et al. (2009) explain the broadened features of the spectrum through reflection off a high column density of the relativistic outflow, we find that they can as well be modelled by relativistic disk reflection. They also find further iron absorption features around 9 keV, but these are beyond our spectral resolution in this range. Both studies find a strong soft excess, it is not present in our newer (2014) dataset. Including a CDR-component from the beginning of the fit, the CDR-Norm converges to very low values, so we dismiss the XILLVER-component as not significant. This is also confirmed by the absence of a visible thin iron line.

NGC 1365: This source is known to show strong absorption variability (Risaliti et al., 2005). Walton et al. (2014) have shown that the spectral variability can be modelled assuming a constant model of disk reflection, but varying partial covering absorption. Initially using a partial covering model our covering fraction converges to 1, so we accept as model a total obscuration of column density $5.78_{-0.16}^{+0.17} \times 10^{22} \text{ cm}^{-2}$. We also see the small Fe absorption feature at 6.85 keV observed by Risaliti et al. (2013), which we model as a simple Gaussian line. Below 1 keV we find a soft excess that can be modeled at acceptable χ^2 using either a second partial coverer at different ionisation ($\chi_{red}^2 \simeq 1.33$), an additional XSTAR-wind ($\chi_{red}^2 \simeq 1.29$), or a black body soft excess ($\chi_{red}^2 \simeq 1.4$). While we are unable to discern these three models, the choice does not have any impact on the reflection model parameters and only concerns the region below 1 keV. Excluding this region from our analysis we gain a very good fit.

MCG–6-30-15: The prototypical bare AGN was one of the first sources where broadened $K\alpha$ -emission was detected and the possibility of a high black hole spin discussed (Tanaka et al., 1995; Iwasawa et al., 1996). While some observers find the spectrum to be well explained by relativistic reflection (Wilms et al., 2001; Fabian et al., 2002), others argue that the soft part of the spectrum as well as its variability can be explained by complex, multi-layered warm absorption on the order of 10^{22} cm^{-2} (Morales et al., 2000; Miller et al., 2008). Thus, after finding no acceptable fit using only reflection models, we include layers of warm absorption. We find that two absorption layers at different ionization fit the data very well, a nearly neutral hydrogen equivalent column of $n_{\text{H}} = (3.2 \pm 0.8) \times 10^{21}$ and a column of $n_{\text{H}} = (6.9 \pm 1.8) \times 10^{21}$ at $\log \xi \simeq 2$. These absorption structures are consistent with those analyzed by Marinucci et al. (2014b) in much greater detail. We find an even steeper emissivity profile than Wilms et al. (2001) (breaking radius at $6 r_{\text{g}}$), note however that we used a fixed outer emissivity index. The fitted inclination is consistent with $i \simeq 30^\circ$ found by Tanaka (1995) and Fabian (2002).

Mrk 841: Longinotti et al. (2010) find features of lower density ($N_{\text{H}} = 10^{21} \text{ cm}^{-2}$) warm absorption in RGS data, but also confirmed that the absorption has no significant impact on the shape of the iron $K\alpha$ complex. We see no significant absorption features in our EPICpn data set. Although older *XMM-Newton* observations have shown a strong soft excess up to a factor of 2.5 above continuum (Petrucci et al., 2007) the soft excess in our 2014 data is moderate and can completely be accounted for by soft reflection lines. We acquire acceptably flat residuals without adding any complexity to the basic reflection models. However, the comparably short duration observation has a much worse signal to noise compared to the preceding ones.

3C 382: Torresi et al. (2010) and Reeves et al. (2009) report subtle features of warm absorption from *Chandra* and *XMM-Newton* gratings data. At low column densities ($N_{\text{H}} \simeq 10^{21} \text{ cm}^{-2}$) these are beyond our resolution and have no significant impact on the broad spectrum. We start fitting the time separate spectra of 3C 382 using a common power law and reflection model and find a good fit. When untying the photon index, $\log \xi$ and ϵ_1 -parameters, they converge to values consistent with each other, so we leave them tied for further analysis. Much like for Ark 120 and Fairall 9, the soft excess can be completely fitted by soft reflection lines. Our findings are well consistent with those of Sambruna et al. (2011). From a 2007 *Suzaku* observation they determined inner accretion disk parameters of $\log \xi \simeq 3$ and $i \simeq 30^\circ$ and also find that there is no further requirement for a soft excess component apart from reflection.

3C 390.3: Sambruna et al. (2009) reported that this source shows very low intrinsic absorption and a significant double peaked iron feature. Across multiple datasets from 2004 to 2007 they observe Photon indices from 1.77 to 1.93. They also find a strongly ionized reflection at $\log \xi \simeq 3.4$, but argue that the broad iron line is produced by radiation outside $20 r_g$. Walton et al. (2013) noted that Giovannini et al. (2001) put radio constraints on the jet inclination of 3C 390.3 at $i = 30 - 35^\circ$. Our fit agrees well with these values. Similarly to our 3C 382, we are able to fit both datasets with a common power law.

Mrk 335: These spectra are not fittable by a common power law and reflection model at a $\chi_{red}^2 = 5$, so we untie photon indices first and gain largely flat residuals apart from a significant soft excess. The soft excess can be modeled using a black-body of 0.11 keV as was first found by Pounds et al. (1987). However, visible residuals remain around the edge of the soft excess. Motivated by the strongly variable light-curve, we include a neutral partial covering component and find the best fit column at $1.21_{-0.18}^{+0.24} \times 10^{22}$. We find the black-body temperature at $0.117_{-0.008}^{+0.022}$ keV to perfectly agree with literature. Though finding flat residuals throughout, we are unable to constrain the parameters of the emissivity profile. As with the 3C sources, untying the $\log \xi$ and ϵ_1 -parameters for the separate spectra does not significantly change or improve the fit.

1H 0419-755: This source has been observed to be subject to strong variability, which has often been attributed to complex absorption (Page et al., 2002; Pounds et al., 2004). Newer studies from Fabian et al. (2005); Pal & Dewangan (2013) have shown that this source can more easily be described by a variable primary source and disk reflection model, eliminating any need for strong absorption. At photon indices around 2, we observed the source in its high flux state like the quoted studies. We can not fit the datasets to a common power law, so we also use models with untied photon indices. Otherwise, the spectrum behaves like Ark 120 and Fairall 9 with the flat soft excess completely accounted for by soft reflection.

Mrk 509: Mehdipour et al. (2011) investigated the strong variable soft excess of this source. They concluded that it is unlikely to be produced by disk black-body emission but rather by Comptonized disk seeded emission. After an initial fit of two separate power laws, we also see significant residuals below 1 keV. As a detailed study of the origins of soft excess emission is beyond our scope, we include a phenomenological black-body component. At a temperature of $kT = 0.036 \pm 0.009$ keV we reach a significantly improved fit from $\chi_{red}^2 = 1.28$ to 1.12, without any soft residuals.

Mrk 1018: Using individual power laws and reflection, no further complexities remain in the spectrum. In spite of the low exposure and high S/N we are able to significantly constrain all parameters.

6.4 Model II: Relxillp - Parameters

As starting point, we use the fit results gained in Model I, only exchanging the RR-component. The physical parameters of the Model II RR-component are set to those gained with Model I and kept fixed, then the lamppost height and reflection fraction are fitted. Then the rest of the parameters is untied and refitted in the order given before. As we generally find very low lamppost heights, we measure heights in units of the event horizon. From a statistics point of view, we generally find slightly worse, though still acceptable fits using the free lamppost models. Spin parameters are closer constrained towards higher values. While Photon indices, iron abundances and ionisation parameters stay consistent, there is a visible trend towards measuring higher inclinations. Where in the emissivity profile for five source we only could put lower limits on f_{ref} , we are now able to constrain all but one source to intermediate values. The low lamppost heights are consistent with the generally steep inner emissivity profiles (compare Sec. 2.5).

Table 9: Best fit parameters with confidence intervals for Model II applied to the whole sample. χ^2/N_{dof} is calculated at a binning of minimum S/N = 5.

Model II	Γ	A_{Fe} (A_{Fe}^{\odot})	$\log \xi$	h (r_{EH})	a	i ($^{\circ}$)	f_{refl}	χ^2/N_{dof}
Ark 120	$1.943^{+0.011}_{-0.010}$	3.9 ± 0.4	$2.733^{+0.016}_{-0.027}$	$1.1240^{+0.0024}_{-0.0039}$	> 0.9979	$53.4^{+1.5}_{-1.8}$	$0.522^{+0.029}_{-0.128}$	2956/2605
Fairall 9	$2.040^{+0.008}_{-0.010}$	3.0 ± 0.4	$2.839^{+0.001}_{-0.013}$	$1.141^{+0.007}_{-0.005}$	$0.9955^{+0.0003}_{-0.0003}$	$49.62^{+0.12}_{-1.01}$	$2.12^{+0.08}_{-0.05}$	2997/2638
PDS 456	2.02 ± 0.04	> 6	$3.31^{+0.07}_{-0.10}$	$1.38^{+0.74}_{-0.19}$	> 0.982	61^{+6}_{-7}	$0.81^{+0.08}_{-0.21}$	711/603
NGC 1365	$1.895^{+0.083}_{-0.026}$	$8.2^{+1.0}_{-2.9}$	$2.70^{+0.04}_{-0.38}$	$1.53^{+0.13}_{-0.04}$	> 0.9627	52.0 ± 1.4	$5.2^{+0.4}_{-0.8}$	1703/1638
MCG-6-30-15	$2.043^{+0.024}_{-0.025}$	$0.41^{+0.13}_{-0.12}$	$3.04^{+0.17}_{-0.16}$	19^{+28}_{-15}	-	24^{+9}_{-19}	$1.0^{+0.5}_{-0.4}$	2106/1989
Mrk 841	$1.880^{+0.027}_{-0.026}$	$0.24^{+0.12}_{-0.13}$	$3.00^{+0.06}_{-0.10}$	$3.5^{+2.5}_{-1.2}$	> 0.52	27^{+5}_{-7}	> 4.6	1193/1079
3C 382	$1.998^{+0.009}_{-0.007}$	$0.95^{+0.35}_{-0.13}$	$2.699^{+0.016}_{-0.062}$	< 1.015	> 0.9978	$50.8^{+1.6}_{-4.2}$	0.422 ± 0.004	2490/2404
3C 390.3	$1.737^{+0.008}_{-0.007}$	$3.2^{+0.4}_{-0.5}$	$3.000^{+0.011}_{-0.087}$	$9.6^{+5.1}_{-1.9}$	> 0.6778	> 78.3	$1.15^{+0.34}_{-0.21}$	2821/2626
Mrk 335	$2.14^{+0.04}_{-0.09}$	$2.3^{+0.8}_{-0.4}$	$2.00^{+0.15}_{-0.18}$	$1.08^{+0.20}_{-0.09}$	$0.62^{+0.16}_{-0.30}$	23^{+6}_{-11}	$0.99^{+0.14}_{-0.13}$	1691/1599
1H 0419-577	$1.87^{+0.08}_{-0.06}$	< 0.65	$2.699^{+0.005}_{-0.037}$	< 1.095	$0.9909^{+0.0001}_{-0.0003}$	$35.0^{+1.5}_{-0.9}$	$2.78^{+0.15}_{-0.10}$	2184/1949
Mrk 509	$1.814^{+0.012}_{-0.010}$	$0.72^{+0.06}_{-0.05}$	$2.699^{+0.007}_{-0.033}$	$1.1192^{+0.0014}_{-0.0011}$	> 0.9979	$41.1^{+1.3}_{-0.7}$	$0.908^{+0.046}_{-0.023}$	4125/3069
Mrk 1018	$1.9914^{+0.0027}_{-0.0036}$	1.8 ± 0.5	$3.00^{+0.09}_{-0.25}$	7^{+12}_{-6}	-	> 71	$3.9^{+4.1}_{-2.5}$	714/712
	$1.79^{+0.12}_{-0.11}$							
	$1.902^{+0.026}_{-0.028}$							

6.5 Model III: Relxillp (self-consistent) - Parameters

We now fit a self-consistent model, deriving the reflection fraction directly from the fitted lamppost height. The time-variable models are again fitted to different power laws, and we allow the lamppost heights to vary. Results are given in Table 10.

Using the self-consistent model, we find the best fits for PDS 456, NGC 1365 but slightly worse fits for Ark 120 and Fairall 9 while power law, Iron abundance and ionisation stay consistent, also inclinations are closer to the values of the emissivity profile. Compared to the free lamppost fit, lamppost heights are found at more intermediate values and for PDS 456, MGC 6-30-15 and 3C 382 constraining the spin is no longer possible. The time-separate spectra still yield acceptable fits, with slight variation in the lamppost height of 1H 0419-577.

Table 10: Best fit parameters with confidence intervals for the whole sample. χ^2/N_{dof} is calculated at a binning of minimum S/N = 5. Note that f_{refl} is no longer a fitted parameter but inferred from h .

Model III	Γ	A_{Fe} (A_{Fe}^{\odot})	$\log \xi$	h (r_{EH})	a	i ($^{\circ}$)	f_{refl}	χ^2/N_{dof}
Ark 120	$1.904^{+0.008}_{-0.006}$	$2.95^{+0.11}_{-0.18}$	2.751 ± 0.016	$3.36^{+0.09}_{-0.16}$	$0.994^{+0.003}_{-0.004}$	$40.1^{+1.9}_{-1.6}$	(2.525)	3098/2605
Fairall 9	2.005 ± 0.007	$2.35^{+0.12}_{-0.29}$	$2.831^{+0.034}_{-0.029}$	$2.89^{+0.30}_{-0.13}$	$0.992^{+0.005}_{-0.004}$	$32.0^{+2.2}_{-2.6}$	(2.882)	3165/2638
PDS 456	2.15 ± 0.04	> 6	$3.31^{+0.14}_{-0.39}$	23^{+106}_{-18}	-	50^{+8}_{-9}	(0.892)	664/603
NGC 1365	$1.904^{+0.130}_{-0.028}$	$5.80^{+1.00}_{-0.04}$	$2.698^{+0.009}_{-0.256}$	$1.85^{+0.06}_{-0.07}$	> 0.9797	$51.1^{+1.3}_{-1.5}$	(6.034)	1699/1638
MCG-6-30-15	$2.036^{+0.027}_{-0.018}$	0.42 ± 0.11	$3.01^{+0.08}_{-0.11}$	18^{+18}_{-9}	-	25^{+6}_{-7}	(1.106)	2108/1989
Mrk 841	$1.876^{+0.029}_{-0.023}$	$0.24^{+0.11}_{-0.13}$	$3.00^{+0.07}_{-0.12}$	< 1.23	$0.79^{+0.06}_{-0.61}$	$33.7^{+2.9}_{-3.7}$	(1.813)	1196/1079
3C 382	$2.007^{+0.007}_{-0.006}$	0.54 ± 0.10	-	-	-	-	-	
3C 390.3	1.737 ± 0.006	3.2 ± 0.4	$3.000^{+0.010}_{-0.081}$	$10.5^{+1.9}_{-6.9}$	> 0.8795	> 78.6	(1.292)	2816/2626
Mrk 335	$2.14^{+0.06}_{-0.08}$	$2.6^{+0.6}_{-0.5}$	$2.01^{+0.18}_{-0.16}$	$1.138^{+0.028}_{-0.063}$	$0.69^{+0.13}_{-0.18}$	24^{+5}_{-7}	(1.466)	1712/1599
	$1.88^{+0.05}_{-0.06}$			$1.17^{+0.09}_{-0.06}$			(1.484)	
1H 0419-577	$1.899^{+0.017}_{-0.024}$	0.65 ± 0.08	$2.699^{+0.009}_{-0.035}$	$1.090^{+0.016}_{-0.091}$	> 0.9978	$37.7^{+3.1}_{-2.7}$	(22.481)	2156/1949
	1.977 ± 0.013			$1.51^{+0.05}_{-0.08}$			(9.374)	
Mrk 509	$1.933^{+0.012}_{-0.010}$	0.54 ± 0.04	$2.749^{+0.012}_{-0.011}$	$1.441^{+0.012}_{-0.011}$	> 0.99786	< 6.9	(10.535)	4217/3187
	$1.989^{+0.004}_{-0.003}$			$1.690^{+0.029}_{-0.011}$			(7.243)	
Mrk 1018	$1.933^{+0.012}_{-0.010}$	$1.7^{+0.6}_{-0.7}$	$2.97^{+0.11}_{-0.26}$	$2.8^{+17.2}_{-1.3}$	> 0.34	> 70	(2.620)	711/707
	1.914 ± 0.024			5 ± 4			(1.689)	

6.6 Model II: Relxillp - Residuals

Residuals largely resemble those of Model I, with one exception. For the datasets of Fairall 9, 1h0419–577 and Mrk 509 we see a similar bump from 6 to 12 keV. In this range datapoints lie consistently above the model, but still within error range. Note that for these sources we found the highest reflection fractions in Model I. With Model II we gained intermediate reflection fractions, but the lowest lamppost heights of the sample. The excesses of these three sources are visible in EPICpn as well as FPM datasets, so we can rule out detector effects like pileup.

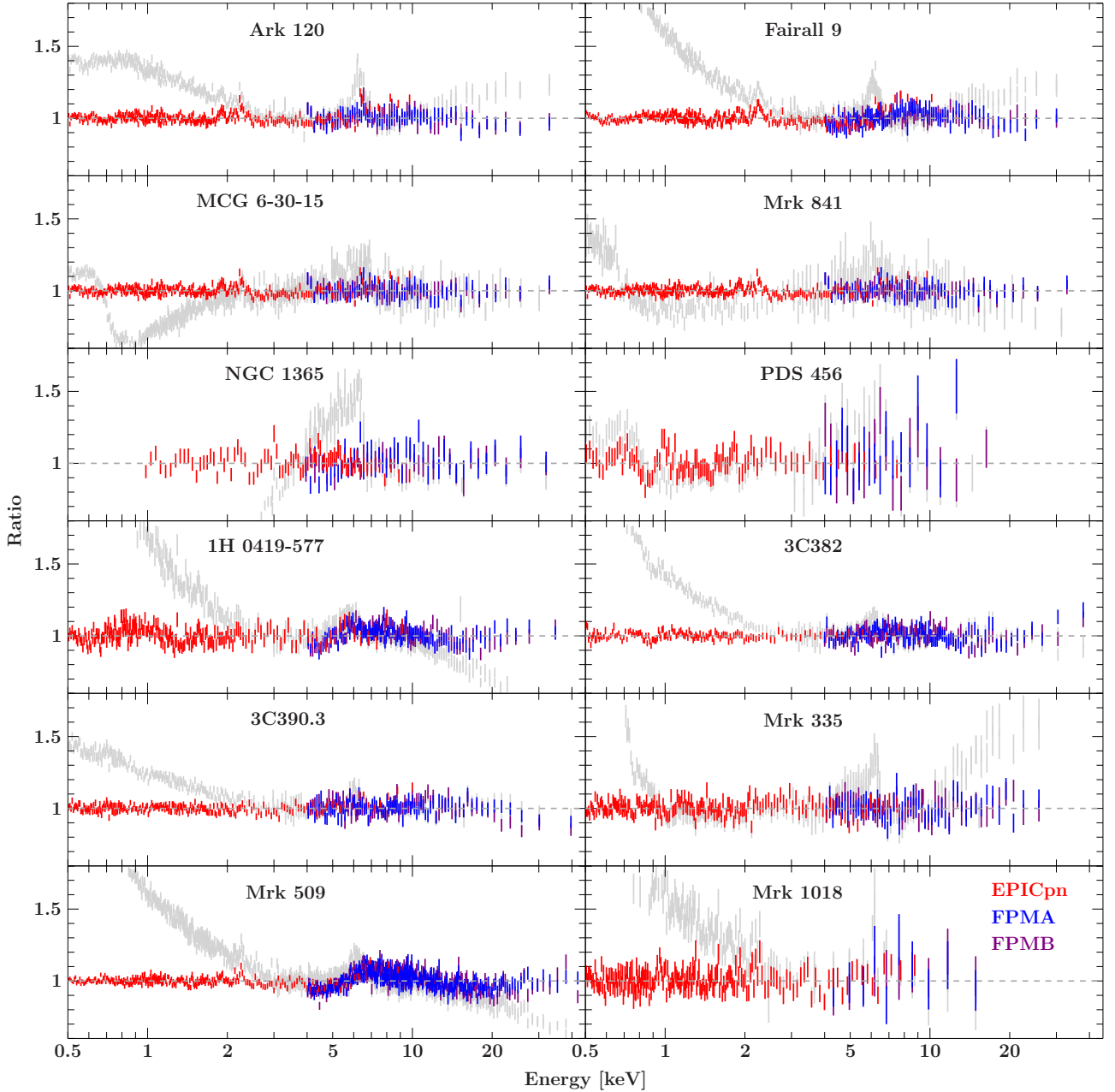


Figure 36: Residuals of the Relxillp model fits according to table 9. In the background the power law residuals from Fig. 33 are shown for comparison. Binning is increased for readability.

6.7 Model III: Relxillp (self-consistent) - Residuals

Residuals are very similar to those of Model II. Again, we observe the 6-12 keV excess in the residuals of Fairall 9, 1h0419-577 and Mrk 509.

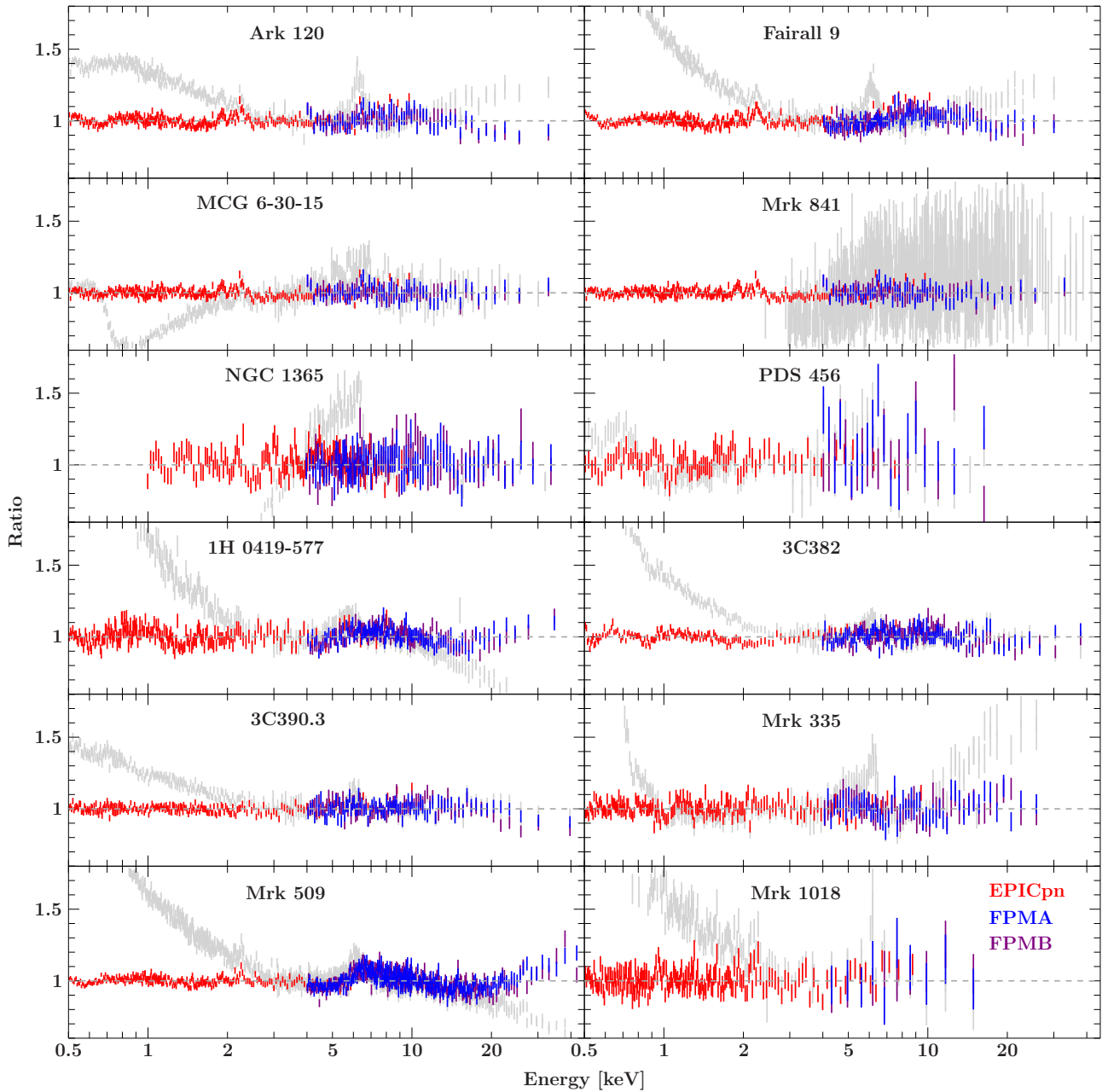


Figure 37: Residuals of the self-consistent lamppost fits according to table 9. In the background the power law residuals from Fig. 33 are shown for comparison. Binning is increased for readability.

6.8 Spectral component decomposition

In panels 38 and 39 we present individual model components according to the best fit parameters of Model II. Generally we show the primary power law component, CDR and RR and the sum of all emission components. Where required, we also show an absorbed and an unabsorbed version of the summed emission. Spectra share the same flux and energy scales.

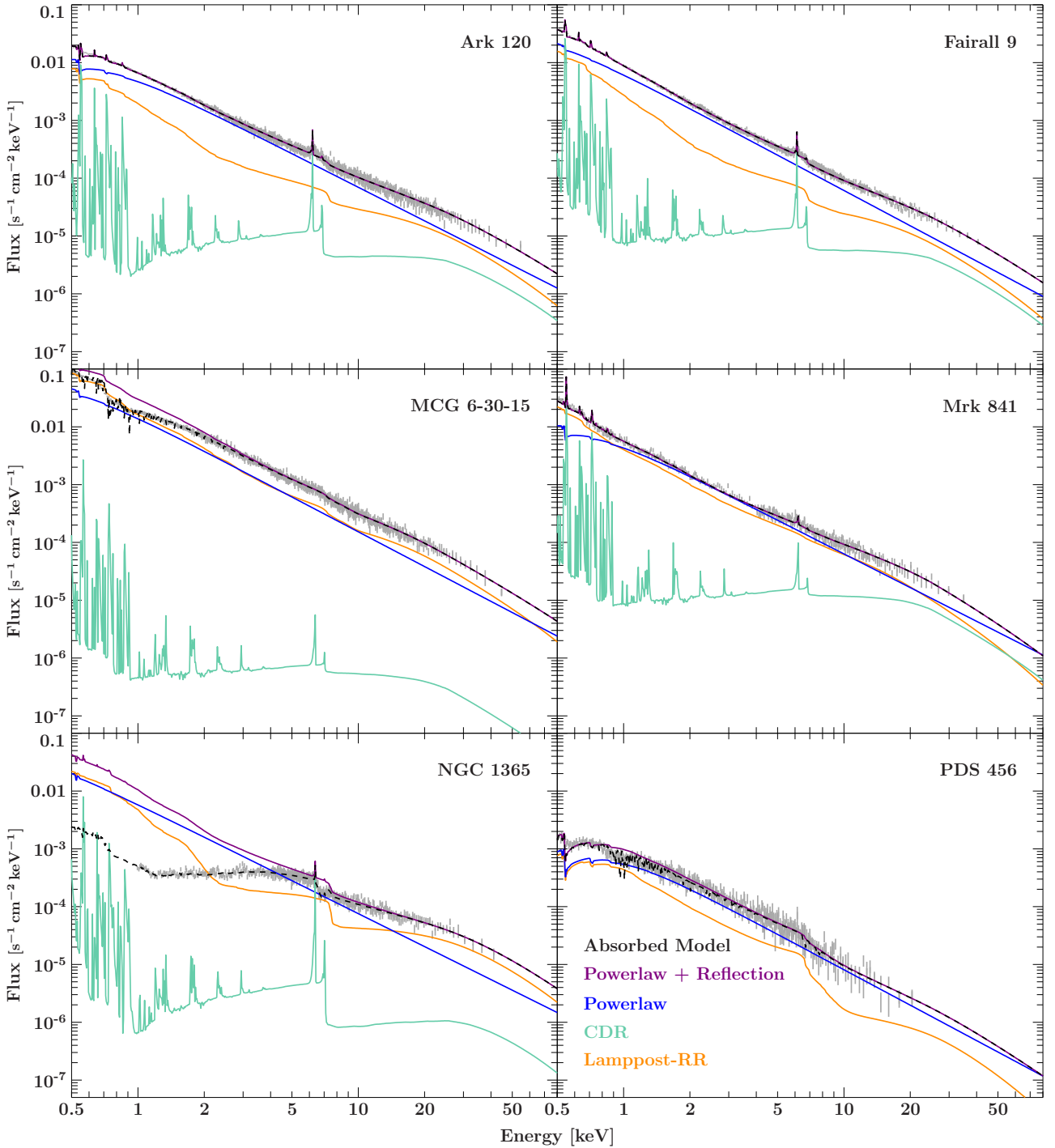


Figure 38: Model components according to Model II best fits with power law, Relativistic (RR) and Cold Distant Reflection (CDR). We also view the summed emission (purple) and the complete models (black) including absorption. Unfolded data in the background.

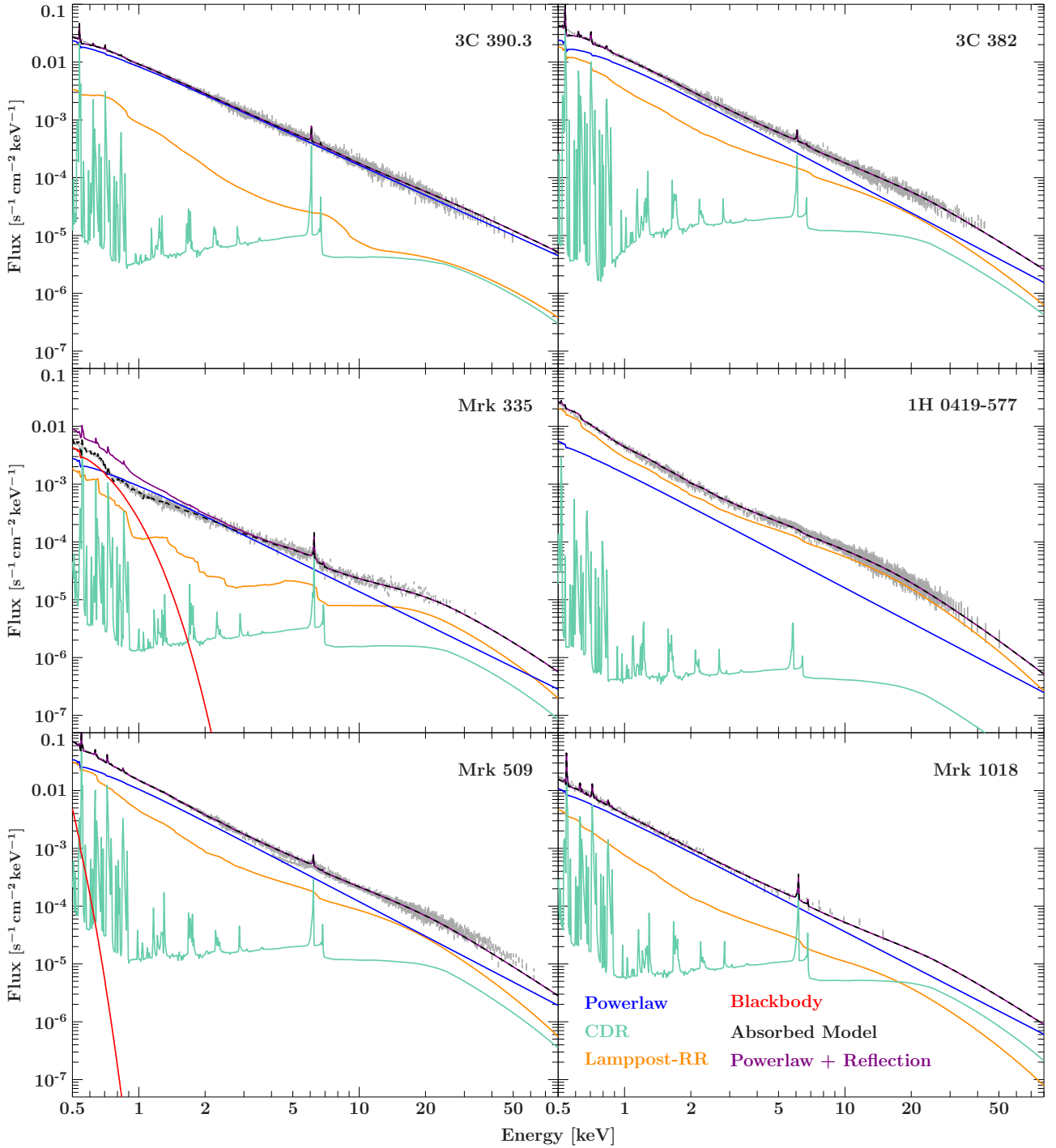


Figure 39: Model components according to Model II best fits with power law, Relativistic (RR) and Cold Distant Reflection (CDR). We also view the summed emission (purple) and the complete models (black) including absorption. Unfolded data in the background. The FPM data are scaled by a factor of $E^{\Gamma_1 - \Gamma_2}$ to correct the change of power law slope.

For most sources, the flux of the relativistic reflection surpasses that of the distant reflection by magnitudes of order and lies below the primary power law continuum. For individual cases, we see the flux of the relativistic Compton hump surpassing the primary spectrum, this can be explained by a redistribution of spectral energy. Also, the effect of relativistic light bending on low height sources plays a role in these sources. As downward emission is preferred, a higher flux hits the surface of the accretion disk and gets reflected rather than directly escaping.

6.9 Individual source results

Ark 120: Applying a broad range of reflection models we find that the lamppost models satisfyingly reproduce the emissivity profile based Model I. Nevertheless, for a perfect fit we require a small additional component that might result from an ionization gradient of the illuminated disk or from an extended, low-luminosity part of the lamppost source. We find intermediate inclinations close to those of Nardini et al. (2011) and Walton et al. (2013). While Nardini was unable to constrain the spin, Walton (2013) found an intermediate value of 0.6 and we find spins larger than 0.9 independently of the model.

Fairall 9: In the existing literature (Schmoll et al., 2009; Lohfink et al., 2012; Walton et al., 2013) on *Suzaku* and *XMM-Newton* data no consensus on inclinations and spin parameters can be found. Our measurements most closely resemble those of Walton (2013). While the self-consistent lamppost model finds consistent parameters with the emissivity profile, it produces a significantly worse statistic yet not enough to rule out the lamppost. The consistency of all parameters suggests that the lamppost model basically fits, but might have to be modified to include an extended radiation source.

PDS 456: We find a significant relativistic reflection component, but no signs of a narrow iron line. This requires the distant reflection to be completely outshined by the inner disk, or the outer parts to be obscured from view as might be caused by the present outflow. We are not able to constrain the self-consistent lamppost model, but the model with independent reflection fraction yields parameters consistent to the emissivity profile model. In the the χ^2 -landscape, we see two local minima for the ionization, one at neutral and one at high ionization. Given that we do not even see a cold reflection component or thin iron line, we deem the low ionization minimum not physically reasonable and restrict our fits to higher ionizations. The self-consistent model finds a very high radiation source compared to the free model. This indicates that lower intensity hits the disk than expected in an unobscured lamppost setup. Note that we find similarly extreme values for iron abundance and inclination as Walton et al. (2013), but they have kept the low ionization solution.

NGC 1365: The self-consistent fit yields the best statistics and is consistent to the emissivity profile fit. Considering the high inclination, the observed variable obscuration can be plausibly explained by a sightline along the edge of a filamented torus. Our measurement is also strikingly consistent with that of Risaliti et al. (2013), who found $a > 0.84$, $i = 60_{-20}^{+3}$ and $\Gamma = 1.92_{-0.26}^{+0.04}$ on the same dataset. The parameters of Walton et al. (2014) lie in the same range, however both did not measure a lamppost height.

MCG–6-30-15: Using the lamppost models we find one of the highest source heights of the sample. While we are unable to reliably constrain the spin parameter in lamppost geometry, all other reflection parameters stay consistent with the RELXILL fit. Photon index, spin and inclination agree with the Marinucci et al. (2014b) study of the same dataset. Our ionization parameter is slightly higher, but Marinucci (2014b) found ionization in this source to be variable.

Mrk 841: Apart from spin and lamppost height, parameters are consistent for all three models. In Lamppost geometry we find lower and worse constrained spins. The self-consistent model gives the closer constraints and a lower lamppost value.

3C 382: We find the emissivity profile to perfectly agree in parameters and fit statistics with a free reflection fraction lamppost, while the self-consistent model can not be constrained at all. The source height is found to be unlikely low at $< 1.02 r_{\text{EH}}$ indicating that the lamppost model might mimic a different geometry like a spherical region around the event horizon.

3C 390.3: The component decomposition (Fig. 38) shows that the best fit relativistic reflection component is compared to other sources less luminous by a factor of 10 and thus the least significant in the whole sample. The unreasonably high inclination found for the lamppost model also indicates that the fit might only reproduce non-relativistic reflection. The inclination found with the emissivity profile fit however agrees with the Giovannini et al. (2001) radio measurement.

Mrk 335: Apart from iron abundance, parameters stay consistent between different models, with the lamppost models giving better fits than the emissivity profile. In the self-consistent model, the lamppost heights do not vary between the two observations separated by 4 years, although photon indices change significantly. The hydrogen absorption column stays consistent for all three models at $1.11_{-0.21}^{+0.30} \times 10^{22}$ for Model II and $1.20_{-0.30}^{+0.17} \times 10^{22}$ for Model III. Parker et al. (2014) already fitted the RELXILLP model to the *NuSTAR* dataset only and found a higher source height of $h = 3.1 \pm 0.4 r_g$. While our spin agrees with that of Walton (2013) but not Parker, no general consistency of the other physical parameters can be seen between the three studies.

1H 0419-755: Model I perfectly fits the data, but is not completely matched by the lamppost models at a margin comparable to the results on Fairall 9 and Ark 120. Assuming the lampposts as valid anyway, we would find a slight change in spectral slope and a lamppost height increasing from 1.1 to 1.5 r_{EH} between the *XMM-Newton* and *NuSTAR* observation. However, we have to be careful interpreting this spectrum as the high reflection fraction and the spectrum decomposition show that the intensity of the reflected radiation would be significantly higher than the primary radiation. This might either hint at a source deep inside the relativistic region, or some obscuration of the primary but not the reflected emission. Another explanation would be a concave or conical inner accretion disk surface focusing reflected radiation.

Mrk 509: While Model I fits the data well, in lamppost geometry we find a significantly worse fit and very low lamppost heights. Examining residuals, we find an unfitted excess between 6 and 10 keV. Inclinations, ionization parameters and photon indices are inconsistent between models, so we argue that either we are missing some spectral component, or the lamppost model is insufficient to describe this source. The black-body component however stays significant at temperatures of $0.0292^{+0.0007}_{-0.0006}$ keV for Model II and $0.0119^{+0.0002}_{-0.0019}$ keV for Model III.

Mrk 1018: Parameters are not generally consistent between models although we find flat residuals. Being the source with the worst statistics, we would require higher S/N and spectral range to put meaningful constraints on spin and inclination.

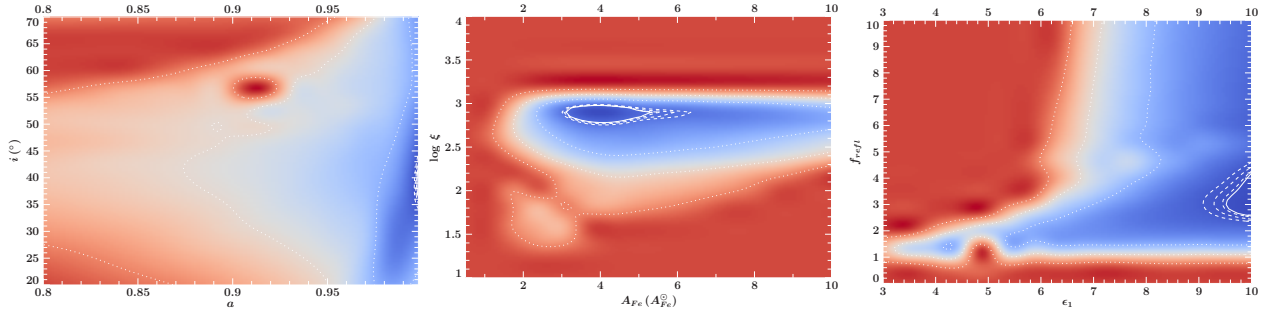
6.10 χ^2 -Landscapes

To find parameter degeneracies, we calculate 2-dimensional χ^2 -contour maps for all physical parameters, shown in Figs. 49 - 58 of the appendix. If two parameters are statistically independent, we expect the joint confidence contours to be elliptical with its axes parallel to the parameter axes. To map these contours we are stepping through the complete parameter space of two parameters. The parameter pair is fixed at each point and the remaining parameters refitted and the best-fit χ^2 calculated. In the visualization colours run from blue (low χ^2) to red (high χ^2). Maps are normalized to a lowest χ^2 of 0, while the contours indicate heights of $\chi^2 = 4.61, 5.99, 9.21$ and 13.8 corresponding to the two parameter confidence intervals of 90%, 95%, 99% and 99.9% (see Sec. 4.2). The drawn line indicates the 90% confidence, dashed lines up to 99.9% contours.

The upper panels show contours for the RELXILL-models while the the lower panels show contours for the free reflection fraction RELXILLP model. The rightmost panels contain the reflection parameters which are inherently different for both models and can not be compared directly. For the time-separate models also contours of both photon indices for *XMM-Newton* and *NuSTAR* spectra are included. In this section we only show a selection of noteworthy contours, for the full sample see the appendix.

Throughout the sample, parameter degeneracies only occur in singular cases. More frequently (compare Figs. 40, 41 and 42), we find several local minima in $\log \xi - A_{\text{Fe}}$ -space but generally these lie close together, so the choice of minimum has no significant impact on the behaviour of other parameters. Note that although on some χ^2 -maps the A_{Fe} contours run of the lower edge of the map, for the sample fit we used a wider parameter space and could generally find a lower boundary. We also see that in cases, where individual parameters can not be constrained at all (as was several times the case for spin) this does not have an impact on the constrainability of other parameters. In some cases, i.e. Fig 40, we see degeneracy between the lamppost height and reflection fraction. This can be physically expected as a change in lamppost height mainly changes the intensity of the reflected continuum. In the self-consistent lamppost model, this problem is resolved as the reflection fraction is no fitted parameter anymore. The separated photon indices of the last four sources are generally well constrained, except for Mrk 1018.

Ark 120: Model I



Model II

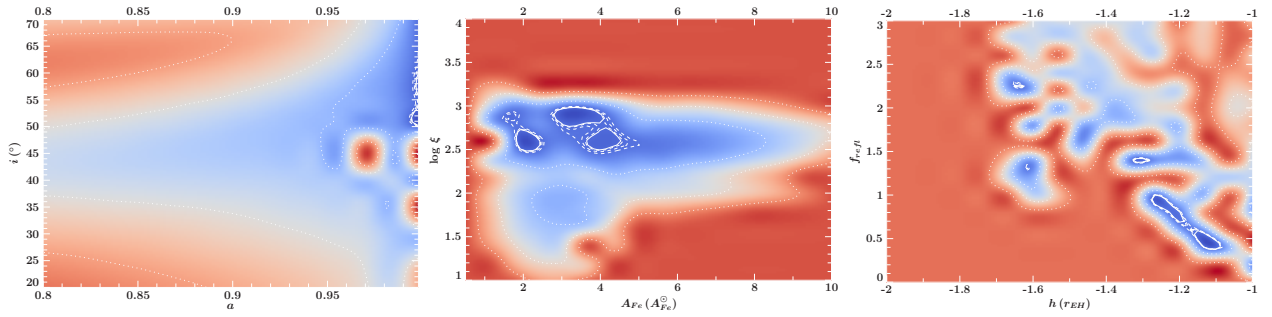
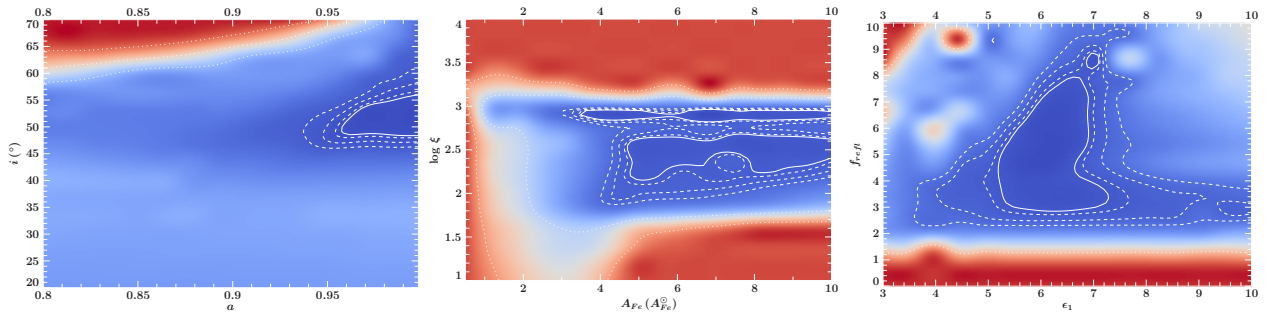


Figure 40: The spin parameter is constrained close to the upper limit. While the lamppost height shows some degeneracy with the reflection fraction, it can still be constrained to less than $1.4 r_{\text{EH}}$. We see three local minima in the $\log \xi - A_{\text{Fe}}$ combination, but in close proximity to each other.

NGC 1365: Model I



NGC 1365: Model II

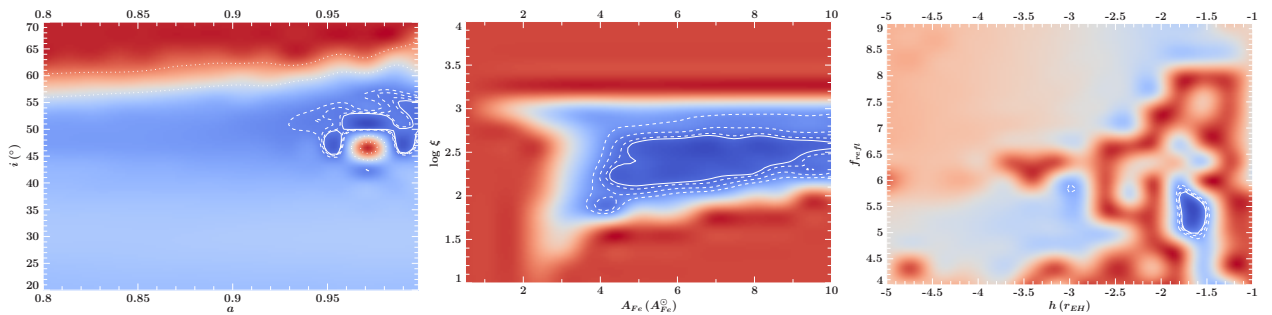
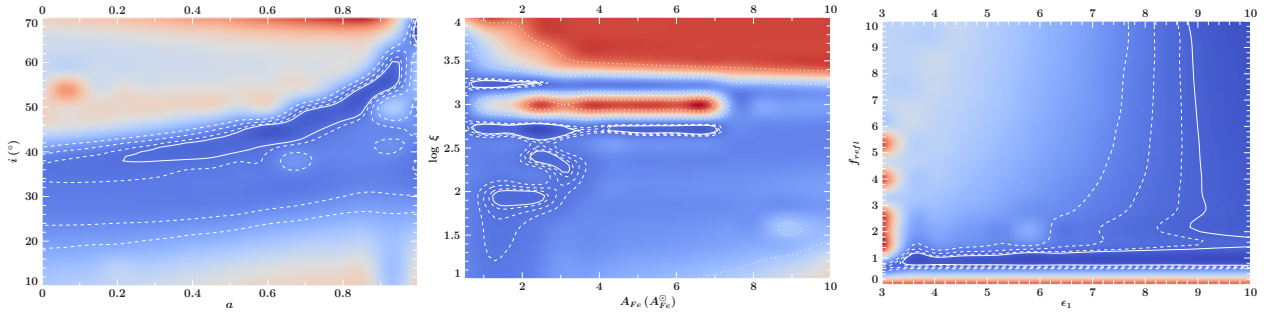
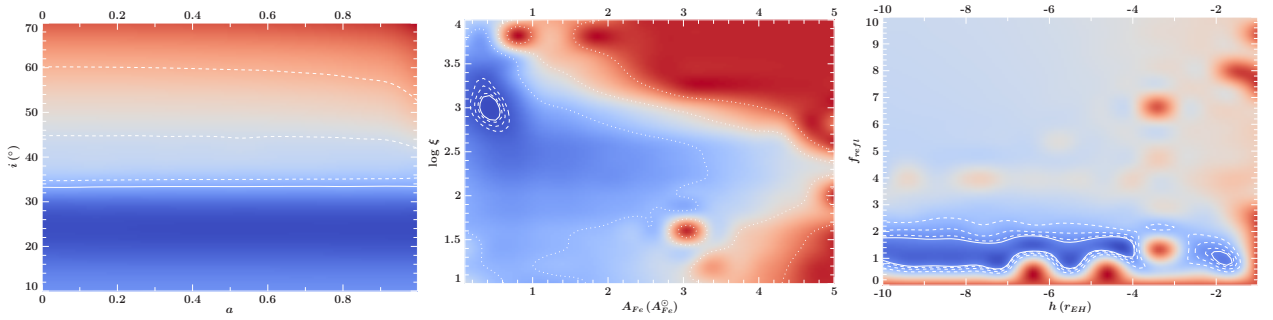


Figure 41: The contours are well constrained and consistent for both models. Constraints on lamppost parameters are closer than for the emissivity profile.

Figure 42: MCG 6-30-15
Model I

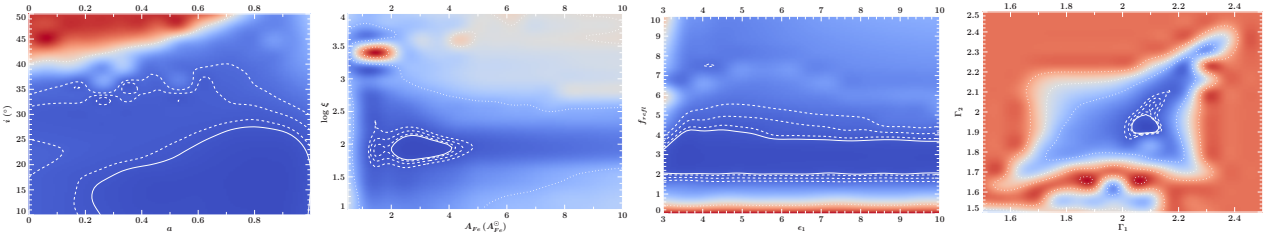


Model II



Going from Model II to Model III, a multitude of local minima in $\log \xi$, A_{Fe} and f_{ref} is resolved to a global minimum, but spin gets unconstrainable. The lamppost height finds a very large confidence interval.

Mrk 335: Model I



Mrk 335: Model II

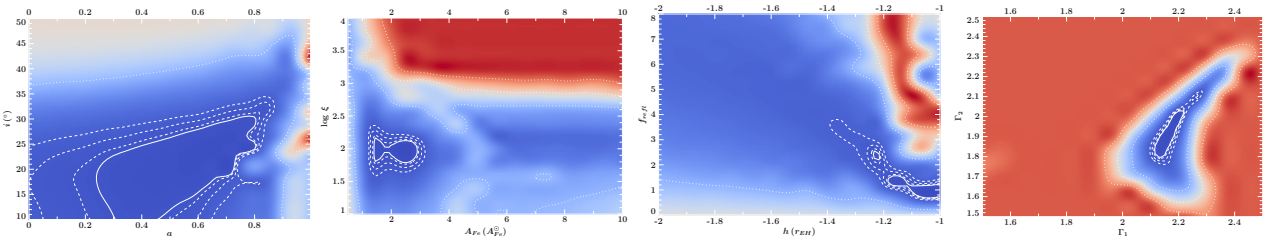


Figure 43: Contours are very consistent. Spin and reflection parameters get slightly better constraints in Model II. Where the emissivity profile can not be constrained at all, we can put close constraints on the lamppost source of Model II

6.11 Cross Validation of Simultaneous Observations

As we found some discrepancies of flux calibrations in Sec. 5.4, we take a more detailed look at cross calibration matters, comparing our results to the work of A. Gokus (2016) (priv. comm.) who determined cross calibration constants for a range of simultaneous *XMM-Newton* and *NuSTAR* observations. This way, we can estimate the impact of data extraction techniques on our final results. We have to note two main differences in the following determination of cross calibration constants. Gokus extracted spectra only for time ranges where *XMM-Newton* and *NuSTAR* were indeed simultaneously observing, taking *NuSTAR*'s observation gaps into account. This work uses light-curve selected intervals of constant flux where Gokus averaged across the complete observing time of the datasets. However, we extract the full time ranges of EPICpn data inside our selected time windows (compare Sec. 5.3). We also have to consider the models used, as we have seen that a simplified power law is not sufficient to give sample-wide consistent values of cross calibration. Gokus achieved this by examining semi-physical models similar to ours applied to the overlapping range of 3-10 keV. The models are given in Table 11. For comparison we re-evaluate our according best fits of Model I (Table 8). We fix reflection parameters and refit photon index and all norm parameters to the EPICpn and FPM datasets separately and in the same spectral range.

Table 11: Models used by the different cross calibrations in comparison

Study	Model	Analysis site
Gokus	tbnew*(powerlaw + relxill + zgauss)	XSPEC
This work	tbnew*(powerlaw + relxill + xillver)	ISIS & Isisscripts

Applying similar models to a sample of 10 simultaneously observed sources, Gokus found that power law indices measured by the FPM are consistently steeper than those measured with EPICpn at a difference of $\Delta\Gamma = 0.13 \pm 0.05$. A comparison of the overlap of both samples, consisting of Ark 120, Fairall 9 and MCG-6-30-15 is shown in Table 12.

Table 12: Cross calibration parameters in comparison

Source	Study	Γ_{EPN}	Γ_{FPM}	$\Delta\Gamma$	$N_{\text{FPMA}}/N_{\text{EPN}}$	$N_{\text{FPMB}}/N_{\text{EPN}}$
Ark 120	Gokus	1.63 ± 0.07	1.75 ± 0.08	0.12 ± 0.01	1.00 ± 0.07	1.00 ± 0.07
	This work	1.82 ± 0.03	1.93 ± 0.03	0.12 ± 0.01	$1.05^{+0.02}_{-0.03}$	$1.07^{+0.02}_{-0.03}$
Fairall 9	Gokus	1.84 ± 0.03	1.95 ± 0.022	0.11 ± 0.01	1.06 ± 0.04	1.13 ± 0.07
	This work	1.96 ± 0.07	2.08 ± 0.08	0.12 ± 0.01	$0.993^{+0.021}_{-0.022}$	$1.017^{+0.022}_{-0.023}$
MCG-6-30-15	Gokus	1.76 ± 0.10	1.92 ± 0.11	0.16 ± 0.01	1.03 ± 0.08	1.07 ± 0.08
	This work	1.97 ± 0.03	1.79 ± 0.04	-0.18 ± 0.01	$0.79^{+0.04}_{-0.02}$	$0.80^{+0.04}_{-0.02}$

We see that for Fairall 9 and Ark 120 Flux calibration agree within margin of error. Photon indices deviate slightly, but this can be explained by the different used models. The missing cold reflection component in Gokus model leads to the Compton hump being compensated by a flatter power law index. More conclusively the deviations in power law slope are consistent between both studies, and also agree with our first power law calibration in Table 3.

The comparison of MCG-6-30-15 seems more problematic. We have to keep in mind that this observation had long exposure at strong source variability and that both studies extracted different time windows. In Sec. 5.3.2 we have seen, that spectral hardness is fluctuating on small time scales. The time intervals that were observed by *XMM-Newton* but not *NuSTAR* might be enough to separate power law indices significantly, when a strong peak in hardness ratio is missed by the FPM observation.

Originally we assumed consistent photon indices in our modelling of simultaneous observations. Having seen that there is a systematic offset in power law slopes between FPM and EPICpn calibrations, we want to examine the impact of this effect on the physical results of our sample study. If indeed *NuSTAR* is measuring steeper spectra, this might lead to us underestimating the Compton hump in the high energy spectral range. Accordingly, we would measure lower reflection fractions respectively higher lamppost heights. To estimate this effect, we re-examine the results of Model III (self-consistent lamppost) applied to the spectrum of Ark 120. Therefore we compare three scenarios:

- **Tied:** The original Model III, with the same power law fitted to *XMM-Newton* and *NuSTAR* data only modified by a multiplicative detector constant.
- **Untied:** The same model with separate photon indices for both data sets, but the rest of the physical parameters tied together.
- **Offset:** The model with one photon index free to vary and the second one with a fixed offset relative to the first one, where we use the offset given in Table 12.

Table 13: Fit results for different methods of accounting for photon index cross calibration.

Ark 120	Γ	A_{Fe} (A_{Fe}^{\odot})	$\log \xi$	h (r_{EH})	a	i ($^{\circ}$)	f_{refl}	χ^2/N_{dof}
Tied	$1.904^{+0.008}_{-0.006}$	$2.95^{+0.11}_{-0.18}$	2.751 ± 0.016	$3.36^{+0.09}_{-0.16}$	$0.994^{+0.003}_{-0.004}$	$40.1^{+1.9}_{-1.6}$	(2.525)	3098/2605
Untied	$1.904^{+0.017}_{-0.018}$	$2.56^{+0.15}_{-0.20}$	$2.770^{+0.026}_{-0.019}$	$3.10^{+0.12}_{-0.11}$	$0.9936^{+0.0029}_{-0.0041}$	$41.4^{+1.6}_{-1.8}$	(2.735)	3054/2605
Offset	$1.881^{+0.006}_{-0.005}$ $1.984^{+0.006}_{-0.007}$ (1.874)	$2.43^{+0.13}_{-0.17}$	2.745 ± 0.010	$2.92^{+0.09}_{-0.06}$	$0.9926^{+0.0023}_{-0.0034}$	$43.6^{+1.2}_{-1.4}$	(2.876)	3123/2605

Looking at the results in Table 13, we see that the effect is indeed visible, yet not dramatic. Untied power law parameters converge to values close to those of tied power law model and the offset model is the statistically least significant. Apart from lamppost height and reflection fraction, physical parameters stay consistent. We conclude that the cross calibration issues do not have a significant impact on the general conclusions of this work. There is, as argued above, a small but significant deviation in reflection fraction. We estimate a systematic error leading to lamppost heights that could be smaller than the measured values by $15 \pm 5\%$. Note, that this effect only applies to simultaneous observations. In the right panel of Fig. 44 we see power law indices as determined from the cross-calibration (Sec. 5.4) and from the best-fit physical models of simultaneous observations. We see that the physical model yields vastly better agreement in its photon indices than the simple power law fit, and that when fitting the physical model across the full spectral range, power law parameters between FPM and EPICpn generally agree.

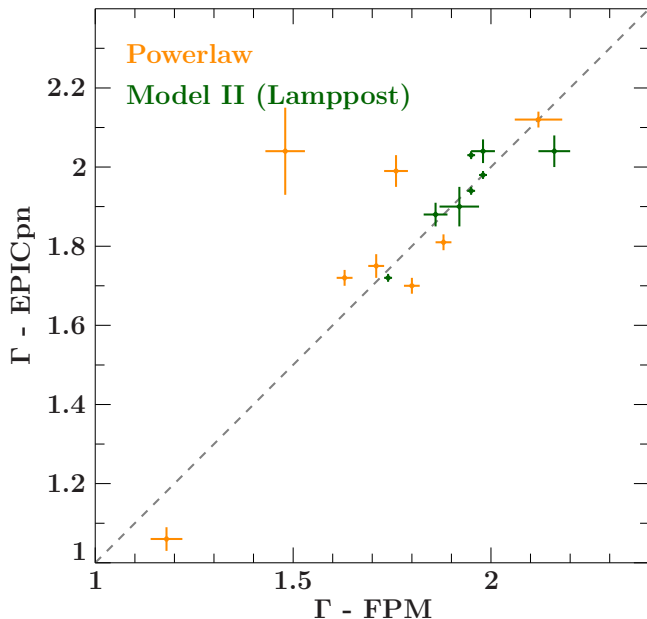


Figure 44: Best fit photon indices for the eight sources where simultaneous fits are possible. For Model II, in the best fit models of Table 9 photon indices were untied between FPM and EPICpn and all norm parameters refitted.

7 Sample discussion

Throughout the whole sample, the inner emissivity profiles observed with Model I are very steep. According to Dauser (2014) this implies a lamppost source at very small height, matched by the fit results of source heights at only several event horizon radii. Across all models and sources, we find spin parameters to be constrained to values very close to the physically possible maximum. This observational bias has been reported previously (see, e.g., Brenneman et al., 2011; Reynolds et al., 2012; Walton et al., 2013). There are several effects that explain this preference for observing high spins. First of all it is expected that rapidly rotating black holes show a higher accretion efficiency and are therefore easier to detect (Thorne, 1974; Vasudevan et al., 2016). Moreover detecting slowly rotating black holes is much harder, as strong relativistic broadening is only expected for large spin and compact primary sources (Dauser, 2014). Additionally, the maximal observed reflection strength for slowly rotating black holes is much lower than for high spin (see, e.g., Dauser et al., 2016). In the latter case the reflection spectrum can easily exceed the observed primary radiation due to general relativistic effects (see also Fig. 38). A similar observation bias might also be responsible for the detection of source heights close to the event horizons, as only from these sources we expect obvious relativistic broadening (Fabian et al., 2015).

7.1 Parameter correlations

In Fig. 45 we show all measured reflection fractions and lamppost heights, distinguished by model. Source heights fall in the same range as the values determined by Emmanoulopoulos et al. (2014) via reverberation mapping. Obviously, our ability to constrain lamppost heights strongly depends on the source height. It can be seen as strong support for the model that all measured parameter pairs lie in the theoretically allowed area. In this plot we see that the measured values fall into two groups: One of reflection fractions close to the maximum value, and one with lamppost heights close to the event horizon. The latter group is only present in Model II and shows unphysical combinations of low height and low reflection fraction. Also we find the majority of sources at unlikely low heights. As Model III constrains the reflection fraction to an idealized theoretical value it yields much more physical results while still giving acceptable fits. Generally we can put better constraints on the source heights and find physically reasonable values. We see that degeneracies that lead partly to unphysical solutions are removed. Still, the remaining group that already found realistic values using Model II does not change much.

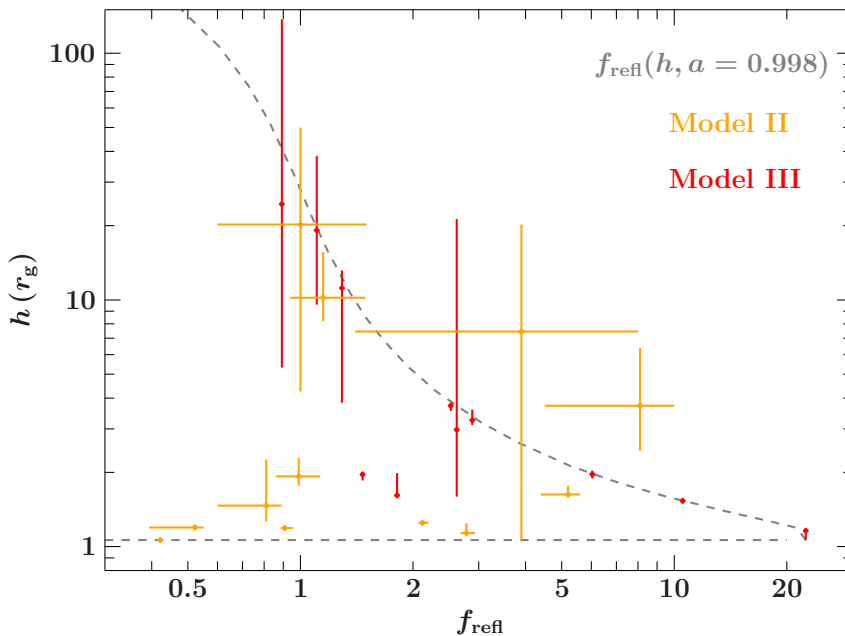


Figure 45: Measured lamppost height and reflection fraction parameters with errors for Models II and III. The dashed lines indicate the size of the event horizon and the theoretical maximum of the reflection fraction, both for maximum spin.

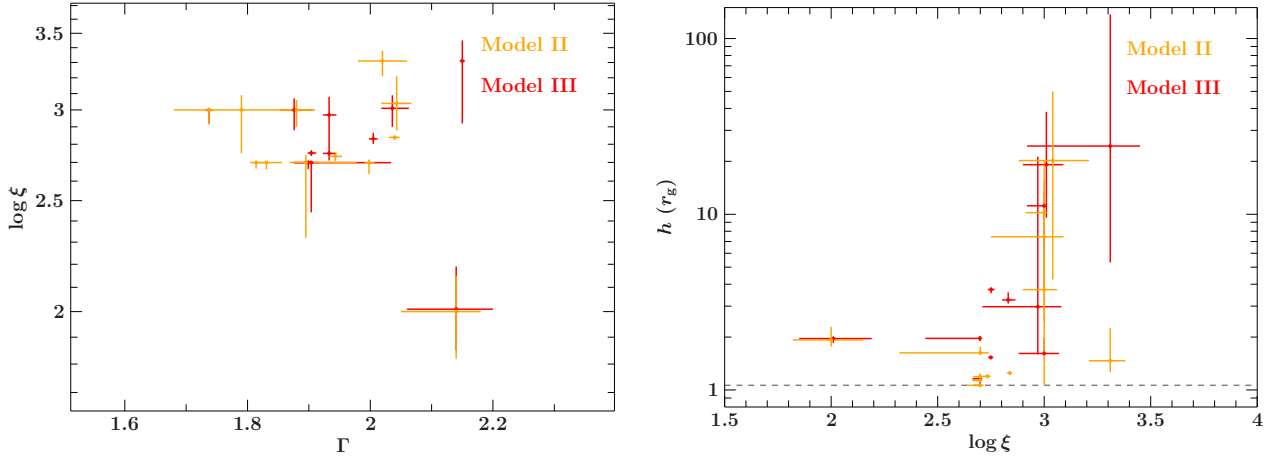


Figure 46: Parameter values for power law indices, ionization parameters and lamppost height. A clustering around the parameter values of $\Gamma \sim 2$ and $\log \xi \sim 3$ is visible for both models.

Inclinations and iron abundances are scattered randomly throughout the sample and show no obvious correlations to other parameters. The values we find for ionization at the inner accretion disk edge are clustering around $\log \xi = 2.7 \pm 0.3$ as can be observed in Fig. 46. It can be argued that this is another selection effect: Only accretion systems with high energy dissipation can be observed at all, this implies a preference for observing higher temperature accretion disks. From the higher ionization side, we are again constrained by the selection criterion of visually distinguished iron lines. A fully ionized accretion disk would forbid the existence of such a line. These two observation biases constrain the observed ionization parameters to the intermediate range. Ignoring the outlier at $\log \xi = 2$, we see slight correlations of $\log \xi \propto \Gamma$ and $\log h \propto \log \xi$.

7.2 Comparison to the Walton (2013) sample

Our study generally finds harder power laws than the study of (Walton et al., 2013) as can be seen in Fig. 47. This is a direct result of the inclusion of *NuSTAR* data and the according extension of the energy range. Their PIN/XIS spectra extend up to maximally 20 keV, albeit at very low signal-to-noise, so he systematically underestimates the extent of the Compton hump. Including this region, we find a strong spectral curvature that is generally better explained by a harder power law spectra, and stronger soft reflection components. This observation is confirmed by the behaviour of the ionization parameter. Walton already found that across his sample ionization parameters are strongly clustered around a value of $\log \xi = 2.2$. As pointed out above, we see a similar clustering, but at a significantly higher value of $\log \xi = 2.7$. The systematic increase in $\log \xi$ and decrease in photon indices is needed to model the strong spectral curvatures of our broad band spectra (compare Fig. 33).

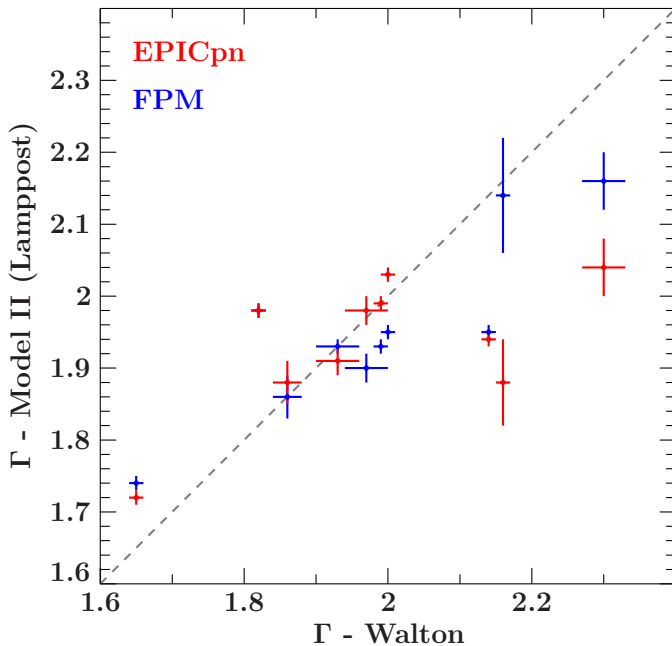


Figure 47: Photon indices measured for the whole sample in comparison to (Walton et al., 2013). The values for NGC 1365 and MCG-6-30-15 are not included as they were not part of the original Walton (2013) study. Indices of Model II have been initially tied between FPM and EPICpn. For the purposes of this comparison they have been separated and refitted together with all norm parameters.

We also compare the inclination and iron abundance parameters to those of Walton and between our three models in Fig 48. There is a visible tendency for measuring lower inclinations with the emissivity profile (Model I) than with the lamppost models. Where Walton (2013) found inclination values constrained to a close band of $30^\circ - 60^\circ$, we also find inclinations below 60° but more evenly distributed towards lower values - well consistent with an obscuring torus model. If the paradigm of an obscuring dust torus is true, we would expect to observe 'bare' AGN to be scattered randomly in a low inclination range, but to be blocked out at higher inclinations. The maximum inclination would be determined the typical vertical extent of the Torus. Note however, that this argument can only explain the trend and we can not qualitatively discuss the distribution of inclinations, as the features produced by varying inclination are also subject to observation bias. Accretion disks of extremely high inclination produce lines that might be too broad and low to observe at all. To discern these two limiting factors, we would require a larger sample and to take a deeper look at absorption phenomena. Comparing iron abundances, we see that these parameters are generally not consistent within statistical errors. Nevertheless, an overall correlation between the two samples is still visible. It can also be seen, that the lamppost model fits produce systematically lower iron abundances than the RELXILL emissivity profile fits.

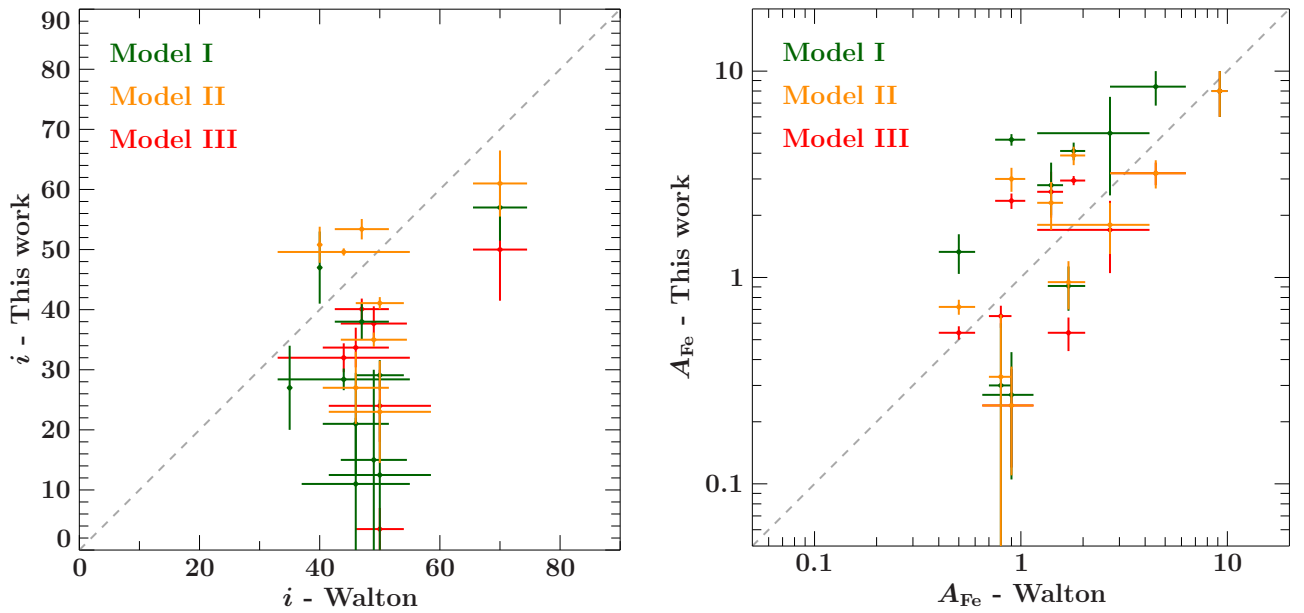


Figure 48: Left: Inclination parameters in comparison to those measured by Walton (2013) for all three models. Right: Analogous comparison of iron abundances.

8 Conclusions and Outlook

We conclude by collecting the most noteworthy results gained through the course of this thesis: Simultaneous fitting of *XMM-Newton* and *NuSTAR* data, taking into account a wide spectral range, allowed us to reliably put constraints on a complex physical model of relativistic reflection. We measured physically reasonable values that largely agree with literature. Seen that cross calibration issues remain, but their impact on measurements can be handled. From our simultaneous highest-resolution, lowest variability observations of Ark 120 and Fairall 9 we gained a deviation in photon indices between FPM and EPICpn of $\Delta\Gamma = 0.12 \pm 0.1$.

Where 11 AGN of our sample feature notable soft excesses, 9 of these can be explained by a combination of reflection and low column absorption. We emphasize that relativistic reflection is a powerful hypothesis to explain a wide range of soft excesses in unobscured AGN and also has to be factored in when the soft excess radiation is produced by other processes.

Already when using the emissivity profile model of relativistic reflection, we constrain every source's spin parameter close to the upper limit. It has been argued, that this preference is due to a strong observation bias. With the lamppost models, individual cases become unconstrainable. We are only able to constrain spin parameters of sources with very low lamppost heights and the uncertainties on source heights obviously grow with increasing height. We find inner emissivity profile indices to be constrained to very high values throughout the sample. Consistent to this, we find generally low source heights below $10 r_g$. Again, the preference for low heights might be observation bias.

A lamppost geometry model can reproduce all models fitted by an emissivity profile, but often at slightly worse χ^2 . We have to keep in mind that the fitted emissivity profiles do not generally have to be physically reasonable, and that there is also a possibility of further features like extended source geometries that are covered by the emissivity profile but not the lamppost model. The self-consistent lamppost model is well able to explain the data at comparable statistics to a free-normalization lamppost. Moreover, the self-consistent model produces physically more reasonable values by ruling out sources of low height and low reflection fraction. The model also is no longer affected by the degeneracy between reflection fraction and lamppost height.

We report lamppost height values at an average of $4 r_g$. To great agreement, Emmanoulopoulos et al. (2014) determined lamppost heights for 12 AGN from reverberation mapping and found a sample average of $3.7 r_g$, but we find individually more extreme values. They are gathered in Table 14. The three sources with highest reflection fractions and lowest lamppost height feature a bump in residuals between 6 and 12 keV. This might be a feature produced by extended emission that gets enhanced in low height sources.

Table 14: Reduced χ^2 for the fits of all three models at consistent binning and lamppost heights that could be measured self-consistent and significantly with 90% confidence intervals. Best fits highlighted in bold, entries in brackets signal problematic fits with unphysical or unconstrainable parameter values.

Source	Model I	Model II	Model III	Model III LP height (r_{EH})
Ark 120	1.10	1.14	1.19	$3.36^{+0.09}_{-0.16}$
Fairall 9	1.05	1.14	1.21	$2.89^{+0.30}_{-0.13}$
MCG 6-30-15	1.07	1.07	1.06	18^{+18}_{-9}
Mrk 841	1.08	1.12	1.12	< 1.23
NGC 1365	1.06	1.05	1.05	$1.85^{+0.06}_{-0.07}$
PDS 456	1.20	1.21	(1.12)	
1H 0419-577	1.01	1.13	1.11	$1.51^{+0.05}_{-0.08} / 1.090^{+0.016}_{-0.091}$
3C 382	1.04	1.04	(-)	
3C 390.3	1.06	(1.08)	(1.08)	
Mrk 335	1.07	1.06	1.08	$1.138^{+0.028}_{-0.063} / 1.17^{+0.09}_{-0.06}$
Mrk 509	1.13	(1.34)	(1.33)	
Mrk 1018	1.02	1.02	1.02	$2.8^{+17.2}_{-1.3} / 5 \pm 4$

Across the whole sample, we find slightly harder power law indices and a systematic increase in ionization parameters compared to the study of Walton et al. (2013). This is a result of the inclusion of high energy *NuSTAR* data. To model the observed Compton humps we need flatter power laws and compensate the lost soft flux via stronger reflection components. Although not agreeing for each source individually, the observed distributions of iron abundances and accretion disk inclination remain similar to those of Walton (2013). We only see accretion disk inclination angles below 60° . This observation agrees well with the paradigm that bare AGN are observed via sightlines above the obscuring torus.

This work can be built upon in several directions:

Extended sample: Our sample of twelve sources is only half as big as that of Walton, and only a small part of the known unobscured AGN. With a growing database of *NuSTAR* observations, performing a systematic analysis of a larger sample of high quality data, we could determine whether the trends observed in Sec. 7 are statistically significant.

Improved cross calibration: The *NuSTAR* calibration team is constantly working on the cross calibration issues discussed in Sec. 6.11. The calibration uncertainties are a further factor of complication considering the already complex parameter space of the physical model. If the upcoming releases of the *NuSTAR* calibration database improve upon these problems, we might be able to better constrain our sources of lower data quality.

Refined reflection models: Implementations of an extended lamppost source model, and of a multiple ionization zone accretion disk model are being worked on by T. Dauser (priv. comm.). An application of these models might resolve the remaining residuals of the lamppost model and yield further insight on the connections between accretion and X-ray emission.

Time-resolved analysis: We have seen variability in several sources. A time-resolved analysis might give results on whether source heights contribute to this variability, and whether there is any connection to flaring behaviour of the accretion disk. At the time of writing, variability of the lamppost geometry is largely unexplored territory and might yield great insight on the nature of the radiation source.

9 Bibliography

- 2016, XMM-Newton Users Handbook, ESA: XMM-Newton SOC, 2.14 edition
- Abramowicz M., Jaroszynski M., Sikora M., 1978 63, 221
- An H., Kaspi V.M., Archibald R., et al., 2014, *Astronomische Nachrichten* 335, 280
- Andrae R., 2010, arXiv e-prints
- Andrae R., Schulze-Hartung T., Melchior P., 2010, arXiv e-prints
- Antonucci R., 1993, *araa* 31, 473
- Ballantyne D.R., Bollenbacher J.M., Brenneman L.W., et al., 2014, *Astrophys. J.* 794, 62
- Ballantyne D.R., Vaughan S., Fabian A.C., 2003, *Mon. Not. R. Astron. Soc.* 342, 239
- Ballhausen R., 2015, *Master's thesis*, Friedrich Alexander-Universität Erlangen-Nürnberg
- Bardeen J.M., 1970, *Nature* 226, 64
- Bearden J.A., Burr A.F., 1967, *Rev. Mod. Phys.* 39, 125
- Bentz M.C., Denney K.D., Grier C.J., et al., 2013, *Astrophys. J.* 767, 149
- Best P.N., Heckman T.M., 2012, *Mon. Not. R. Astron. Soc.* 421, 1569
- Best P.N., Kauffmann G., Heckman T.M., et al., 2005, *Mon. Not. R. Astron. Soc.* 362, 25
- Beuchert T., 2013, *Master's thesis*, Friedrich Alexander-Universität Erlangen-Nürnberg
- Blandford R., Eichler D., 1987, *PhysRep* 154, 1
- Blumenthal G.R., Gould R.J., 1970, *Rev. Mod. Phys.* 42, 237
- Bondi H., 1952, *Mon. Not. R. Astron. Soc.* 112, 195
- Brenneman L., 2013, *Measuring the Angular Momentum of Supermassive Black Holes*
- Brenneman L.W., Reynolds C.S., 2006, *Astrophys. J.* 652, 1028
- Brenneman L.W., Reynolds C.S., Nowak M.A., et al., 2011, *Astrophys. J.* 736, 103
- Bromley B.C., Chen K., Miller W.A., 1997, *ApJ* 475, 57
- Chiaberge M., Gilli R., Lotz J.M., Norman C., 2015, *Astrophys. J.* 806, 147
- Comastri A., Setti G., Zamorani G., Hasinger G., 1995, *aap* 296, 1
- Dauser T., 2010, *Master's thesis*, Friedrich Alexander-Universität Erlangen-Nürnberg
- Dauser T., 2014, Ph.D. thesis, Friedrich Alexander-Universität Erlangen-Nürnberg
- Dauser T., García J., Walton D.J., et al., 2016 590, A76
- Dauser T., Garcia J., Wilms J., et al., 2013, *Mon. Not. R. Astron. Soc.* 430, 1694
- Dauser T., Svoboda J., Schartel N., et al., 2012, *Mon. Not. R. Astron. Soc.* 422, 1914
- Dauser T., Wilms J., Reynolds C.S., Brenneman L.W., 2010, *NMRAS* 409, 1534
- Davis J.E., 2001, *Astrophys. J.* 562, 575
- den Herder J.W., Brinkman A.C., Kahn S.M., et al., 2001, *AAP* 365, L7
- Di Gesu L., Costantini E., Piconcelli E., et al., 2014 563, A95
- Dickey J.M., Lockman F.J., 1990, *araa* 28, 215
- Done C., Davis S.W., Jin C., et al., 2012, *Mon. Not. R. Astron. Soc.* 420, 1848
- Dove J.B., Wilms J., Nowak M.A., et al., 1998, *Mon. Not. R. Astron. Soc.* 298, 729
- Dovčiak M., Done C., 2016, *Astronomische Nachrichten* 337, 441
- Dunlop J.S., McLure R.J., Kukula M.J., et al., 2003, *Mon. Not. R. Astron. Soc.* 340, 1095
- Einstein A., 1916, *Annalen der Physik* 354, 769
- Eisenberger P., Platzman P.M., 1970, *Phys. Rev. A* 2, 415
- Emmanoulopoulos D., Papadakis I.E., Dovčiak M., McHardy I.M., 2014, *Mon. Not. R. Astron. Soc.* 439, 3931
- Emmanoulopoulos D., Papadakis I.E., McHardy I.M., et al., 2011, *Mon. Not. R. Astron. Soc.* 415, 1895
- Fabian A.C., 2012, *araa* 50, 455
- Fabian A.C., Iwasawa K., Reynolds C.S., Young A.J., 2000, *Publ. Astron. Soc. Pac.* 112, 1145
- Fabian A.C., Lohfink A., Kara E., et al., 2015, *Mon. Not. R. Astron. Soc.* 451, 4375
- Fabian A.C., Miniutti G., Gallo L., et al., 2004, *Mon. Not. R. Astron. Soc.* 353, 1071
- Fabian A.C., Miniutti G., Iwasawa K., Ross R.R., 2005, *Mon. Not. R. Astron. Soc.* 361, 795
- Fabian A.C., Rees M.J., Stella L., White N.E., 1989, *Mon. Not. R. Astron. Soc.* 238, 729
- Fabian A.C., Vaughan S., 2003, *Mon. Not. R. Astron. Soc.* 340, L28
- Fabian A.C., Vaughan S., Nandra K., et al., 2002, *Mon. Not. R. Astron. Soc.* 335, L1
- Frank J., King A., Raine D.J., 2002, *Accretion Power in Astrophysics: Third Edition*
- Gallo L.C., Fabian A.C., Grupe D., et al., 2013, *Mon. Not. R. Astron. Soc.* 428, 1191
- García J., Dauser T., Lohfink A., et al., 2014, *ApJ* 782, 76
- García J., Dauser T., Reynolds C.S., et al., 2013, In: *AAS/High Energy Astrophysics Division*, Vol. 13. *AAS/High Energy Astrophysics Division*, p. 117.01
- García J., Kallman T.R., 2010, *Astrophys. J.* 718, 695
- George I.M., Fabian A.C., 1991, *MNRAS* 249, 352
- George I.M., Fabian A.C., Nandra K., et al., 1989, In: *Hunt J., Battrick B. (eds.) Two Topics in X-*

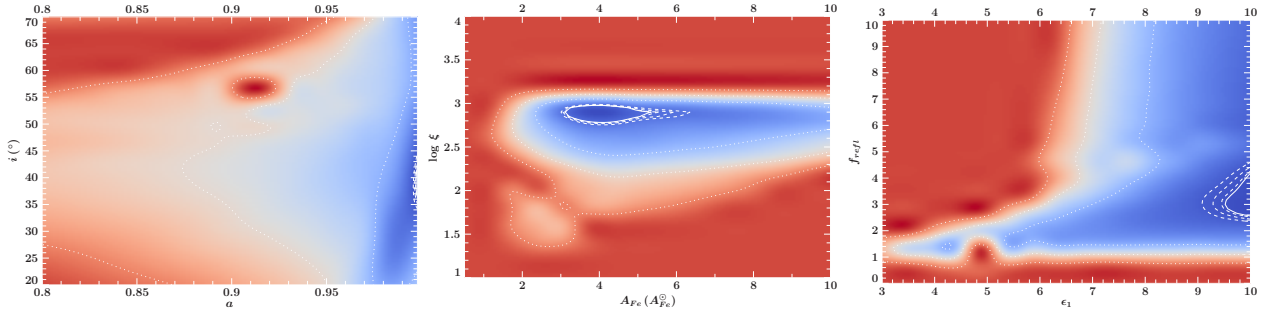
- Ray Astronomy, Volume 1: X Ray Binaries. Volume 2: AGN and the X Ray Background, Vol. 296. ESA Special Publication
- George I.M., Turner T.J., Netzer H., et al., 1998 114, 73
- Ghez A.M., Salim S., Weinberg N.N., et al., 2008, *Astrophys. J.* 689, 1044
- Giovannini G., Cotton W.D., Feretti L., et al., 2001, *Astrophys. J.* 552, 508
- Gofford J., Reeves J.N., Braito V., et al., 2014, *Astrophys. J.* 784, 77
- Gokus A., 2016, *Master's thesis*, Friedrich Alexander-Universität Erlangen-Nürnberg in preparation
- Gorenstein P., 2012, *Optical Engineering* 51, 011010
- Haardt F., Maraschi L., 1991, *Astrophys. J.* 380, L51
- Hanke M., 2007, *Master's thesis*, Friedrich Alexander-Universität Erlangen-Nürnberg
- Harrison C.M., Alexander D.M., Mullaney J.R., Swinbank A.M., 2014, *Mon. Not. R. Astron. Soc.* 441, 3306
- Harrison F.A., Craig W.W., Christensen F.E., et al., 2013, *ApJ* 770, 103
- Heitler W., 1954, *Quantum theory of radiation*
- Iwasawa K., Fabian A.C., Reynolds C.S., et al., 1996, *Mon. Not. R. Astron. Soc.* 282, 1038
- Jansen F., Lumb D., Altieri B., et al., 2001, *AAP* 365, L1
- Jones F.C., 1968, *Physical Review* 167, 1159
- Kadler M., Krauß F., Mannheim K., et al., 2016, *ArXiv e-prints*
- Kalberla P.M.W., Burton W.B., Hartmann D., et al., 2005, *aap* 440, 775
- Keck M.L., Brenneman L.W., Ballantyne D.R., et al., 2015, *Astrophys. J.* 806, 149
- Kerr R.P., 1963, *Physical Review Letters* 11, 237
- Kitaguchi T., Bhalerao V., Cook W.R., et al., 2014, In: *Space Telescopes and Instrumentation 2014: Ultraviolet to Gamma Ray*, Vol. 9144. *procspie*, p. 91441R
- Konigl A., Kartje J.F., 1994, *Astrophys. J.* 434, 446
- Kraus F., 2016, *Ph.D. thesis*, Friedrich Alexander-Universität Erlangen-Nürnberg
- Krauss F., 2013, *Master's thesis*, Friedrich Alexander-Universität Erlangen-Nürnberg
- Krolik J.H., 1999, *Active galactic nuclei : from the central black hole to the galactic environment*
- Krolik J.H., Kallman T.R., 1987, *ApJ* 320, L5
- Kuntz K.D., Snowden S.L., 2008 478, 575
- Lampton M., Margon B., Bowyer S., 1976, *Apj* 208, 177
- Laor A., 1991, *Astrophys. J.* 376, 90
- Levenberg K., 1944, *Quarterly of applied mathematics* 2, 164
- Lohfink A.M., Reynolds C.S., Miller J.M., et al., 2012, *Astrophys. J.* 758, 67
- Longinotti A.L., Costantini E., Petrucci P.O., et al., 2010 510, A92
- Lumb D.H., Scharfel N., Jansen F.A., 2012, *Optical Engineering* 51, 011009
- Lumb D.H., Warwick R.S., Page M., De Luca A., 2002 389, 93
- Madsen K.K., Harrison F.A., Markwardt C.B., et al., 2015, *apjs* 220, 8
- Magdziarz P., Zdziarski A.A., 1995, *Mon. Not. R. Astron. Soc.* 273, 837
- Marinucci A., Matt G., Kara E., et al., 2014a, *Mon. Not. R. Astron. Soc.* 440, 2347
- Marinucci A., Matt G., Miniutti G., et al., 2014b, *Astrophys. J.* 787, 83
- Marquardt D.W., 1963, *Journal of the society for Industrial and Applied Mathematics* 11, 431
- Martocchia A., Karas V., Matt G., 2000, *Mon. Not. R. Astron. Soc.* 312, 817
- Martocchia A., Matt G., 1996, *Mon. Not. R. Astron. Soc.* 282, L53
- Mason K.O., Breeveld A., Much R., et al., 2001, *AAP* 365, L36
- Matt G., Fabian A.C., Ross R.R., 1993, *Mon. Not. R. Astron. Soc.* 262, 179
- Matt G., Marinucci A., Guainazzi M., et al., 2014, *Mon. Not. R. Astron. Soc.* 439, 3016
- Matt G., Perola G.C., Piro L., Stella L., 1992 257, 63
- Mayer-Kuckuck T., 1985, *BG Teubner, Stuttgart*
- McClintock J.E., Shafee R., Narayan R., et al., 2006, *Astrophys. J.* 652, 518
- McHardy I.M., Stewart G.C., Edge A.C., et al., 1990, *Mon. Not. R. Astron. Soc.* 242, 215
- Mehdipour M., Branduardi-Raymont G., Kaastra J.S., et al., 2011 534, A39
- Miller J.M., Tomsick J.A., Bachetti M., et al., 2015, *Astrophys. J., Lett.* 799, L6
- Miller L., Turner T.J., Reeves J.N., 2008 483, 437
- Morales R., Fabian A.C., Reynolds C.S., 2000, *Mon. Not. R. Astron. Soc.* 315, 149
- Mortlock D.J., Warren S.J., Venemans B.P., et al., 2011, *Nature* 474, 616
- Mushotzky R.F., Done C., Pounds K.A., 1993, *araa* 31, 717
- Mushotzky R.F., Fabian A.C., Iwasawa K., et al., 1995, *Mon. Not. R. Astron. Soc.* 272, L9
- Nandra K., George I.M., Mushotzky R.F., et al., 1997, *ApJ* 477, 602
- Nandra K., O'Neill P.M., George I.M., Reeves J.N., 2007, *Mon. Not. R. Astron. Soc.* 382, 194
- Nardini E., Fabian A.C., Reis R.C., Walton D.J., 2011, *Mon. Not. R. Astron. Soc.* 410, 1251
- Netzer H., 2015, *araa* 53, 365
- Osterbrock D.E., Pogge R.W., 1985, *Astrophys. J.* 297, 166
- Paczynsky B., Wiita P.J., 1980 88, 23

- Page K.L., Pounds K.A., Reeves J.N., O'Brien P.T., 2002, *Mon. Not. R. Astron. Soc.* 330, L1
- Pal M., Dewangan G.C., 2013, *Mon. Not. R. Astron. Soc.* 435, 1287
- Parker M.L., Wilkins D.R., Fabian A.C., et al., 2014, *Mon. Not. R. Astron. Soc.* 443, 1723
- Parratt L.G., 1954, *Phys. Rev.* 95, 359
- Pearson K., 1900, *The London, Edinburgh, and Dublin Philosophical Magazine and Journal of Science* 50, 157
- Peterson B., Wilkes B., 2000, *Active Galaxies: Unified Model*
- Petrucci P.O., Ponti G., Matt G., et al., 2007 470, 889
- Pierre Auger Collaboration Abraham J., Abreu P., et al., 2007, *Science* 318, 938
- Pounds K., Reeves J., O'Brien P., et al., 2001, *Astrophys. J.* 559, 181
- Pounds K.A., Nandra K., Stewart G.C., et al., 1990, *Nature* 344, 132
- Pounds K.A., Reeves J.N., Page K.L., O'Brien P.T., 2004, *Astrophys. J.* 616, 696
- Pounds K.A., Stanger V.J., Turner T.J., et al., 1987, *MNRAS* 224, 443
- Pringle J.E., 1981, *araa* 19, 137
- Rees M.J., 1984, *araa* 22, 471
- Rees M.J., Netzer H., Ferland G.J., 1989, *Astrophys. J.* 347, 640
- Reeves J., Done C., Pounds K., et al., 2008, *Mon. Not. R. Astron. Soc.* 385, L108
- Reeves J.N., Braito V., Gofford J., et al., 2014, *Astrophys. J.* 780, 45
- Reeves J.N., Braito V., Nardini E., et al., 2016, *ApJ* 824, 20
- Reeves J.N., O'Brien P.T., Braito V., et al., 2009, *Astrophys. J.* 701, 493
- Reeves J.N., O'Brien P.T., Ward M.J., 2003, *Astrophys. J., Lett.* 593, L65
- Refsdal S., 1964, *Mon. Not. R. Astron. Soc.* 128, 295
- Reynolds C.S., 2014, *Space Sci. Rev.* 183, 277
- Reynolds C.S., Brenneman L.W., Lohfink A.M., et al., 2012, In: Petre R., Mitsuda K., Angelini L. (eds.) *American Institute of Physics Conference Series*, Vol. 1427. American Institute of Physics Conference Series, p.157
- Reynolds C.S., Nowak M.A., 2003, *PhysRep* 377, 389
- Richards G.T., Lacy M., Storrie-Lombardi L.J., et al., 2006 166, 470
- Risaliti G., Elvis M., Fabbiano G., et al., 2005, *Astrophys. J., Lett.* 623, L93
- Risaliti G., Harrison F.A., Madsen K.K., et al., 2013, *Nat* 494, 449
- Risaliti G., Maiolino R., Salvati M., 1999, *Astrophys. J.* 522, 157
- Rybicki G.B., Lightman A.P., 1986, *Radiative Processes in Astrophysics*
- Sambruna R.M., Reeves J.N., Braito V., et al., 2009, *Astrophys. J.* 700, 1473
- Sambruna R.M., Tombesi F., Reeves J.N., et al., 2011, *Astrophys. J.* 734, 105
- Scargle J.D., Norris J.P., Jackson B., Chiang J., 2013, *ApJ* 764, 167
- Schmoll S., Miller J.M., Volonteri M., et al., 2009, *Astrophys. J.* 703, 2171
- Schwarzschild K., 1916, *Abh. Konigl. Preuss. Akad. Wissenschaften Jahre 1906,92, Berlin,1907* 1916
- Seyfert C.K., 1943, *Astrophys. J.* 97, 28
- Shakura N.I., Sunyaev R.A., 1973 24, 337
- Sijacki D., Springel V., Di Matteo T., Hernquist L., 2007, *Mon. Not. R. Astron. Soc.* 380, 877
- Strüder L., Briel U., Dennerl K., et al., 2001, *AAP* 365, L18
- Su M., Slatyer T.R., Finkbeiner D.P., 2010, *Astrophys. J.* 724, 1044
- Svoboda J., Dovciak M., Goosmann R.W., et al., 2012 545, A106
- Tanaka Y., Nandra K., Fabian A.C., et al., 1995, *Nat* 375, 659
- Thorne K.S., 1974, *Astrophys. J.* 191, 507
- Torresi E., Grandi P., Longinotti A.L., et al., 2010, *Mon. Not. R. Astron. Soc.* 401, L10
- Trump J.R., Impey C.D., McCarthy P.J., et al., 2007 172, 383
- Turner T.J., Pounds K.A., 1989, *Mon. Not. R. Astron. Soc.* 240, 833
- Ulmschneider P., Priest E.R., Rosner R., (eds.) 1991, *Mechanisms of Chromospheric and Coronal Heating*
- Urry C.M., Padovani P., 1995, *Publ. Astron. Soc. Pac.* 107, 803
- Vasudevan R.V., Fabian A.C., Reynolds C.S., et al., 2016, *Mon. Not. R. Astron. Soc.* 458, 2012
- Vaughan S., Fabian A.C., Ballantyne D.R., et al., 2004, *Mon. Not. R. Astron. Soc.* 351, 193
- Walton D.J., Nardini E., Fabian A.C., et al., 2013, *Mon. Not. R. Astron. Soc.* 428, 2901
- Walton D.J., Risaliti G., Harrison F.A., et al., 2014, *Astrophys. J.* 788, 76
- Wilkins D.R., Fabian A.C., 2012, *Mon. Not. R. Astron. Soc.* 424, 1284
- Wilkins D.R., Gallo L.C., Grupe D., et al., 2015, *Mon. Not. R. Astron. Soc.* 454, 4440
- Wilms J., Allen A., McCray R., 2000, *ApJ* 542, 914
- Wilms J., Reynolds C.S., Begelman M.C., et al., 2001, *Mon. Not. R. Astron. Soc.* 328, L27
- Wilson A.S., Colbert E.J.M., 1995, *Astrophys. J.* 438, 62
- Wolter H., 1952, *Annalen der Physik* 445, 94
- Yaqoob T., Padmanabhan U., 2004, *Astrophys. J.* 604, 63

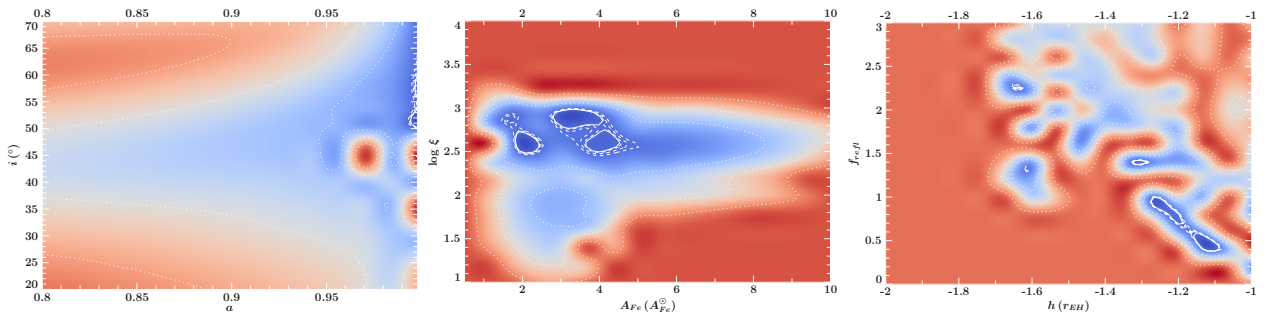
Appendices

Sample Contours

Figure 49: Ark 120
Model I

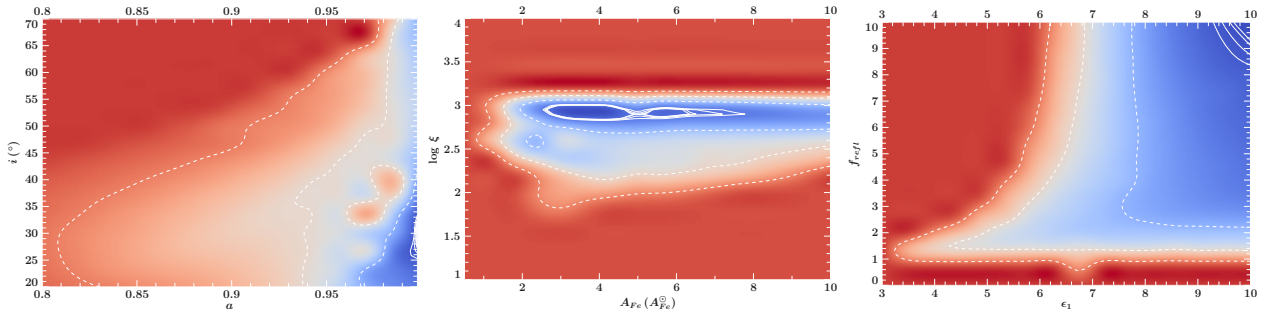


Model II

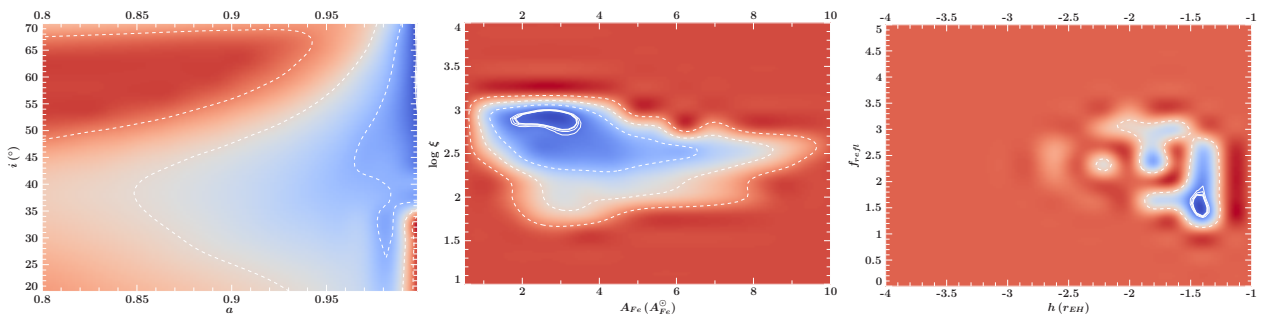


Most parameters are well constrained. While the lamppost height shows some degeneracy with the reflection fraction, it can still be constrained to less than $1.4 r_{EH}$.

Figure 50: Fairall 9
Model I

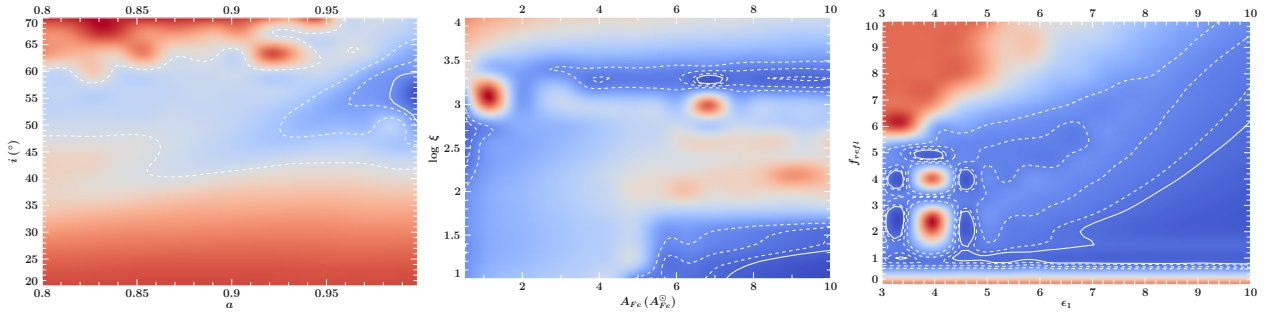


Model II

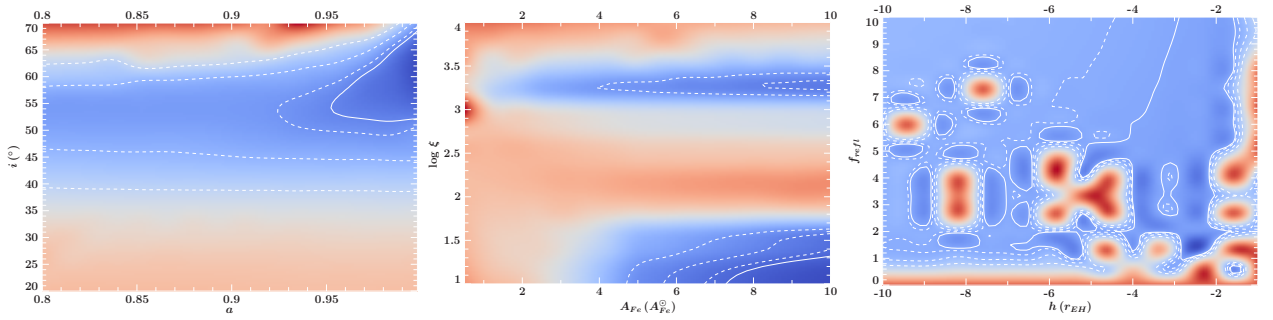


Though giving better χ^2 , the RELXILL-fit gives only lower boundaries for the emissivity profile parameters. Using the lamppost model, we can constrain the iron abundance and radiation source parameters (bottom right) significantly better and to physically more reasonable values.

Figure 51: PDS 456
Model I

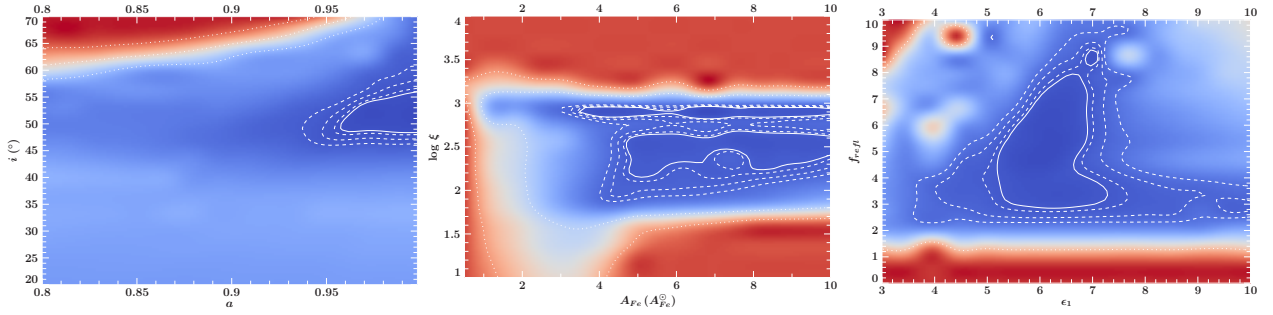


Model II

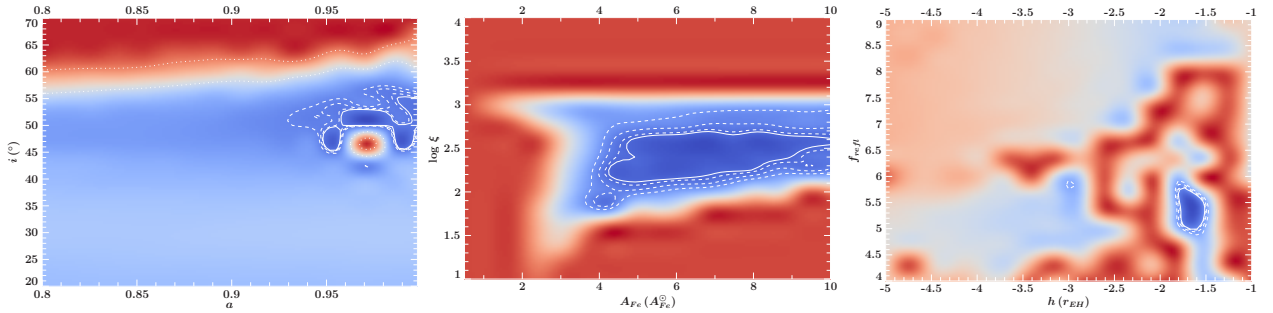


The ionisation parameter (mid panels) finds two statistically significant minima, but we dismiss the minimum at $\log \xi = 1$ as too low to be physically reasonable. Inclination and spin parameter are unambiguously constrained, although at large confidence intervals. Where the landscape of the emissivity profile parameters is complicated and has multiple minima, the lamppost parameters, though poorly constrained have a clear minimum.

Figure 52: NGC 1365
Model I

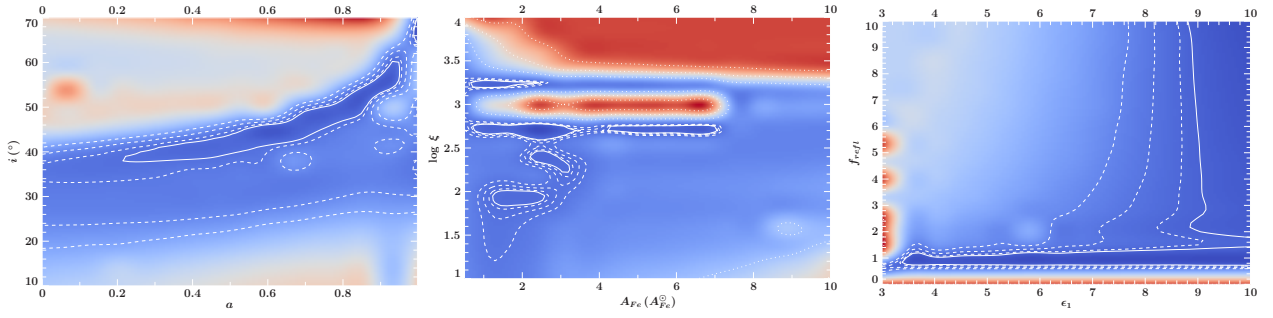


Model II

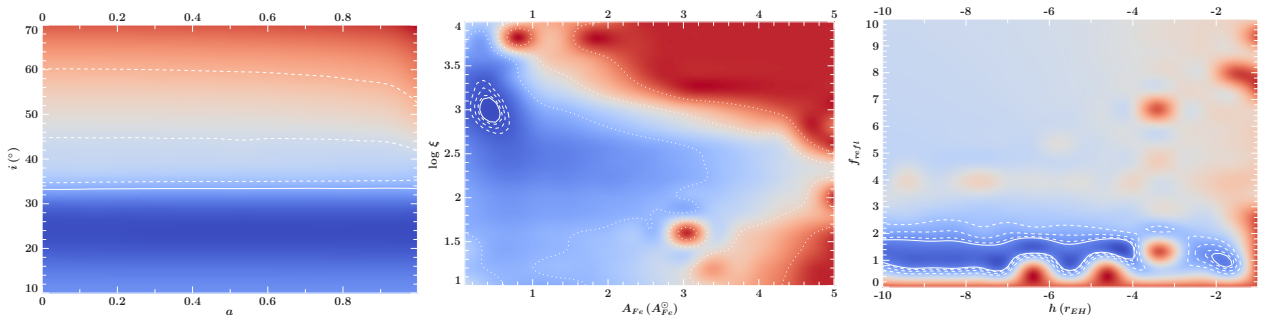


The contours are well constrained, unambiguous and consistent for both models. Constraints on lamppost parameters are closer than for the emissivity profile.

Figure 53: MCG 6-30-15
Model I

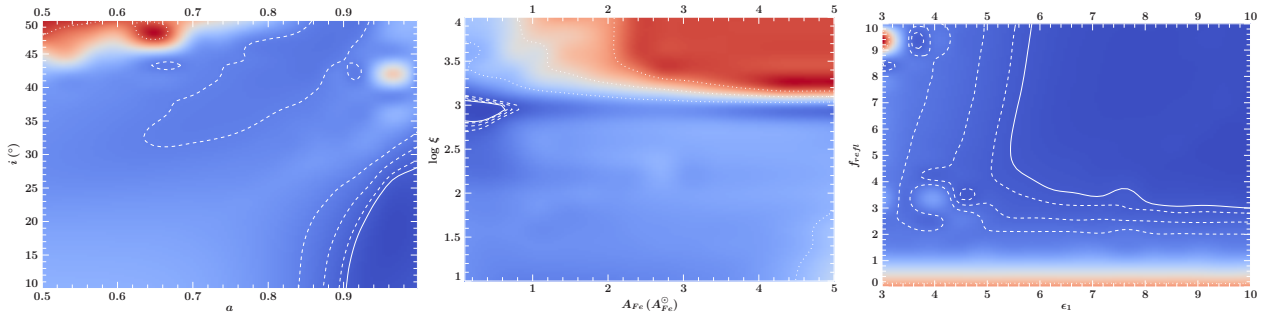


Model II

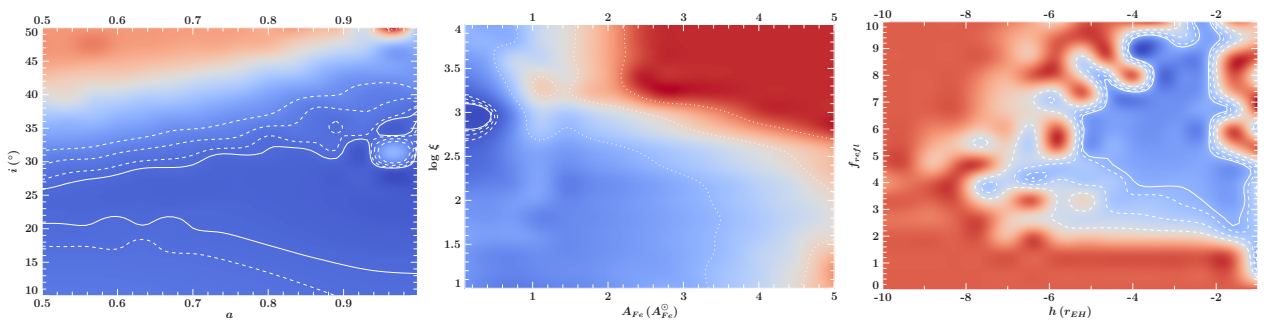


Going from Model II to Model III, degeneracy in $\log \xi$, F_{Fe} and reflection fraction is resolved, but spin gets unconstrainable. The lamppost height finds a very large confidence interval.

Figure 54: Mrk 841
Model I

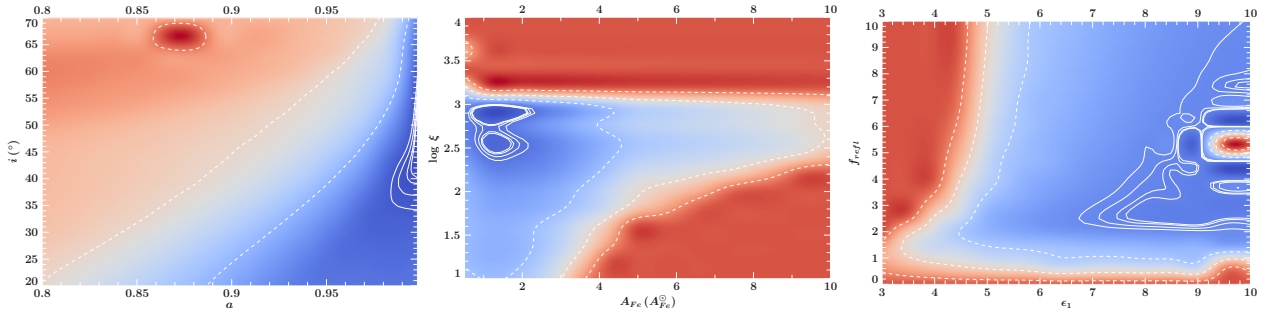


Model II

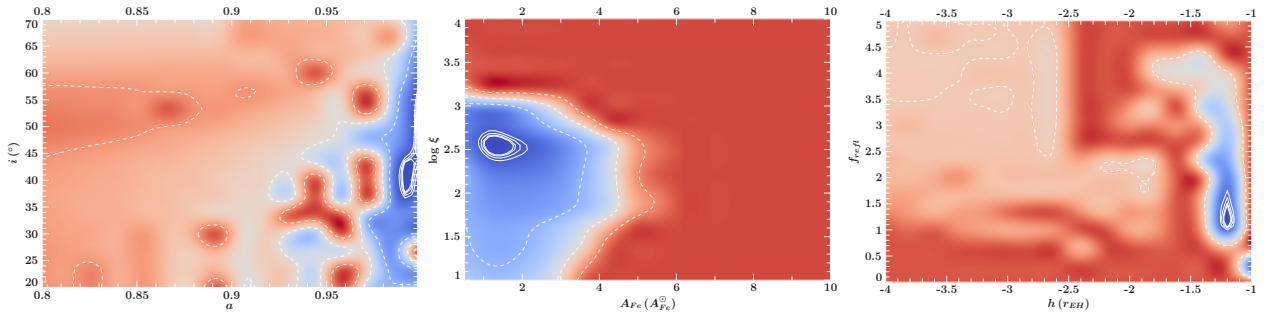


Contours are consistent. Reflection parameters and inclinations are closer constrained in Model III, while spin gets less constrainable.

Figure 55: 3C 382
Model I

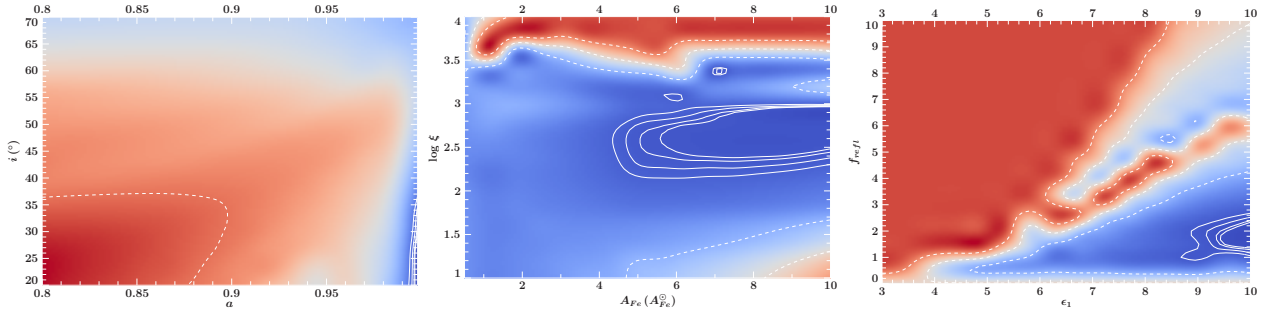


Model II

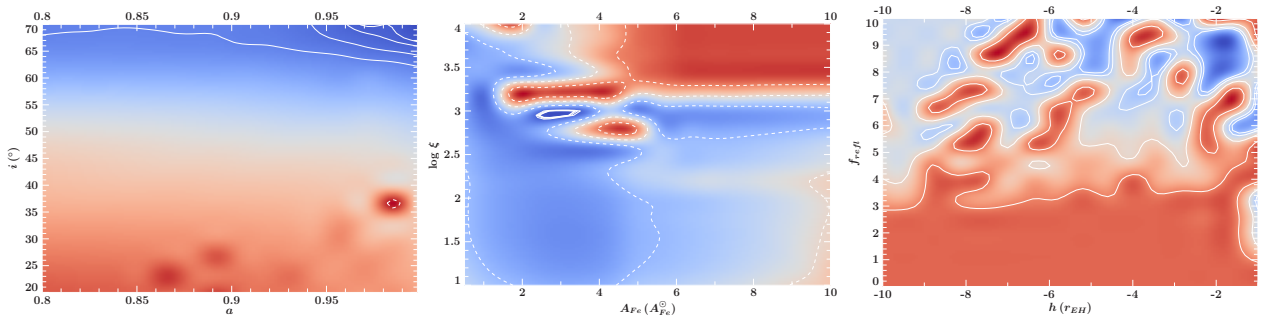


Contours are well constrained and consistent for both models. Again the landscape of the lamppost parameter is closer constrained and less complicated than that of the emissivity profile.

Figure 56: 3C 390.3
Model I

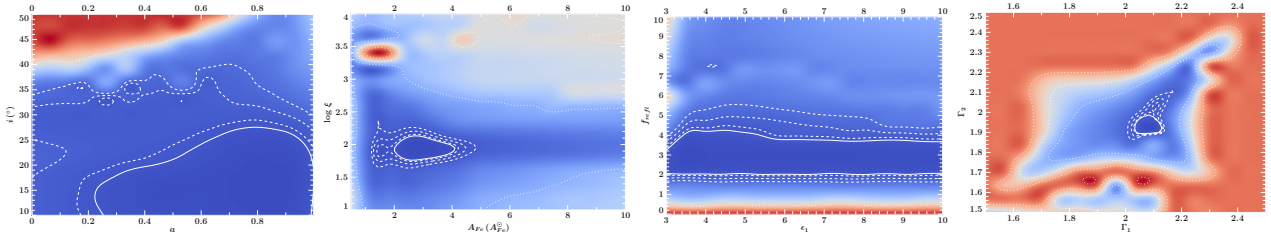


Model II

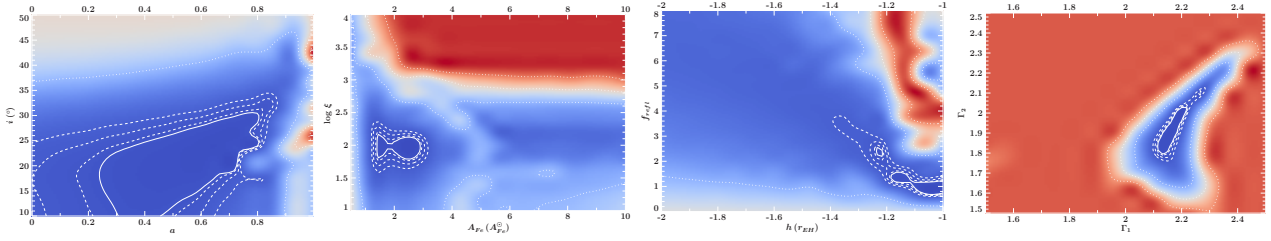


Comparing the models for 3C 390.3 shows that the emissivity profile finds a reasonably constrained and unambiguous fit, but we can not constrain the lamppost source parameters and find a problematically high inclination (bottom left).

Figure 57: Mrk 335
Model I

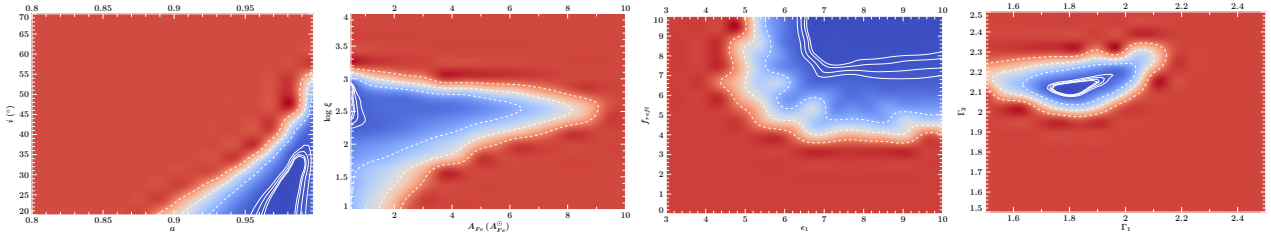


Model II

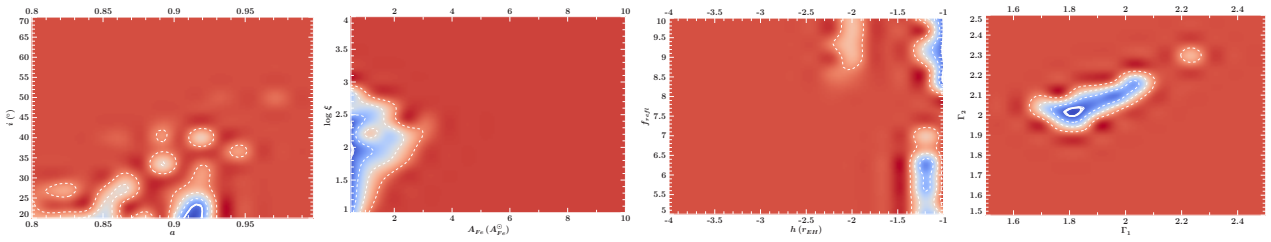


Contours are consistent, but constraining the ionisation parameter is problematic with ambiguity towards very low values. Importantly, the varying Photon indices are unambiguous though the reflection fraction of the lamppost source is nearly unconstrainable (bottom third).

Figure 58: 1H 0419-755
Model I

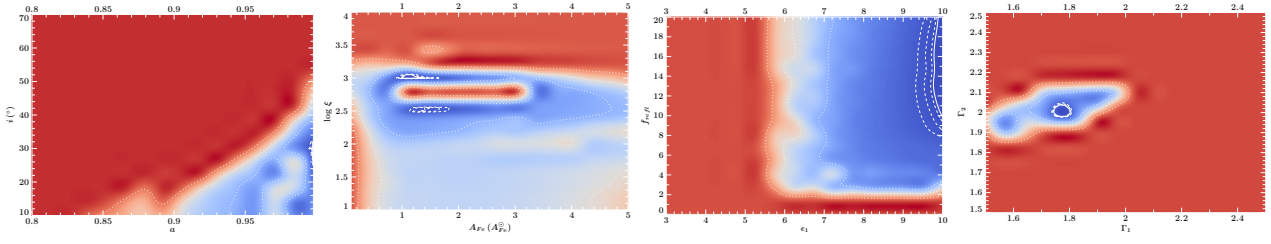


Model II

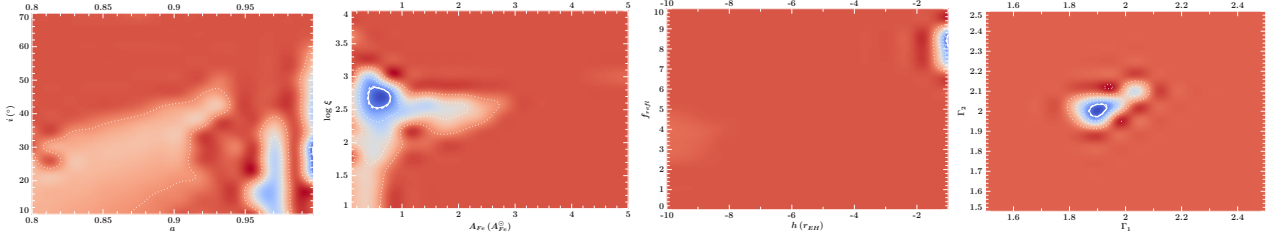


Contours are generally compatible, but with noteworthy less spin in the lamppost geometry. Also, constraining lamppost source height turns out problematic.

Figure 59: Mrk 509
Model I

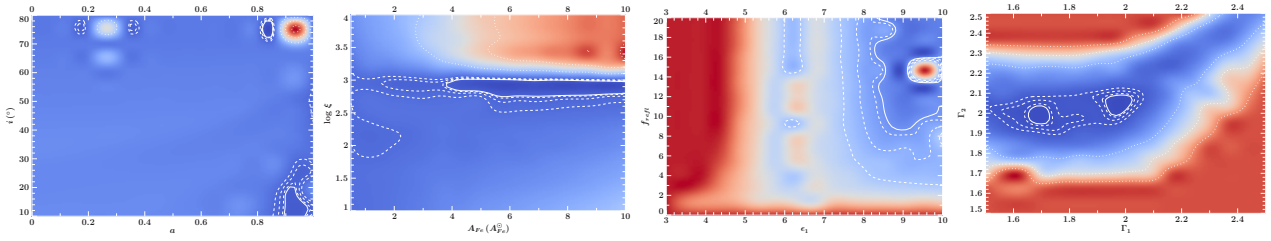


Model II

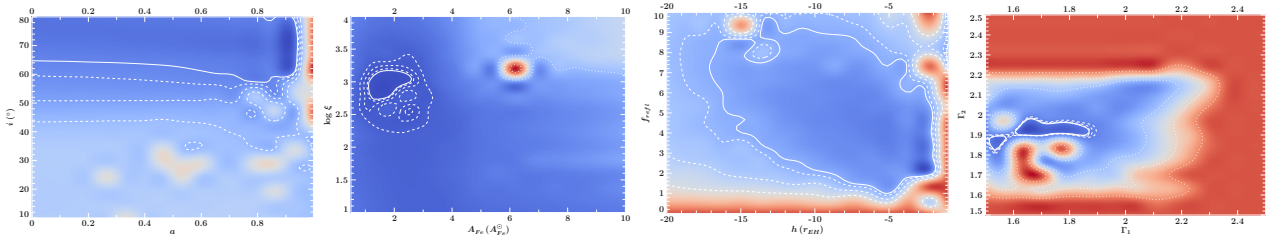


Contours are very consistent. Spin and reflection parameters get slightly better constraints in Model III.

Figure 60: Mrk 1018
Model I



Model II



We see local minima at very high and low inclinations for Model I. In Model II inclination is constrained to high inclinations, but at the expense of a clearly constrained spin.

Acknowledgments and Thanks

At this transitional point in my studies of physics and astronomy, and having finished the largest work project of my life up to now, I naturally want to thank all of the people who accompanied me through this formative and exciting time.

I deeply want to thank Jörn Wilms for supervising this work, for giving insightful and motivating lectures on astronomy, for giving me the possibility to travel to interesting conferences and for useful scientific and personal advice. Equally I have to thank Thomas Dauser and Tobias Beuchert for providing me with a powerful theoretical model, guiding me into this field of research, introducing me to the process of scientific writing and for countless pages of proofreading.

Thank you to summer students S. Jeffreson and J. Tawabutr for helping pre-selecting the sample and getting a grip on the intricacies of the used models and thank you to D. Walton for compiling the sample and providing the data that this study is based on, as well as to J. Garcia for the great work on his reflection models.

Additionally I want to thank Tobias Beuchert, Christina Gräfe, Tobias Hain, Andrea Gokus, Miriam Örtel, Annika Kreikenbohm and Felicia Krauss for being the most helpful travel and conference companions. I also thank Felix Fürst and Andrea for helping out on the cross calibration part of this work.

A collective thank you to everyone at the Remeis Observatory for making this such a great place to work, for the friendly and supportive office climate and the many social activities. Special thanks go to the reliable admins and to the outstanding pool management.

I am very grateful to my parents for always supporting my choices and being there whenever help is needed. And finally I want to thank Franziska Munkert, for being who she is.

Eigenständigkeitserklärung

Hiermit erkläre ich, dass ich diese Arbeit selbstständig angefertigt und keine anderen als die angegebenen Hilfsmittel verwendet habe.

Bamberg, 30. September 2016